

# Design and Evaluation of OFDM Radio Interfaces for High Mobility Communications

Pedro Suárez Casal

Doctoral Thesis UDC / 2015

Advisors: Luis Castedo Ribas  
José Antonio García Naya

Doutorado en Tecnoloxías da Información e Comunicaci3ns en Redes M3viles





D. Luis Castedo Ribas e D. José A. García Naya

CERTIFICAN

Que a memoria titulada “Design and Evaluation of OFDM Radio Interfaces for High Mobility Communications” foi realizada por D. Pedro Suárez Casal baixo a nosa dirección no Departamento de Electrónica e Sistemas da Universidade da Coruña e remata a Tese que presenta para optar ó grao de Doutor.

A Coruña, setembro de 2015.

Asdo.: Dr. Luis Castedo Ribas  
Director da Tese Doutoral  
Catedrático de Universidade  
Departamento de  
Electrónica e Sistemas  
Universidade da Coruña

Asdo.: Dr. José A. García Naya  
Director da Tese Doutoral  
Profesor de Universidade  
Departamento de  
Electrónica e Sistemas  
Universidade da Coruña



**Tese Doutoral:** Design and Evaluation of OFDM Radio Interfaces  
for High Mobility Communications

**Autor:** D. Pedro Suárez Casal

**Directores:** Dr. Luis Castedo Ribas e Dr. José A. García Naya

**Data de defensa:** 18 de novembro de 2015

## **Tribunal**

**Presidente:** Guillem Femenias Nadal

**Vogal:** César Briso Rodríguez

**Secretaria:** Paula María Castro Castro



# Agradecimientos

Al final de una clase, el profesor me preguntó desde la tarima si me gustaría hacer el proyecto de fin de carrera con él. Así empezó mi recorrido en el GTEC hasta ahora, que aspiro a ser doctor. Ese profesor era Luis Castedo, al que agradezco todo el apoyo en lo científico y en lo económico durante estos años, dándome la ocasión de participar en proyectos para mí impensables cuando antes de que empezara todo mis expectativas no iban más allá de sacar una carrera, y luego ya se verá.

Uno de estos proyectos fue implementar una capa física en un sistema en tiempo real, sobre el que se detallan algunos aspectos en esta tesis. Tuve la suerte de compartir este trabajo con Ángel, con el que pasé cuatro años codo con codo, y estoy seguro de que si me lo hubieran cambiado por otro no habríamos llegado tan lejos. Todavía me pregunto cómo fue capaz Luis de confiar en nosotros para semejante tarea, pero le agradezco que nos haya dado esa oportunidad, que aproveché para aprender muchísimo en un trabajo que, aunque con altibajos, siempre me pareció apasionante.

Esta tarea tampoco habría llegado a buen término sin el apoyo constante durante estos años de José Antonio. Desde los inicios, donde era el hombre al que preguntar, sobre todo cuando mi ignorancia me llevaba a pensar en chispas y aparatosos accidentes cuando tenía que tocar un cable, hasta su fantástico trabajo con los demostradores sin los cuales la mayor parte de esta tesis nunca se habría llegado a realizar. En este área también colaboraron Tiago, Néstor, Valentín, Javi, Ismael y Xosé, hasta terminar esa pequeña pieza de ingeniería con la que se hicieron las medidas experimentales. A José Antonio, Ismael y Xosé también tengo que agradecer –más bien se las debo– esas inacabables campañas de medidas nocturnas, de las cuales siempre me quedé corto sacando resultados para compensar su esfuerzo.

También se merecen un recuerdo especial Tiago y José por habernos aguantado durante las comidas, mientras Ángel y yo a veces no hablábamos de otra cosa que no fueran FPGAs, y Paula, que tanto nos ayudó quitándonos trabajo de encima cuando todo se torcía.

Termino estos agradecimientos dedicando este trabajo a mi familia, mis padres y hermanos, y especialmente a María, que siempre me animó a terminar esta tesis, incluso cuando le decía que a lo mejor no valía la pena.



# Resumo

Nas dúas últimas décadas, as modulacións multiportadora emerxeron como una solución de baixa complexidade para combatir os efectos do multitraxecto en comunicacións sen fíos. Entre elas, Orthogonal Frequency Division Multiplexing (OFDM) é posiblemente o esquema de modulación máis estudado, e tamén amplamente adoptado como alicerce de estándares da industria como WiMAX ou LTE. Sen embargo, OFDM é sensible a canles que varían co tempo, unha característica dos escenarios con mobilidade, debido á aparición da interferencia entre portadoras (ICI).

A implementación de equipamento hardware para o usuario final faise normalmente en chips dedicados, aínda que entornos de investigación, prefírense solucións máis flexibles. Unha aproximación popular é a coñecida como Software Defined Radio (SDR), onde os algoritmos de procesado de sinal se implementan en hardware reconfigurable como Digital Signal Processors (DSPs) e Field Programmable Gate Arrays (FPGAs).

O obxectivo deste traballo é dobre. Por un lado, definir unha arquitectura para implementacións de tempo real de capas físicas basadas en OFDM usando como referencia o estándar WiMAX, probada nunha plataforma composta por DSPs e FPGAs. Por outra banda, estudar os efectos da selectividade en tempo no sinal OFDM, definindo métodos de estimación de canle que teñen en conta a ICI, e evaluándoos tanto en simulación como con medidas experimentais. Seguíronse dúas aproximacións para caracterizar o comportamento de formas de onda OFDM baixo condicións de mobilidade, unha baseada nun emulador de canle que traballa en tempo real, e outra en inducir grandes ensanchamentos Doppler no sinal mediante a extensión da duración do símbolo OFDM.



# Resumen

En las dos últimas décadas, las modulaciones multiportadora han emergido como una solución de baja complejidad para combatir los efectos del multitrayecto en comunicaciones inalámbricas. Entre ellas, Orthogonal Frequency Division Multiplexing (OFDM) es posiblemente el esquema de modulación más estudiado, y también ampliamente adoptado como fundamento de estándares de la industria como WiMAX o LTE. Sin embargo, OFDM es sensible a canales que varían con el tiempo, una característica de los escenarios con movilidad, debido a la aparición de la interferencia entre portadoras (ICI).

La implementación de equipamiento hardware para el usuario final se hace normalmente en chips dedicados, aunque en entornos de investigación, son preferibles soluciones más flexibles. Una aproximación popular es la conocida como Software Defined Radio (SDR), donde los algoritmos de procesamiento de señal se implementan en hardware reconfigurable como Digital Signal Processors (DSPs) y Field Programmable Gate Arrays (FPGAs).

El objetivo de este trabajo es doble. Por un lado, definir una arquitectura para implementaciones de tiempo real de capas físicas basadas en OFDM usando como referencia el estándar WiMAX, probada en una plataforma compuesta por DSPs y FPGAs. Por otro lado, estudiar los efectos de la selectividad en tiempo en la señal OFDM, definiendo métodos de estimación de canal que tengan en cuenta la ICI, y evaluándolos tanto en simulación como con medidas experimentales. Se han seguido dos aproximaciones para caracterizar el comportamiento de formas de onda OFDM bajo condiciones de movilidad, una basada en un emulador de canal que trabaja en tiempo real, y otra en inducir grandes ensanchamientos Doppler en la señal mediante la extensión de la duración del símbolo OFDM.



# Abstract

In the last two decades, multicarrier modulations have emerged as a low complexity solution to combat the effects of the multipath in wireless communications. Among them, Orthogonal Frequency Division Multiplexing (OFDM) is possibly the most studied modulation scheme, and has also been widely adopted as the foundation of industry standards such as WiMAX or LTE. However, OFDM is sensitive to time selective channels, which are featured in mobility scenarios, due to the appearance of Inter-Carrier Interference (ICI).

Implementation of hardware equipment for the end user is usually implemented in dedicated chips, but in research environments, more flexible solutions are preferred. One popular approach is the so called Software Defined Radio (SDR), where the signal processing algorithms are implemented in reconfigurable hardware such as Digital Signal Processors (DSPs) and Field Programmable Gate Arrays (FPGAs).

The aim of this work is two-fold. On the one hand, to define an architecture for the implementation of real-time OFDM-based physical layers, using as a reference the WiMAX standard, and it is tested on a platform composed by DSPs and FPGAs. On the other hand, to study the effects of the time selectivity on the OFDM signal, defining channel estimation methods aware of the ICI, and its evaluation both in simulation as well as experimental measurements. Two approaches have been followed to assess the behavior of OFDM waveforms under mobility conditions, one based on a real-time channel emulator, and the other on inducing large Doppler spreads in the signal by extending the duration of the OFDM symbols.



# Contents

<b>1</b>	<b>Introduction</b>	<b>1</b>
1.1	Thesis Overview . . . . .	3
1.2	Authored Publications . . . . .	4
1.2.1	Journal Publications . . . . .	4
1.2.2	Conference Publications . . . . .	4
<b>2</b>	<b>Elements of OFDM-based Transceivers</b>	<b>7</b>
2.1	Signal model . . . . .	7
2.2	Receiver . . . . .	8
2.2.1	Frame detection . . . . .	11
2.2.2	Time and frequency offsets estimation . . . . .	12
2.2.3	Channel estimation . . . . .	12
2.2.4	Signal equalization . . . . .	14
2.2.5	MIMO communications . . . . .	15
2.3	WiMAX Physical Layer . . . . .	15
2.3.1	WiMAX Advanced . . . . .	17
2.4	Conclusions . . . . .	19
<b>3</b>	<b>SDR Architecture for OFDMA</b>	<b>21</b>
3.1	Mobile WiMAX Physical Layer Design . . . . .	22
3.1.1	Digital Up/Downconversion . . . . .	24
3.1.2	Frame control . . . . .	24
3.1.3	Downlink Synchronization . . . . .	24
3.1.4	Subchannelization and Channel Equalization . . . . .	26
3.1.5	Channel Coding . . . . .	27
3.1.6	Physical Layer (PHY) Control . . . . .	28
3.1.7	Advanced WiMAX . . . . .	29
3.2	Conclusions . . . . .	30

<b>4</b>	<b>Evaluation of the Proposed OFDMA SDR Architecture under Doubly-Selective Channels</b>	<b>31</b>
4.1	Channel emulator . . . . .	31
4.2	Results . . . . .	33
4.2.1	Experiments under static scenarios . . . . .	33
4.2.2	Experiments under emulated mobile scenarios . . . . .	34
4.3	Conclusion . . . . .	38
<b>5</b>	<b>Estimation of MIMO-OFDM Doubly-Selective Channels</b>	<b>39</b>
5.1	State of the Art . . . . .	39
5.2	Signal Model . . . . .	41
5.3	ICI Estimation . . . . .	42
5.3.1	Optimal BEM Design . . . . .	44
5.3.2	Optimal BEM Design under Spatially Correlated Channels . . . . .	47
5.3.3	Channel BEM Coefficients Estimation . . . . .	48
5.3.4	Computational Complexity . . . . .	49
5.4	Results . . . . .	50
5.4.1	Estimation under Spatially Uncorrelated Channels . . . . .	51
5.4.2	Estimation under Spatially Correlated Channels . . . . .	54
5.5	Conclusions . . . . .	56
<b>6</b>	<b>Experimental Evaluation under Doubly-Selective Channels</b>	<b>57</b>
6.1	Signal Model . . . . .	58
6.2	Receiver Structure . . . . .	59
6.2.1	Frame Detection and Synchronization . . . . .	60
6.2.2	Inter-Carrier Interference (ICI) Cancellation and Equalization . . . . .	60
6.3	Experimental Setup . . . . .	62
6.3.1	Physical Layer Configuration . . . . .	66
6.4	Results . . . . .	67
6.4.1	ICI Estimation Algorithms Evaluation . . . . .	67
6.4.2	Indoor, Outdoor and MIMO configurations . . . . .	73
6.4.3	Throughput . . . . .	79
6.5	Conclusions . . . . .	86
<b>7</b>	<b>Conclusions and Future Work</b>	<b>89</b>
7.1	Future Work . . . . .	90
7.1.1	ICI estimation on the Hardware Platform . . . . .	91
7.1.2	Channel Characterization . . . . .	91
7.1.3	Uplink Evaluation and beyond OFDM . . . . .	91

<b>A</b>	<b>Resumen de la tesis</b>	<b>101</b>
A.1	Arquitectura SDR para la implementación de sistemas basados en OFDM . . .	102
A.2	Estimación de canal en OFDM en canales doblemente selectivos . . . . .	104
A.3	Evaluación experimental de OFDM bajo canales doblemente selectivos . . . .	105
A.4	Conclusiones . . . . .	107



# List of Figures

2.1	The frequency channel matrix when transmitting OFDM signals over time-varying channels has a banded structure, with its energy focused in the regions marked in yellow color. . . . .	11
2.2	Block diagram of an IEEE Std 802.16e transmitter. . . . .	16
2.3	Examples of pilot patterns in Mobile WiMAX for the PUSC SISO zone (left-hand side), and WiMAX Advanced for SISO (right-hand side). Pilot subcarriers are marked as blue, while the remaining are allocated to data. . . . .	18
3.1	Global architecture of the base (top) and mobile (bottom) stations including the downlink building blocks. TI C6416 is a DSP model of Texas Instruments [8]; and Virtex II V2000, Virtex 4 SX55, and Virtex 4 SX35 are FPGA models from Xilinx [11, 12]. . . . .	23
3.2	Downlink frame detection and synchronization subsystem implemented in the Mobile Station (MS). . . . .	25
3.3	Operation of the convolutional coding and decoding with tail-biting. . . . .	27
3.4	Mapping of data bursts to the downlink subframe with the Ohseki algorithm. . . . .	29
3.5	Proposed 802.16m architecture. . . . .	30
4.1	Block diagram of the OFDMA-TDD evaluation system configured to test the downlink. . . . .	32
4.2	Setup of the hardware platform during the radio-frequency measurements. . . . .	34
4.3	Constellation of the RF test with the profile of 8.75 MHz. . . . .	35
4.4	Constellation of the RF test with the profile of 10 MHz. . . . .	35
4.5	Downlink frame detection error rate in AWGN and ITU-R channels. . . . .	36
4.6	Coded BER over Additive White Gaussian Noise (AWGN) channel using the 3.5 MHz downlink profile. . . . .	37
4.7	Coded BER over ITU-R channels using the 8.75 MHz downlink profile. . . . .	37
4.8	FER over ITU-R channel using the 8.75 MHz downlink profile. Bursts of 6480 bits for QPSK 1/2 and 12960 bits for 16-QAM 1/2. . . . .	38

5.1	General scheme of the ICI estimation strategy. From the received OFDM symbols an initial frequency response estimations are obtained, which are eventually used to obtain the ICI per subcarrier from the variations in the time direction. . . . .	43
5.2	Overview of the ICI estimation scheme for $K = 4$ consecutive OFDM symbols. $\hat{\mathbf{g}}_k$ is the frequency response estimation for the $k$ -th OFDM symbol. The estimates per subcarrier in the time direction $\hat{\mathbf{g}}_n$ are used to recover the evolution of the channel frequency response over time $\mathbf{g}_n$ for the $n$ -th subcarrier.	45
5.3	MSE of the channel matrix estimation over normalized Doppler spread for $\text{SNR} = 30$ dB and under spatially uncorrelated channels. . . . .	52
5.4	MSE of the channel matrix estimation over SNR for a normalized Doppler spread value $f_d T = 0.20$ and under spatially uncorrelated channels. . . . .	53
5.5	BER over SNR for $2 \times 2$ and $4 \times 4$ MIMO transmissions for normalized Doppler spread value $f_d T = 0.20$ and under spatially uncorrelated channels. . . . .	53
5.6	MSE over SNR of the channel matrix estimation for the $4 \times 4$ MIMO system, a normalized Doppler spread value $f_d T = 0.18$ , and under spatially correlated channels. . . . .	55
5.7	MSE over normalized Doppler spread of the channel matrix estimation for the $4 \times 4$ MIMO system, a fixed $\text{SNR} = 30$ dB, and under spatially correlated channels. . . . .	55
5.8	MSE over OFDM symbol index of the channel matrix estimation for the $4 \times 4$ MIMO system, a fixed $\text{SNR} = 30$ dB, a normalized Doppler spread value $f_d T = 0.18$ , and under spatially correlated channels. . . . .	56
6.1	Block diagram of the outdoor-to-outdoor measurement setup. The transmit antennas are placed outdoors and the receive antennas are installed outside the car on its roof. The interpolator at the transmitter side and the decimator at the receiver side enable the recreation of high speed conditions during low speed experiments. The corresponding outdoor-to-indoor setup is basically the same. The only difference is that receiving antennas are placed inside the car instead of outside. . . . .	59
6.2	Block diagram of the receiver structure with decimation and the OFDM receiver with ICI cancellation. The OFDM receiver is the same for the experimental and the simulation results. . . . .	60

6.3	Base station downlink transmitter is placed outdoors, on the second floor of the CITIC building located in the Campus de Elviña at the University of A Coruña. Note that only one of the two vertically polarized antennas is used for $1 \times 1$ transmissions, while both cross polarized antennas are used for the $2 \times 2$ MIMO transmissions. . . . .	64
6.4	Mobile receivers mounted on a car. Two antennas corresponding to the outdoor receiver are placed on the roof of the car, while another two antennas for the second receiver are inside the car, between the two front seats. . . . .	65
6.5	First measurement scenario at the Campus de Elviña, A Coruña. The measurement trajectory as well as the location of the base station are shown. . .	65
6.6	Second measurement scenario at the Campus de Elviña, A Coruña. The measurement trajectory as well as the location of the base station are shown. . .	66
6.7	Perfect channel estimator and DPS-BEM with orders $Q = \{3, 4, 5\}$ and with interpolation factor $I = 32$ . . . . .	69
6.8	Comparison of pilot-based channel estimator and DPS-BEM with orders $Q = \{3, 4, 5\}$ and with interpolation factor $I = 32$ . . . . .	69
6.9	Comparison of perfect channel estimator and a pilot-based channel estimator (LS) with and without feedback, both with interpolation factor $I = 32$ . . . . .	70
6.10	Comparison of perfect channel estimator and a pilot-based channel estimator (LS) with and without feedback, both with interpolation factor $I = 20$ . . . . .	71
6.11	Comparison of perfect channel estimator and a pilot-based channel estimator (LS) with and without feedback, both with interpolation factor $I = 12$ . . . . .	71
6.12	Comparison of pilot-based channel estimator (LS) with DPS-BEM and KL-BEM and interpolation factor $I = 32$ . . . . .	72
6.13	Comparison of perfect estimator and a pilot-based estimator with linear interpolation, both with interpolation factor $I = 32$ . . . . .	73
6.14	EVM and SNR for $1 \times 1$ and $v^I = 120$ km/h. The receive antennas are placed outside the car. . . . .	74
6.15	EVM and SNR for $1 \times 1$ and $v^I = 360$ km/h. The receive antennas are placed outside the car. . . . .	75
6.16	EVM and SNR for $1 \times 1$ and $v^I = 600$ km/h. The receive antennas are placed outside the car. . . . .	75
6.17	EVM and SNR for $1 \times 1$ and $v^I = 120$ km/h. The receive antennas are placed inside the car. . . . .	76
6.18	EVM and SNR for $1 \times 1$ and $v^I = 360$ km/h. The receive antennas are placed inside the car. . . . .	76
6.19	EVM and SNR for $1 \times 1$ and $v^I = 600$ km/h. The receive antennas are placed inside the car. . . . .	77

6.20 EVM and SNR for $2 \times 2$ and $v^I = 120$ km/h. The receive antennas are placed outside the car. . . . .	78
6.21 EVM and SNR for $2 \times 2$ and $v^I = 360$ km/h. The receive antennas are placed outside the car. . . . .	78
6.22 EVM and SNR for $2 \times 2$ and $v^I = 600$ km/h. The receive antennas are placed outside the car. . . . .	79
6.23 Throughput for $1 \times 1$ and $v^I = 120$ km/h. The receive antennas are placed outside the car. . . . .	80
6.24 Throughput for $1 \times 1$ and $v^I = 360$ km/h. The receive antennas are placed outside the car. . . . .	81
6.25 Throughput for $1 \times 1$ and $v^I = 600$ km/h. The receive antennas are placed outside the car. . . . .	81
6.26 Throughput for $1 \times 1$ and $v^I = 120$ km/h. The receive antennas are placed inside the car. . . . .	82
6.27 Throughput for $1 \times 1$ and $v^I = 360$ km/h. The receive antennas are placed inside the car. . . . .	83
6.28 Throughput for $1 \times 1$ and $v^I = 600$ km/h. The receive antennas are placed inside the car. . . . .	83
6.29 Throughput for $2 \times 2$ and $v^I = 120$ km/h. The receive antennas are placed outside the car. . . . .	84
6.30 Throughput for $2 \times 2$ and $v^I = 360$ km/h. The receive antennas are placed outside the car. . . . .	84
6.31 Throughput for $2 \times 2$ and $v^I = 600$ km/h. The receive antennas are placed outside the car. . . . .	85

---

# Chapter 1

## Introduction

In August 1914, several submarine cables, which used to connect Germany with America, were cut by the British forces near Azores as part of the hostilities started with the World War I. For the first time, since businessman Cyrus W. Field had envisioned a transoceanic cable joining both sides of the Atlantic in the middle of 19th century, wired telegraph messages from Germany could not be heard in the United States. This put German army in a delicate situation, since they had to rely on wireless transmissions, which at the time were vulnerable to enemy eavesdroppers. Six years later, technology had matured to allow the first radio broadcasting companies to start operations. This new communication media proved to be very effective, to the extent of being banned by some governments fearing civilian unrest, and creating concerns about the future of newspapers. Wireless communications had already been a hot research topic for two decades, a trend followed by the design of new transmission techniques more robust against interferences and undesired recipients, and by the study of the theoretical limits of the wireless channel capacity. Nowadays, thanks to the digital revolution, technology evolved to allow for high bandwidth data delivery to remote locations, but the nature of the difficulties faced are still the same as those met by engineers a century ago.

The propagation of the electromagnetic waves over the air is affected by phenomena such as pathloss attenuation, diffraction, and reflection on the physical elements between the transmitter and the receiver. A by-product of these effects is the multipath propagation, where a receiver, given a sufficiently high sampling rate, can distinguish distinct replicas of the transmitted signal after traversing different paths, thus leading to a different delay and amplitude for each replica. If the receiver is not prepared to deal with multipath, an interference in the received signal will be observed, and thus a reduced performance will be obtained. Multicarrier communications are among the key technologies which allowed for implementing efficient transceivers capable of combating these effects. Thoroughly studied since the 90's, they have been applied to a wide set of scenarios, ranging from high data rate transmissions over copper telephone links, to underwater acoustic communications. Their most important advantage lies on their

ability to cope with frequency-selective channels with a moderate computational complexity. Between them, Orthogonal Frequency Division Multiplexing (OFDM) has become the most widely adopted scheme given its good properties under slowly time-variant channels, and the possibility of an efficient implementation through the Fast Fourier Transform (FFT) algorithm.

Furthermore, the electromagnetic waves are subject to frequency shifts according to the relative motion between the emitter of these waves and a receiver, an effect postulated by Christian Doppler to explain the color shifts towards red or blue of binary stars as observed from Earth. In mobile wireless channels, the added up Doppler shifted replicas, arriving from multiple directions around the receiver, give raise to the so-called Doppler spread, one of the sources of time selectivity. OFDM suffers under these mobility conditions, where the orthogonality between the subcarriers is lost as long as those channel variations over time become faster. This effect is known as ICI, and its estimation and cancellation has been subject of study in the past years. Additionally, with the popularization of Multiple-Input Multiple-Output (MIMO) systems, where the spatial diversity of the wireless channel is exploited to provide more robust and faster links, these techniques became more important, given that the ICI effect is increased when multiple transmit antennas are used.

Radio equipment has traditionally relied on hardware devices, although with the increasing computational power of digital circuits, it has been possible to develop software implementations of some of its building blocks. The most prominent example is the Software Defined Radio (SDR), a term popularized by Joe Mitola, where general-purpose programmable devices are used to minimize the reliance on dedicated hardware equipment. Most end-user products are still based on very specialized chips, but in research environments more flexible solutions have been adopted to evaluate communication algorithms. Three types of architectures are typically distinguished in this area: demonstrators for showing the feasibility of some technology; prototypes for an eventual development of a product aimed to the end-user; and testbeds, which provide more flexibility than demonstrators and prototypes, and are of special interesting in the research community to perform rapid experimental testing of algorithms and techniques.

Wireless communication testbeds allow for measuring wireless waveforms in real-world scenarios, for experimentally evaluating existing signal processing techniques validated using theoretical models, and for implementing real-time evaluation hardware such as channel emulators. This experimental approach enables researchers to assess if the assumptions made when developing algorithms are suitable for real-world scenarios. The appearance of nonlinearities caused by hardware equipment such as amplifiers, or spurious effects such as frame detection and synchronization errors, might lead to unexpected results, which can be evaluated in a cost-effective manner under this approach.

## **1.1 Thesis Overview**

This work is devoted to design architectures for SDR implementations of OFDM systems, as well as their evaluation in high-mobility scenarios. Additionally, techniques for ICI estimation and cancellation appropriate for existing wireless communication standards are described, and also assessed by means of over-the-air transmissions with the help of a hardware testbed in realistic vehicular scenarios.

Chapter 2 contains an overview of the OFDM waveform and how is affected by typical impairments caused by the hardware equipment and the radio propagation. It will focus on the effects caused by synchronization errors, and on the ICI originated by the time-varying conditions of the channel.

Chapter 3 describes the architecture of a SDR implementation of a OFDM-based transceiver using the WiMAX standard as a reference. This architecture is based both on Digital Signal Processors (DSPs) and on Field Programmable Gate Arrays (FPGAs) and provides a flexible setup for the implementation of other OFDM-based systems.

Chapter 4 is devoted to the performance evaluation of the physical layer described in the previous chapter considering the recreation of time-varying scenarios with the help of a channel emulator implemented on reconfigurable hardware. The performance of the system is assessed for different channel models ranging from the simplest case of AWGN channels to emulated high-speed vehicular channels, thus allowing for evaluating the performance degradation suffered by an OFDM system which does not combat ICI.

Chapter 5 details the ICI estimation techniques used in multicarrier systems, and specifically in OFDM. Many of the algorithms found in the literature deal with systems in which the pilot subcarriers have been specifically designed to improve ICI estimations and to ease its cancellation. However, these pilot structures are not usually found in wireless communications standards. The main purpose of this chapter is to describe some techniques which are adequate for waveforms with arbitrary training symbol allocations, without relying on specific structures optimized for ICI estimation, and also considering MIMO communications with and without spatial correlation between antennas.

Chapter 6 summarizes the results of over-the-air measurement campaigns carried out to evaluate the performance of ICI estimation algorithms in high mobility scenarios. These measurements have been done by inducing large Doppler spreads by means of enlarging the symbol period of the OFDM symbols, obtaining an assessment of the performance of the ICI estimation techniques outside simulation conditions. Experiments, both with Single-Input Single-Output (SISO) and MIMO setups, have been carried out to experimentally evaluate the behavior of ICI estimation algorithms under high mobility conditions and to be able to compare the experimental results to simulation results. The impact on the system throughput is also analyzed.

## 1.2 Authored Publications

### 1.2.1 Journal Publications

- A. Carro-Lagoa, P. Suárez-Casal, J. A. García-Naya, P. Fraga-Lamas, L. Castedo, and A. Morales-Méndez, “Design and implementation of an OFDMA-TDD physical layer for WiMAX applications,” *EURASIP Journal on Wireless Communications and Networking*, vol. 2013, no. 1, p. 243, 2013.
- P. Suárez-Casal, Á. Carro-Lagoa, J. A. García-Naya, P. Fraga-Lamas, L. Castedo, A. Morales-Méndez, ”A Real-Time Implementation of the Mobile WiMAX ARQ and Physical Layer”, *Journal of Signal Processing Systems*, Vol. 78 Issue 3, March 2015.
- P. Suárez-Casal, J. Rodríguez-Piñeiro, J. A. García-Naya, and L. Castedo, “Experimental evaluation of the WiMAX downlink physical layer in high-mobility scenarios,” *EURASIP Journal on Wireless Communications and Networking*, vol. 2015, no. 1, p. 109, 2015.

### 1.2.2 Conference Publications

- P. Suárez-Casal, A. Carro-Lagoa, J. A. García-Naya, and L. Castedo, “A Multicore SDR Architecture for Reconfigurable WiMAX Downlink,” in *13th Euromicro Conference on Digital System Design: Architectures, Methods and Tools (DSD)*, 2010, Lille, France, Sept. 2010, pp. 801–804.
- P. Suárez-Casal, J. A. García-Naya, L. Castedo, and M. Rupp, “KLT-based estimation of rapidly time-varying channels in MIMO-OFDM systems,” in *IEEE 14th Workshop on Signal Processing Advances in Wireless Communications (SPAWC)*, 2013, Darmstadt, Germany, Jun 2013, pp. 654–658.
- Á. Carro-Lagoa, P. Suárez-Casal, P. Fraga-Lamas, J. A. García-Naya, L. Castedo, A. Morales-Méndez, ”Real-time validation of a SDR implementation of TDD WiMAX standard”, *2013 Wireless Innovation Forum European Conference on Communications Technologies and Software Defined Radio (SDR-WinnComm-Europe 2013)*, Munich, Germany, June 2013.
- P. Suárez-Casal, J. A. García-Naya, L. Castedo, and M. Rupp, “Channel Estimation in Spatially Correlated High Mobility MIMO-OFDM Systems,” in *Proceedings of the Tenth International Symposium on Wireless Communication Systems (ISWCS 2013)*, Ilmenau, Germany, Aug 2013.
- P. Suárez-Casal, J. Rodríguez-Piñeiro, J. A. García-Naya, and L. Castedo, “Experimental assessment of WiMAX transmissions under highly time-varying channels,” in the

*Proceedings of the Eleventh International Symposium on Wireless Communication Systems (ISWCS 2014)*, Barcelona, Spain, Aug. 2014.

- J. Rodríguez-Piñeiro, P. Suárez-Casal, J. A. García-Naya, L. Castedo, C. Briso-Rodríguez, and J. I. Alonso-Montes, “Experimental validation of ICI-aware OFDM receivers under time-varying conditions,” in *IEEE 8th Sensor Array and Multichannel Signal Processing Workshop (SAM 2014)*, A Coruña, Spain, June 2014.
- J. Rodríguez-Piñeiro, M. Lerch, P. Suárez-Casal, J. A. García-Naya, S. Caban, M. Rupp, L. Castedo, “LTE Downlink Performance in High Speed Trains”. *IEEE 81st Vehicular Technology Conference (VTC2015-Spring)*, Glasgow, United Kingdom, May 2015.



---

# Chapter 2

## Elements of OFDM-based Transceivers

Modern wireless communications are based on the transmission and processing of electromagnetic waves, which are subject to the phenomena linked with their physical propagation. Among those effects, communication systems have to deal with multipath, propagation losses, fading, and in general, with changes over time on the propagation conditions of the environment.

During the last decade, multicarrier systems have been gradually adopted to combat the aforementioned effects, becoming an efficient solution to most of the challenges posed by wireless channels. In particular, Orthogonal Frequency Division Multiplexing (OFDM) has already been established as a foundation of numerous communication standards, including wireless local and personal area networks and mobile cellular communications.

This chapter is structured as follows. In Section 2.1 the general form of an OFDM signal is defined, and in Section 2.2 the common elements of an OFDM receiver are described. Finally, Section 2.3 provides an overview of a communication standard based on OFDM.

### 2.1 Signal model

OFDM is an example of a frequency multiplexing technique in which source symbols are transmitted in narrow parallel frequency channels called subcarriers. In general, the time domain signal generated by a OFDM system with  $N$  subcarriers can be expressed as [64, 78]

$$s_k[t] = \begin{cases} \sum_{n=0}^{N-1} x_k[n] e^{j2\pi n(t-G)/N} & t = 0, \dots, N + G - 1 \\ 0 & \text{otherwise,} \end{cases} \quad (2.1)$$

where  $x_k[n]$  contains the transmitted signal in the  $n$ -th subcarrier and in the  $k$ -th OFDM symbol, and  $G$  denotes the number of samples assigned as guard interval, inserted to avoid the Intersymbol Interference (ISI) caused by the multipath propagation of the channel. Indices denoted with  $[t]$  represent discrete time, while  $(t)$  correspond to continuous time. A guard

interval defined as in (2.1) is equivalent to append, in the time-domain,  $G$  samples from the end of each symbol to the beginning of each of those symbols, defining the so-called Cyclic Prefix (CP), opposed to the Zero Prefix technique in which silence intervals are inserted. The transmitted symbols in the frequency domain  $x_k[n] = d_k[n] + p_k[n]$  are generated by mapping a sequence of input bits into an alphabet  $A$  of size  $M$ ,  $A = \{a_m\}$ ,  $m \in [1, \dots, M]$ , and with  $d_k[n] \in A$ , multiplexed with other signals such as pilot symbols  $p_k[n]$ , used as references for channel estimation at the receiver, and guard subcarriers. Data symbols  $d_k[n]$  and pilot symbols  $p_k[n]$  can occupy disjoint subcarrier sets if  $d_k[n] = 0$  when  $p_k[n] \neq 0$  and vice versa, or transmitted on the same frequencies, leading to the so-called superimposed training. In this work, it will be assumed that the frequency resources of each OFDM symbol are shared in  $D$  data subcarriers and  $P$  pilot subcarriers, and thus  $N = D + P$ . Finally, the samples  $(N + G)K$  samples of the time-domain  $K$  OFDM symbols  $s_k$  must be serially transmitted

$$s[t] = \sum_{k=0}^{K-1} s_k[t - k(N + G)], \quad t = 0, \dots, (N + G)K - 1. \quad (2.2)$$

The samples of  $s[t]$  are sent to the Digital-to-Analog Converter (DAC) at a sample period  $T_s$ , being the total duration of a single OFDM symbol  $(N + G)T_s$  seconds.

## 2.2 Receiver

OFDM signals, when transmitted over the wireless channel, suffer the effects caused by the propagation of the electromagnetic waves. After passing the arriving signal through the receiving filter, the first task is to determine if an OFDM signal is present. This is usually accomplished by the transmission of some preamble and/or training signals, although some redundancies inherent to OFDM such as the cyclic prefix can also be exploited. After detection, the exact time instant when the frame starts must be estimated, as well as the Doppler shifts caused both by the frequency mismatches between the oscillators of the transmitter and receiver, and the possible relative motion between them.

Let us model a multipath wireless channel as a Linear Time Variant (LTV) system. Such system can be represented by an impulse response of the form  $h[t, l]$  in its baseband equivalent representation. The received signal after the matched filter can be represented as

$$\begin{aligned} r[t] &= e^{j2\pi t\epsilon/N} \sum_{l=0}^{L-1} h[t, l] s[t - l + \theta] + w[t] \\ &= e^{j2\pi t\epsilon/N} \sum_{l=0}^{L-1} h[t, l] \sum_{k=0}^{K-1} s_k[t - l + \theta - k(N + G)] + w[t], \end{aligned} \quad (2.3)$$

where  $\theta$  is the timing offset,  $\epsilon$  the frequency offset,  $h[t, l]$  is the baseband equivalent of the channel coefficients at time instant  $t$  and lag  $l$ , and  $w[t]$  represents the Additive White

Gaussian Noise (AWGN). The next stage is to demultiplex the subcarriers block by block to obtain a version of the transmitted symbols  $x_k[n]$  distorted by the added effects caused by the channel, the synchronization offsets, and the noise. Defining  $r_k[t] = r[t + G + kN_T]$ ,  $h_k[t, l] = h[t + G + kN_T, l]$ ,  $w_k[t] = w[t + G + kN_T]$ , and  $\varepsilon_k[t] = e^{j2\pi(t+G+kN_T)\epsilon/N}$  where  $N_T = N + G$ , the received signal in the  $n$ -th block is

$$\begin{aligned}
r_k[t] &= \varepsilon_k[t] \sum_{l=0}^{L-1} h_k[t, l] \sum_{p=0}^{K-1} s_p[t - l + \theta + G + (k - p)N_T] + w_k[t] \\
&= \varepsilon_k[t] \sum_{l=0}^{L-1} h_k[t, l] s_k[t - l + \theta + G] \\
&\quad + \varepsilon_k[t] \sum_{l=0}^{L-1} h_k[t, l] \sum_{p \neq k} s_p[t - l + \theta + G + (k - p)N_T] + w_k[t], \tag{2.4}
\end{aligned}$$

where the first term is the contribution of the  $k$ -th OFDM symbol, and the second term is the ISI of the previous and next symbols. This ISI term approaches to zero if the channel delay  $L$  is shorter than the cyclic prefix  $G$ , and if the timing offset  $\theta$  is in the range  $[-G, \dots, 0]$ . It will be assumed that the OFDM system is designed to meet these requirements, and under this assumption the received  $m$ -th subcarrier of the  $k$ -th OFDM symbol is

$$\begin{aligned}
y_k[m] &= \frac{1}{N} \sum_{t=0}^{N-1} r_k[t] e^{-j2\pi mt/N} \\
&= \frac{1}{N} \sum_{t=0}^{N-1} \left( \varepsilon_k[t] \sum_{l=0}^{L-1} h_k[t, l] s_k[t - l + G + \theta] + w_k[t] \right) e^{-j2\pi mt/N} \\
&= \frac{1}{N} \sum_{t=0}^{N-1} \varepsilon_k[t] \sum_{l=0}^{L-1} h_k[t, l] s_k[t - l + G + \theta] e^{-j2\pi mt/N} + Z_k[m] \\
&= \frac{1}{N} \sum_{t=0}^{N-1} \varepsilon_k[t] \sum_{l=0}^{L-1} h_k[t, l] \sum_{n=0}^{N-1} x_k[n] e^{j2\pi n(t-l+\theta)/N} e^{-j2\pi mt/N} + Z_k[m] \\
&= \frac{1}{N} \sum_{n=0}^{N-1} x_k[n] e^{j2\pi n\theta} \sum_{t=0}^{N-1} \varepsilon_k[t] \sum_{l=0}^{L-1} h_k[t, l] e^{-j2\pi(nl+(m-n)t)/N} + Z_k[m] \\
&= \frac{1}{N} \sum_{n=0}^{N-1} x_k[n] \Theta[n] \sum_{t=0}^{N-1} \varepsilon_k[t] \sum_{l=0}^{L-1} h_k[t, l] e^{-j2\pi(nl+(m-n)t)/N} + Z_k[m] \\
&= \sum_{n=0}^{N-1} x_k[n] \Theta[n] H_k[n, m, \epsilon] + Z_k[m] \\
&= x_k[m] \Theta[m] G_k[m, \epsilon] + \sum_{n \neq m} x_k[n] \Theta[n] H_k[n, m, \epsilon] + Z_k[m], \tag{2.5}
\end{aligned}$$

where in order to obtain the final expressions the following equalities have been defined:

$$Z_k[m] = \frac{1}{N} \sum_{t=0}^{N-1} w_k[t] e^{-j2\pi mt/N} \quad (2.6)$$

$$\Theta[m] = e^{j2\pi m\theta}, \quad (2.7)$$

$$G_k[m, \epsilon] = \frac{1}{N} \sum_{t=0}^{N-1} \epsilon_k[t] \sum_{l=0}^{L-1} h_k[t, l] e^{-j2\pi lm/N}, \quad (2.8)$$

$$H_k[n, m, \epsilon] = \frac{1}{N} \sum_{t=0}^{T-1} \epsilon_k[t] \sum_{l=0}^{L-1} h_k[t, l] e^{-j2\pi(nl+(m-n)t)/N}. \quad (2.9)$$

Recall that  $\Theta[m]$  is a per subcarrier phase shift originated by the timing offset  $\theta$ ,  $G_k[m, \epsilon]$  is the time-averaged frequency response of the  $L$ -path channel during the  $k$ -th OFDM symbol, attenuated due to the energy spread to the other subcarriers when a frequency offset is present,  $H_k[n, m, \epsilon]$  is an interference term which contains the ICI generated by the frequency offset and by the channel variations, and  $Z_k[n]$  a frequency representation of the noise.

From (2.5) it is apparent that the timing offset causes the appearance of a complex phase multiplying each subcarrier, and it can usually be compensated by the channel estimator as long as its value is in the range  $[-G, \dots, 0]$ , as defined before. This turns out to be one of the main advantages of OFDM, since timing synchronization errors are not critical as long as they lie in the range of the CP. However, frequency offsets cause the appearance of Inter-Carrier Interference (ICI) due to the loss of the orthogonality between subcarriers, which turns out in severe degradation of the received signal if this offset is not corrected. This is not the only source of ICI, given that the channel can suffer variations during an OFDM symbol.

Stacking the  $N$  received subcarriers of an OFDM symbol in a vector, the final expression in (2.5) can be written in matrix form as

$$\mathbf{y}_k = \mathbf{F}(\boldsymbol{\epsilon}_k \mathbf{H}_k \mathbf{F}^H \boldsymbol{\Theta} \mathbf{x}_k + \mathbf{w}_k) = \mathbf{G}_k(\epsilon) \boldsymbol{\Theta} \mathbf{x}_k + \mathbf{z}_k, \quad (2.10)$$

where  $\mathbf{F}_N$  represents the Discrete Fourier Transform (DFT) matrix of size  $N$ ;  $[\mathbf{x}_k]_i = x_k[i]$  is a  $N \times 1$  vector with the transmitted subcarriers corresponding to the  $k$ -th OFDM symbol;  $\mathbf{d}_k$  and  $\mathbf{p}_k$  denote the  $D \times 1$  and  $P \times 1$  vectors of data and pilot subcarriers, defined as  $\mathbf{x}_k = \mathbf{D}_k \mathbf{d}_k + \mathbf{P}_k \mathbf{p}_k$ , where  $\mathbf{D}_k$  and  $\mathbf{P}_k$  denote  $N \times D$  and  $N \times P$  permutation matrices to assign each pilot and data symbol to its final subcarrier;  $\boldsymbol{\Theta} = \text{diag}\{[\Theta[0], \dots, \Theta[N-1]]\}$ ;  $\boldsymbol{\epsilon}_k = \text{diag}\{[\epsilon_k[0], \dots, \epsilon_k[N-1]]\}$ ;  $[\mathbf{H}_k]_{i,j} = h_k[i, \text{mod}((i-j), N_T)]$  is a  $N \times N$  matrix for the convolution of the transmitted signal with the channel impulse response;  $[\mathbf{G}_k(\epsilon)]_{i,j} = H_k[j, i, \epsilon]$  is a  $N \times N$  matrix with the channel frequency response; and  $\mathbf{z}_k = \mathbf{F} \mathbf{w}_k$  is a frequency representation of the noise, with  $[\mathbf{w}_k]_i = w_k[i]$  a  $N \times 1$  vector with the noise samples during the  $k$ -th OFDM symbol and  $\mathbf{z}_k \sim \mathcal{N}(\mathbf{0}, \sigma_w^2 \mathbf{I}_N)$ .

When the channel is time-invariant and with frequency offset  $\epsilon = 0$ , the matrix  $\mathbf{G}_k(\epsilon)$  is diagonal, and a single-tap equalizer could be used, even when the channel is frequency

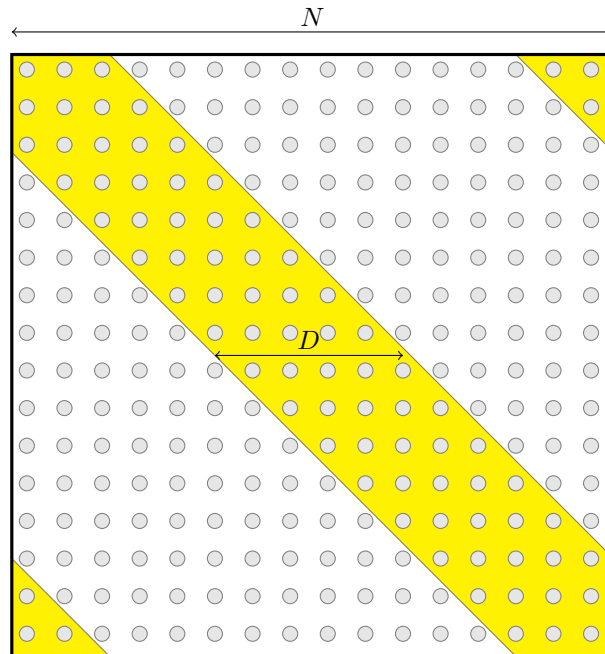


Figure 2.1: The frequency channel matrix when transmitting OFDM signals over time-varying channels has a banded structure, with its energy focused in the regions marked in yellow color.

selective. However,  $\mathbf{G}_k(\epsilon)$  under time-varying channels has a banded structure as shown in Figure 2.1, where the energy of the channel coefficients is spread over the region plotted in yellow color, causing the appearance of ICI from  $D$  neighbor subcarriers. This matrix can be further decomposed as

$$\mathbf{G}_k(\epsilon) = \overline{\mathbf{G}}_k(\epsilon) + \tilde{\mathbf{G}}_k(\epsilon), \quad (2.11)$$

with  $\overline{\mathbf{G}}_k(\epsilon)$  a diagonal matrix with  $[\overline{\mathbf{G}}_k(\epsilon)]_{i,i} = G_k[i, \epsilon]$ , and  $\tilde{\mathbf{G}}_k(\epsilon) = \mathbf{G}_k(\epsilon) - \overline{\mathbf{G}}_k(\epsilon)$ , a matrix containing the coefficients that produce the ICI. As a consequence, channel estimation and equalization turns out to be more challenging tasks. The next subsections deal with the processing blocks being necessary in a OFDM receiver, and how this channel feature affects its performance.

### 2.2.1 Frame detection

One of the first preamble-based algorithms specific for frame detection in OFDM is the one proposed by Schmidl and Cox [76]. In this work, a training sequence built on two consecutive OFDM symbols allows for completing the frame detection, as well as to estimate the timing and frequency offsets. These two symbols exhibit some repetition properties in the time domain which can be exploited by computing the autocorrelation of the input signal to detect the arrival of a preamble. The first symbol is built by generating pseudorandom real-valued sequences, and

by inserting them in the frequency domain every two subcarriers, leaving null subcarriers in-between. After the DFT, a symbol with two equal parts of  $N/2$  samples each will be generated. The autocorrelation metric from the receiving signal is

$$R[t] = \frac{\sum_{d=0}^{N/2-1} r[t+d]r^*[t+d+N/2]}{\sum_{d=0}^{N/2-1} r[t+d]}, \quad (2.12)$$

where  $N$  is the number of subcarriers of the preamble. This algorithm has the advantage of making possible an efficient recursive computation for each arriving sample. A similar approach can be used with the correlation of the CP with the ending of each symbol, providing a mechanism to detect the presence of an OFDM signal even when no preamble is transmitted [64].

### 2.2.2 Time and frequency offsets estimation

Building on the frame detection scheme described previously, the algorithm from Schmidl and Cox uses the autocorrelation metric to also estimate the timing offset by looking for the maximum of its module, and the fractional frequency offset with its phase, i.e.,

$$\hat{\theta} = \underset{t}{\operatorname{argmax}} |R[t]|^2, \text{ and} \quad (2.13)$$

$$\hat{\epsilon} = \frac{\operatorname{angle}(R[\hat{\theta}])}{\pi N}. \quad (2.14)$$

The second symbol is used to estimate the integer frequency offset after the DFT by cross-correlating the two reference blocks.

Although the accuracy of this scheme is good, it allocates many resources for frame detection. Other works have tried to reduce this overhead by using just one OFDM symbol, achieving a similar performance than that of the Schmidl and Cox algorithm [64]. Going back to the last expression in (2.5), it can be seen that ICI not only appears because of frequency mismatches in the oscillators of the stations, but also because of time variations in the impulse response of the channel. Other works have defined algorithms to jointly estimate the frequency offset and the channel variations to obtain all the parameters leading to ICI [67].

### 2.2.3 Channel estimation

Assuming that timing and frequency offsets are corrected, the next stage is channel estimation. It is usual to insert in the frequency domain reference symbols at the transmitter which are known to the receiver. Such strategy is often referred to as Pilot Assisted Training. Other approaches that do not consume resources in terms of pilot symbols are the so-called blind estimation techniques, but this work will focus on the non-blind case since the available communication standards usually allocate subcarriers as pilots. An intermediate solution

consists in superimposed training, where the pilot symbols are added up to the data subcarriers, being necessary to separate pilots and data at the receiver.

The channel estimator can work on different models of the interference. Going back to (2.11) and assuming the frequency offset has been corrected, a receiver can consider the interference  $\tilde{\mathbf{G}}_k$  is negligible, and thus the estimation is limited to the coefficients of the main diagonal of  $\overline{\mathbf{G}}_k$ . This effectively lowers the computational cost. As an example, starting from the model described in (2.5) and assuming ICI and synchronization errors are negligible, a Least Squares (LS) estimation of the channel can be readily obtained as

$$\hat{G}_k[n] = y_k[n]/p_k[n], \quad (2.15)$$

assuming the  $n$ -th subcarrier of the  $k$ -th OFDM symbol  $p_k[n]$  is a pilot symbol known at the receiver. The channel coefficients in the remaining subcarriers, i.e., where user data symbols have been transmitted and they are unknown to the receiver, must be obtained by means of some form of interpolation. For example, LS with the DFT matrix, and Minimum Mean Squared Error (MMSE) interpolations have been proposed, the latter providing better results if the second order statistics of the channel are known at the receiver [30, 91]. The real-time architectures described in Chapter 3 and the corresponding evaluations on Chapter 4 focus on this scenario which assumes ICI is negligible, although tests under mobility will be carried out to assess the consequences of this mismatch on the model assumptions.

A different situation arises if the ICI in  $\mathbf{G}_k$  is significant. In that case, the previous estimator will provide poor results, and more sophisticated techniques can be considered. It can be seen in (2.10) that the number of unknowns in  $\mathbf{G}_k$  is  $N^2$ , and given that  $N$  samples are received per OFDM symbol, this would lead to an under-determined system if training is not properly designed. This strategy would dedicate a large share of the radio resources to estimate all those coefficients, so an alternative is to exploit the banded structure of the channel matrix employing a Basis Expansion Model (BEM). Under this setup it is assumed that the channel variations can be accurately described by a linear model of the form

$$h_k[t, l] = \sum_{q=0}^{Q-1} b_q[t] h_{k,q}[l], \quad (2.16)$$

with  $b_q$  the basis vectors used to linearize the channel, and  $h_{k,q}$  the BEM coefficients to be estimated. This effectively lowers the number of unknowns to  $Q \times L$ , with  $Q \ll N$ . Chapter 5 will be devoted to describe these estimation techniques and how to optimally design these BEMs to reduce the number of coefficients to be estimated. Note that in the frequency domain is  $Q \times N$  the number of coefficients to be estimated.

### 2.2.4 Signal equalization

Once channel estimation is done, estimations of the transmitted symbols can be obtained by means of channel equalization. Equalizers can be classified into two categories: coherent equalizers which consider that the instantaneous channel coefficients are known at the receiver, and non-coherent ones which assume only second-order statistics of the channel are available.

The coherent equalization of an OFDM signal according to the Maximum Likelihood (ML) criteria, which coincides with the Maximum A Posteriori (MAP) criteria under the assumption that the symbols of the transmitted alphabet follow an uniform distribution [71], can be formulated as

$$\hat{\mathbf{x}}_k = \underset{\mathbf{x}_k}{\operatorname{argmax}} \frac{1}{\pi^N \det(\mathbf{C}_w)} \exp(-(\mathbf{y}_k - \mathbf{G}_k \mathbf{x}_k)^H \mathbf{C}_w^{-1} (\mathbf{y}_k - \mathbf{G}_k \mathbf{x}_k)), \quad (2.17)$$

where  $\mathbf{C}_w = \sigma_w^2 \mathbf{I}$  is the covariance matrix of the noise. If  $\mathbf{G}_k$  is not diagonal, the magnitude of the search space of this problem is  $2^N$ , which turns out to be impractical for a moderate number of subcarriers.

Alternatively, classical linear estimators such as LS and Linear Minimum Mean Squared Error (LMMSE) can be applied, and have lower computational complexity than the general MAP approach. For example, the LS equalizer is

$$\hat{\mathbf{x}}_k^{\text{LS}} = \mathbf{G}_k^{-1} \mathbf{y}_k. \quad (2.18)$$

In practical systems, where the actual channel matrix is unknown,  $\mathbf{G}_k$  is replaced by an estimation  $\hat{\mathbf{G}}_k$ . Also, taking into account the banded shape of an channel matrix affected by ICI, the computational complexity of this inversion can be further lowered. In [48, 55] approximations consisting in computing the inversion of submatrices of  $\mathbf{G}_k$  along the main diagonal are proposed. Additionally, recursive computation of the LMMSE equalizer has been developed in [21]. However, all linear equalizers are suboptimal given that in digital communications the transmitted symbols usually do not follow a Gaussian distribution. Due to this property, a linear equalizer must be followed by a decision stage where the information bits are obtained from the equalized symbols with some distance criteria relative to the original alphabet.

Efficient algorithms which consider the ‘‘a-priori’’ information of the discrete alphabet used for the transmitted symbols are the iterative receivers, such as Decision-Feedback Equalization (DFE) [18], and turbo-equalizers. These strategies are very general and can be applied to a broad set of communication problems [26], but there are more specific studies applying these techniques to OFDM under doubly selective channels [75, 77].

### 2.2.5 MIMO communications

The previous signal model can be easily extended to consider Multiple-Input Multiple-Output (MIMO) communications. For the case of a MIMO system with  $M_T$  transmit antennas and  $M_R$  receive antennas, the vector of transmitted subcarriers is  $\mathbf{x}_k = [\mathbf{x}_{k,1}^T, \dots, \mathbf{x}_{k,M_T}^T]^T$  and the noise vector is  $\mathbf{w}_k = [\mathbf{w}_{k,1}^T, \dots, \mathbf{w}_{k,M_R}^T]^T$ . Hence, the received signal model in (2.10) changes to

$$\mathbf{y}_k = (\mathbf{I}_{M_R} \otimes \mathbf{F}) ((\mathbf{I}_{M_R} \otimes \boldsymbol{\varepsilon}_k) \mathbf{H}_k (\mathbf{I}_{M_T} \otimes \mathbf{F}^H \boldsymbol{\Theta}) \mathbf{x}_k + \mathbf{w}_k) = \mathbf{G}_k(\boldsymbol{\varepsilon}) (\mathbf{I}_{M_R} \otimes \boldsymbol{\Theta}) \mathbf{x}_k + \mathbf{z}_k, \quad (2.19)$$

with  $\otimes$  representing the Kronecker product and

$$\mathbf{G}_k(\boldsymbol{\varepsilon}) = \begin{pmatrix} \mathbf{G}_{k,1,1}(\boldsymbol{\varepsilon}) & \mathbf{G}_{k,1,2}(\boldsymbol{\varepsilon}) & \dots & \mathbf{G}_{k,1,M_T}(\boldsymbol{\varepsilon}) \\ \mathbf{G}_{k,2,1}(\boldsymbol{\varepsilon}) & \mathbf{G}_{k,2,2}(\boldsymbol{\varepsilon}) & \dots & \mathbf{G}_{k,2,M_T}(\boldsymbol{\varepsilon}) \\ \dots & \dots & \dots & \dots \\ \mathbf{G}_{k,M_R,1}(\boldsymbol{\varepsilon}) & \mathbf{G}_{k,M_R,2}(\boldsymbol{\varepsilon}) & \dots & \mathbf{G}_{k,M_R,M_T}(\boldsymbol{\varepsilon}) \end{pmatrix}, \quad (2.20)$$

where the channel matrix  $\mathbf{G}_k(\boldsymbol{\varepsilon})$  corresponding to the  $k$ -th OFDM symbol has dimensions  $M_R N \times M_T N$ , with  $N$  the number of subcarriers and with  $\mathbf{G}_{k,i,j}$  representing the channel frequency response between the  $j$ -th transmit antenna and the  $i$ -th receive antenna;  $\mathbf{H}_k$ , with dimensions  $M_R N \times M_T N$ , is built in a similar fashion as  $\mathbf{G}_k$  but from the  $N \times N$  submatrices with the channel impulse response between each antenna pair during the  $k$ -th OFDM symbol after discarding the guard interval; and  $\mathbf{z}_k = (\mathbf{I}_{M_R} \otimes \mathbf{F}) \mathbf{w}_k$ . Under a doubly-selective channel, each of the  $\mathbf{G}_{k,i,j}$  submatrices will have the same banded structure as in the Single-Input Single-Output (SISO) case, and consequently ICI will also affect neighbor subcarriers transmitted from other antennas.

## 2.3 WiMAX Physical Layer

Worldwide Interoperability for Microwave Access (WiMAX) is a Broadband Wireless Access technology that enables ubiquitous delivery of wireless broadband services to either fixed and/or mobile devices [50]. It is a technology based on the IEEE 802.16 standard for the delivery of last-mile wireless broadband access and it has been proposed as an alternative to cable and DSL. The name WiMAX was coined by the WiMAX Forum which was formed to promote conformity and interoperability of the standard [16].

In the year 2004, an edition of the 802.16 standards was published focused on defining waveforms and protocols for fixed broadband wireless access channels. This release was used as the foundation of the first WiMAX standard, known as ‘‘Fixed WiMAX’’, which used an OFDM-based physical layer for Point-to-Multipoint (PMP) and mesh communications [45]. In 2005, the 802.16e provided a revised standard including a new physical layer based on Orthogonal Frequency Division Multiple Access (OFDMA), which allowed for the integration

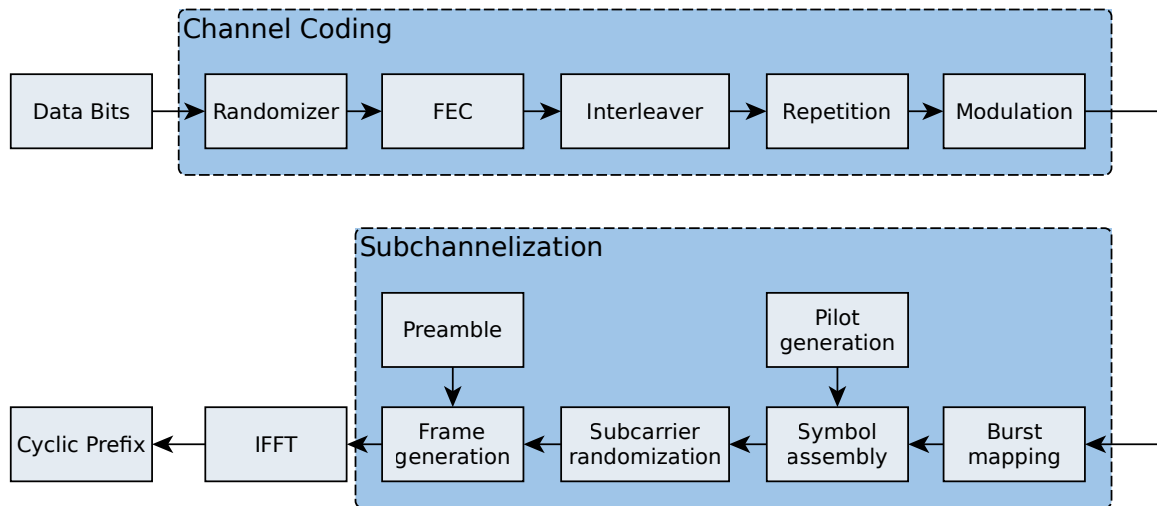


Figure 2.2: Block diagram of an IEEE Std 802.16e transmitter.

WiMAX profile	Channel Bandwidth	FFT size
# 1	3.5 MHz	512
# 2	5 MHz	512
# 3	7 MHz	1024
# 4	8.75 MHz	1024
# 5	10 MHz	1024

Table 2.1: WiMAX profiles.

of more advanced techniques such as MIMO, Low Density Parity Check (LDPC) codes, and Hybrid Automatic Repeat Request (H-ARQ) [43]. This promoted a new version of WiMAX, known as “Mobile WiMAX”, a new standard capable of providing data delivery for users in mobility scenarios.

A frame in the OFDMA physical layer under the Time-Division Duplexing (TDD) configuration consists of a downlink subframe from the base station to the mobile stations, and an uplink subframe. A subframe is in turn built up of data bursts, which are generated by channel encoding the information bits. This whole process is summarized in Figure 2.2.

The channel coding procedure has five steps: randomization, Forward Error Correction (FEC), bit-interleaving, repetition coding, and modulation. There are several FEC encoding methods supported by the WiMAX PHY layer: Convolutional Coding (CC), Convolutional Turbo-Coding (CTC), Block Turbo-Coding (BTC), and Low Density Parity Check (LDPC). Each burst can be encoded using any of these techniques. Variable coding rate and modulation are supported to enable Adaptive Modulation and Coding (AMC) capabilities. Each burst

is mapped to the time-frequency grid defined by the OFDM symbols in a subframe, usually defining rectangular-shaped regions allocated for each burst. Furthermore, each burst is divided into slots, composed by 48 data subcarriers, and each slot contains two subchannels of 24 data subcarriers, each subchannel mapped to two different consecutive OFDM symbols. Channel encoding is done at the slot level, hence the size of any burst is a multiple of one slot.

The downlink subframe is composed of one OFDM symbol for the preamble followed by a series of OFDM symbols with a defined structure of pilots and data. The preambles are generated using a pseudo-noise (PN) sequence, which is unique for each cell and segment combination. These parameters are needed to decode any frame, particularly during pilot demodulation. In the preamble, there is one pilot every three subcarriers in the frequency domain, thus, in the time domain, this symbol has a structure with three repetitions with a phase offset. After the preamble, the 802.16e standard defines several structures for burst mapping and pilot allocation, where Partial Usage of Subcarriers (PUSC) and Full Usage of Subcarriers (FUSC) are the two most prominent examples.

A downlink subframe also consists of several zones of symbols. Each one has a different symbol structure, but at least one PUSC zone must exist. This PUSC zone has two symbols reserved to send the downlink map (DL-MAP), which contains information about the subframe structure and the different bursts of data mapped into the zones. The first burst sent in these two symbols, known as the Frame Control Header (FCH), is encoded with a convolutional rate 1/2 encoder, followed by a repetition rate 1/4 encoder, and modulated using 4-QAM. This burst carries information about how the DL-MAP is encoded, and the DL-MAP does the same for the bursts and zones of the subframe.

In addition, there are requirements at the profile level. WiMAX Forum defines profiles with different bandwidths and number of subcarriers (see Table 2.1). The size of the cyclic prefix is also variable, with sizes ranging from 1/4 to 1/32 of the symbol length.

### **2.3.1 WiMAX Advanced**

In 2011, the WiMAX standard evolved to amendment 802.16m [44, 65] which focuses on enhancements related to air-interface specifications to fulfill the requirements and performance goals established by IMT-Advanced while maintaining full backward compatibility with previous WiMAX versions. In August 2012, the latest revision of WiMAX was published and termed 802.16-2012 [2]. This revision consolidates material from amendments 802.16j-2009 and 802.16h-2010, and also incorporates 802.16m-2011 but excluding the WirelessMAN-Advanced Air Interface, which is now specified in the IEEE Std 802.16.1-2012 [1].

The IEEE 802.16m standard introduces a completely new definition of the Physical layer (PHY) known as Advanced Air Interface (AAI). The configurability of the parameters is reduced to a large extent, but additional features like MIMO and H-ARQ are now mandatory

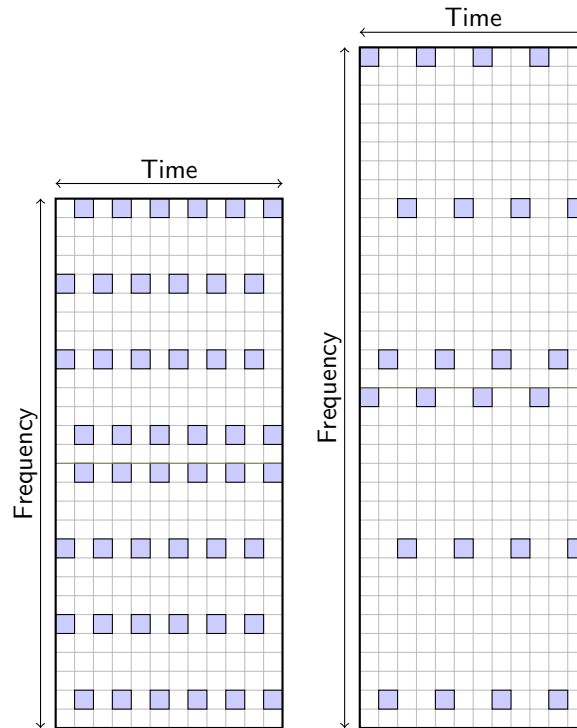


Figure 2.3: Examples of pilot patters in Mobile WiMAX for the PUSC SISO zone (left-hand side), and WiMAX Advanced for SISO (right-hand side). Pilot subcarriers are marked as blue, while the remaining are allocated to data.

to accomplish the minimum requirements of the standard, and also backward compatibility is mandatory. As an example, pilot patterns for 12 consecutive OFDM symbols in Mobile WiMAX and WiMAX Advanced are shown in Figure 2.3, with the pilot patterns for the PUSC zone in Mobile WiMAX (although more zones are defined) and the unique pilot pattern used in WiMAX Advanced for SISO transmissions.

A new profile with a channel bandwidth of 20 MHz and 2048 subcarriers is added, while the 3.5 MHz profile is discarded. The new frame structure is divided into superframes of 20 ms. Each superframe is made up of four 5 ms frames. The main difference with respect to the old frame structure is the way the frames are subdivided into subframes to increase the flexibility of the allocation of downlink and uplink zones. Each subframe can be dynamically configured for downlink or uplink transmission. This dynamic behaviour imposes the need to improve the *Frame Control* block to be more flexible.

The synchronization mechanisms have been improved by defining two new preambles: the PA-preamble, with a fixed number of pilot subcarriers regardless the Fast Fourier Transform (FFT) size to be used by the Advanced Base Station (ABS), and the SA-preamble with a structure and purpose similar to the preamble of the previous release.

The new subchannelization scheme is designed to simplify the channel estimation, to reduce

the signaling overhead required for the burst placement, and it only depends on the MIMO scheme at use.

The AAI defines new MIMO configurations to support Single User MIMO (SU-MIMO) and Multiple User MIMO (MU-MIMO) schemes, both with adaptive and non-adaptive precoding. The WiMAX Forum defines the minimum number of ABS antennas as two, while the Advanced Mobile Station (AMS) can operate with a single antenna. This leads to the need for replicating processing in transmit and receive chains only in the ABS.

Channel coding in 802.16m only uses two FEC schemes. On the one hand, Convolutional Turbo Codes (CTC) is the encoder defined to transmit the data bursts. On the other hand, a Tail-Biting Convolutional Codes (TBCC) encoder with rate 1/5 is used to encode the control information. In this case, it would be necessary to implement two encoding and decoding algorithms inside the FEC processing block. The mandatory H-ARQ processing can be addressed inside the *PHY Control* task.

## 2.4 Conclusions

In this chapter, the OFDM waveform and its behavior under synchronization errors and time-varying channels have been described. Regarding synchronization, timing offset errors are not critical since they translate into a subcarrier-dependent phase offset, and can be assimilated by the channel estimator. However, fractional carrier frequency offsets and time-varying channels introduce ICI between subcarriers. Thus, the assumption that the channel matrix is diagonal does not longer hold, and banded-like channel matrices are observed, demanding for specific estimation and equalization algorithms to remove the interference caused by ICI. Finally, a brief summary of Mobile WiMAX and Advanced WiMAX as examples of OFDM-based physical layers has been provided.



---

## Chapter 3

# SDR Architecture for OFDMA

Hardware implementations of communication systems are usually classified into three large groups [19, 66]: demonstrators for showing the feasibility of some technology; prototypes for an eventual development of a product aimed to the end-user; and testbeds which provide more flexibility than demonstrators and prototypes, and are of special interest for the research community to perform rapid experimental testing of algorithms and techniques.

The implementations of real-time communication systems have usually relied on specific hardware equipment, which turned out to be quite inflexible. This problem is usually circumvented by employing specific chips for each wireless technology. Alternatively, with the help of Field Programmable Gate Arrays (FPGAs) and Digital Signal Processors (DSPs), it is possible to implement real-time systems where a large share of the workload is completed by software algorithms. These technologies provided the foundations for the Software Defined Radios (SDRs) [59–61], of special interest in military applications, where real-time reliable communications and high reconfigurability are required. They are also useful in the research field, where this hardware can be used to develop sophisticated testbeds without losing flexibility.

In this chapter, an architecture for real-time Orthogonal Frequency Division Multiplexing (OFDM)-based physical layers will be described, intended to be deployed in SDRs. The downlink of the WiMAX standard will be used as a reference for the architecture, which is based on the Orthogonal Frequency Division Multiple Access (OFDMA) physical layer defined in the IEEE 802.16e document [43]. In the literature, most works focus on non-real-time deployments and performance evaluation of WiMAX Physical layer (PHY) (see [42, 57, 62] as an example). Other works focus on real-time implementations considering simplex communications, either downlink [23, 33] or uplink [93]. References exist that present the results of several tests in real scenarios to compare the channel models to the obtained data. As an example, path-loss measurements conducted in a rural environment using Fixed-WiMAX commercial equipment are presented in [46] and tests in outdoor scenarios using commercial Mobile-

WiMAX equipment are shown in [95]. Another example is [28] where a performance analysis of the 802.16e OFDMA downlink in vehicular environments (ITU-R M.1225) is shown.

Implementations of individual processing blocks of the WiMAX standard are readily available, but not integrated in a complete system. As an example, the design of a channel encoder prototyped in a reconfigurable hardware architecture is presented in [20]. Another example is a FPGA architecture of a fixed sphere decoder for a WiMAX system presented in [52]. There are some implementations that aim to support two standards by extracting common signal processing between them and sharing hardware resources, like the study of a dual-mode baseband receiver for 802.11n and 802.16e [40], and a 802.16m and LTE downlink implementation [41]. Although most of this chapter focuses on Mobile WiMAX, it will also be explained how the proposed architecture can be used to implement the recently standardized WirelessMAN-Advanced Air Interface.

This chapter is partly based on the publications [22, 82] and is organized as follows. Section 3.1 describes the proposed hardware architecture for the implementation of a Single-Input Single-Output (SISO) OFDMA-Time-Division Duplexing (TDD) PHY compliant with the Mobile-WiMAX standard. Section 3.1.7 explains how the proposed hardware architecture can be used to implement the PHY of the WirelessMAN-Advanced Air Interface. Finally, Section 3.2 presents the concluding remarks.

## 3.1 Mobile WiMAX Physical Layer Design

This section describes the design of an OFDMA-TDD PHY compliant with the Mobile WiMAX standard. The design focuses on the mandatory parts of the standard for both the Base Station (BS) and the Mobile Station (MS), i.e., OFDMA frame structure, Partial Usage of Subcarriers (PUSC) permutation scheme, and channel coding with Tail-Biting Convolutional Codes (TBCC).

Figure 3.1 plots the block diagram of the PHY architecture, which will be described in detail in the next subsections. Also, these tasks were eventually mapped to hardware modules (FPGAs and DSPs), and the placing of each task is also shown in the figure.

DSPs are specialized microprocessors with an instruction set designed to optimize common signal processing tasks. From a development perspective, coding, debugging and optimization of algorithms for a DSP is similar to that for a general purpose microprocessor. In this line, some of its advantages are low compilation times, development in high-level and general-purpose programming languages such as C, and flexibility to extend and refactor existing algorithms. On the other hand, FPGAs are reconfigurable circuits whose potential processing power is much higher than that of the DSPs, but comes at the expense of a larger development cost. An FPGA is usually programmed in hardware description languages such as VHDL or Verilog with very

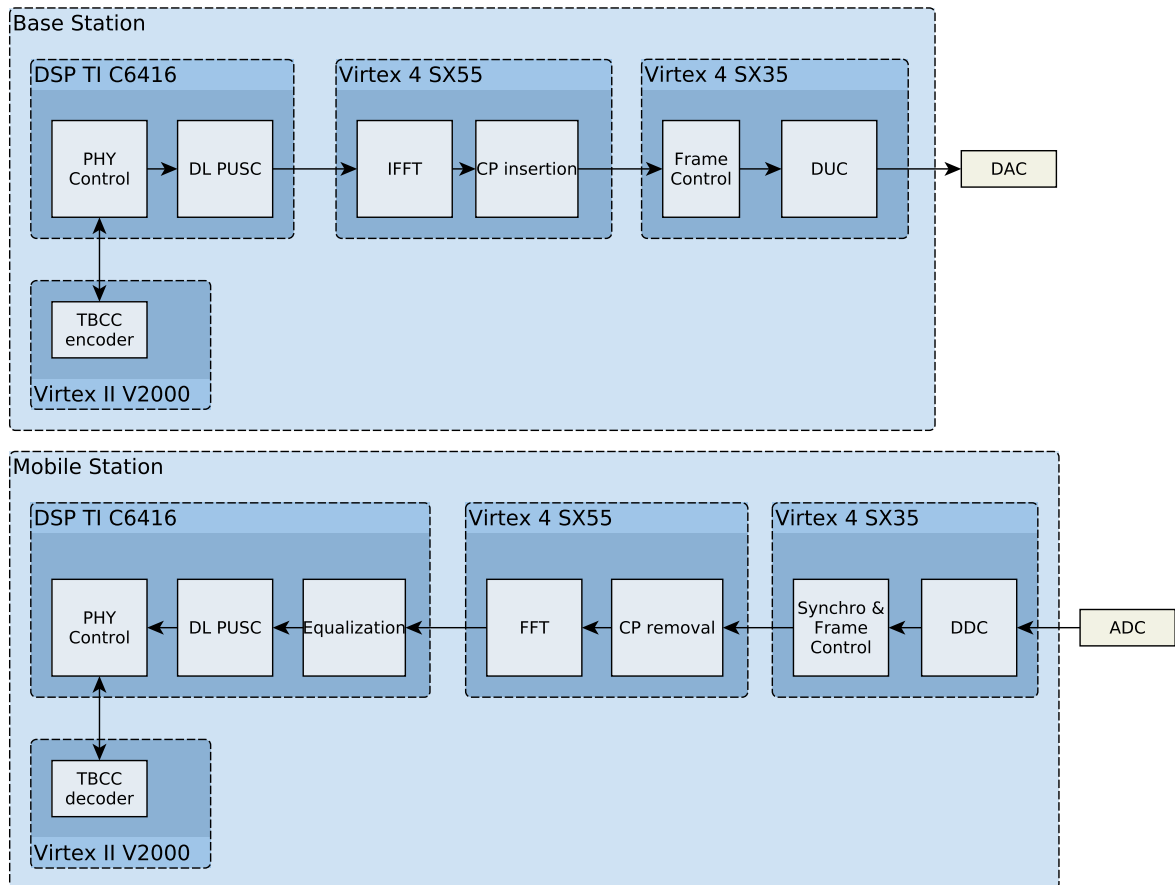


Figure 3.1: Global architecture of the base (top) and mobile (bottom) stations including the downlink building blocks. TI C6416 is a DSP model of Texas Instruments [8]; and Virtex II V2000, Virtex 4 SX55, and Virtex 4 SX35 are FPGA models from Xilinx [11, 12].

high compilation times, providing very specific and powerful designs, but rather rigid.

The main advantage of the previously described hardware architecture is its flexibility, enabling us to meet the requirements of both signal processing operations and high-level control logic demanded by the distinct elements of the software design. The kernel of the architecture is constituted by the DSP. It is responsible of executing higher-level tasks which requires the highest degree of freedom and the most complex operations, as well as controlling the executions in the remaining elements of the system (mainly the tasks running in the different FPGAs).

#### 3.1.1 Digital Up/Downconversion

The Digital Up Converter (DUC) and the Digital Down Converter (DDC) are responsible for adapting signals to the Analog-to-Digital Converters (ADCs) and Digital-to-Analog Converters (DACs) sampling rate and I/Q modulation/demodulation. During upconversion the following tasks are done: upsampling, pulse shaping, and I/Q modulation to a configurable intermediate frequency. The downconverter performs the complementary operations in reverse order, i.e. I/Q demodulation, filtering and downsampling.

#### 3.1.2 Frame control

Figure 3.1 shows blocks of frame control both in the BS and the MS, in the latter case integrated with the synchronization block. In the BS this task is responsible for the effective transmission of the downlink subframe. The WiMAX standard provides strict time delivery constraints for the TDD mode. Specifically, a delay of 5 ms between the beginning of two consecutive downlink subframes is mandatory. The duration of a downlink subframe is in the range of 2.8-3.5 ms, and the remaining time is shared with the transmission of the uplink. Taking this into account, the frame control task in the MS accepts samples for the duration of the downlink subframe, and it could be eventually extended to control the delivery of the uplink in the silence periods assigned by the BS to its transmission by the MSs.

#### 3.1.3 Downlink Synchronization

Frame and symbol detection are key operations to be performed at the MS. In the herein proposed design, frame and symbol detection are carried out using the correlation properties of the preamble and the WiMAX OFDM symbols, respectively. Figure 3.2 plots the block diagram of the synchronization subsystem implemented in the MS.

Since ADCs are not equipped with a Programmable Gain Amplifier (PGA), normalization of the received signal is performed after the DDC stage. This is done by first computing the average power of the received signal and then applying the resulting value as a constant scale

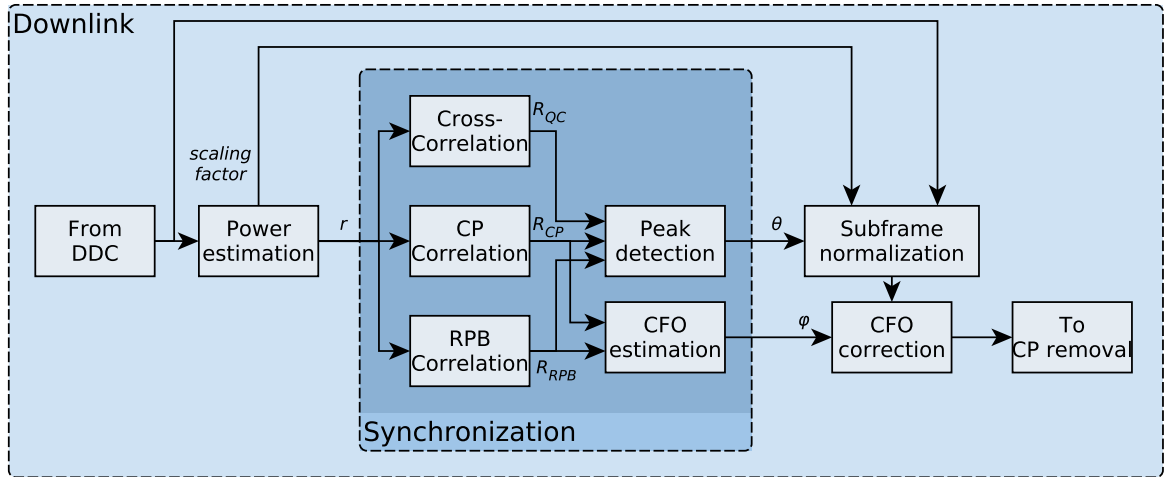


Figure 3.2: Downlink frame detection and synchronization subsystem implemented in the MS.

factor during the whole downlink subframe after synchronization. This normalization strategy has been selected because it provides a good compromise between clipping and quantization errors. The energy estimations computed during the first 1024 samples after the preamble and during the Receive/transmit Transition Gap (RTG) guard interval are stored to eventually estimate the Signal-to-Noise Ratio (SNR).

Preambles in Mobile WiMAX have a fixed structure with two guard subcarriers inserted between each pilot subcarrier whose values are chosen from a predefined set depending on the segment and the BS cell identifier. This structure results in a threefold repetition of samples in the time domain that can be exploited to detect the beginning of a new frame through the following Repetition Property Based (RPB) autocorrelation metric [49]

$$R_{RPB}[t] = \frac{3}{N} \sum_{n=0}^{N/3-1} r[t+n]r^*[t+n+N/3],$$

where  $r[t]$  is the complex-valued baseband received signal and  $N$  is the Fast Fourier Transform (FFT) size. When the preamble of a downlink frame is received, this metric reaches its maximum value and keeps this value during a plateau. The presence of this plateau indicates the incoming of a new downlink frame. The particular sample at which the FFT window starts can be determined making use of two additional metrics. The first one is the Cyclic Prefix (CP) autocorrelation metric defined as

$$R_{CP}[t] = \frac{1}{G} \sum_{n=0}^{G-1} r[t+n]r^*[t+n+N],$$

where  $G$  is the length of the CP. The second metric is the Quantized Cross-correlation (QC) that calculates a cross-correlation between the quantized received signal  $\tilde{r}[n]$  and the last 64

quantized preamble samples in the time domain,  $\tilde{p}[k]$ , i.e.,

$$R_{\text{QC}}[t] = \frac{1}{64} \sum_{n=0}^{63} \tilde{r}[t+n] \tilde{p}^*[t+n].$$

Quantization consists of mapping the input signal and the preamble into  $-1$ ,  $0$ , and  $1$  values to avoid the use of complex multipliers and reduce correlation calculation complexity.

The previously defined three correlation metrics are combined together to determine the frame starting time,  $\hat{\theta}$ , as follows

$$\hat{\theta} = \arg \max_t (|R_{\text{RPB}}[t]|^2 \cdot |R_{\text{CP}}[t]|^2 \cdot |R_{\text{QC}}[t]|^2).$$

Notice that, since the received input signal is normalized, the timing offset can be easily determined at the sample where this function overcomes a predefined threshold value.

The autocorrelation metrics  $R_{\text{RPB}}[k]$  and  $R_{\text{CP}}[k]$  can also be used to obtain estimates of the frequency offset. Indeed, two frequency offset estimations,  $\hat{\phi}_{\text{RPB}}$  and  $\hat{\phi}_{\text{CP}}$ , can be obtained by normalizing the phase of the autocorrelation metrics at the frame starting time,  $\hat{\theta}$ , with respect to the subcarrier spacing [76], i.e.,

$$\hat{\phi}_{\text{RPB}} = \frac{3 \cdot \text{angle}(R_{\text{RPB}}[\hat{\theta}])}{2\pi N}, \text{ and}$$

$$\hat{\phi}_{\text{CP}} = \frac{\text{angle}(R_{\text{CP}}[\hat{\theta}])}{2\pi N}.$$

These two values can be successfully combined to enhance the accuracy of the frequency-offset estimate. The preamble autocorrelation frequency-offset estimate  $\hat{\phi}_{\text{RPB}}$  provides a frequency-offset window in which the exact value can be determined from the CP autocorrelation frequency-offset estimate,  $\hat{\phi}_{\text{CP}}$ . In a general form

$$\hat{\phi}_{\text{COMB}} = \hat{\phi}_{\text{CP}} + \arg \min_k (|\hat{\phi}_{\text{CP}} + k/N - \hat{\phi}_{\text{RPB}}|) / N, \text{ for } k = -2, -1, 0, 1, 2,$$

where  $\hat{\phi}_{\text{COMB}}$  is the combined frequency-offset estimation. In the above expression, the frequency-offset estimation range of  $\hat{\phi}_{\text{CP}}$  goes from  $-\frac{1}{2N}$  to  $\frac{1}{2N}$ , while  $\hat{\phi}_{\text{RPB}}$  ranges from  $-\frac{3}{2N}$  to  $\frac{3}{2N}$ . When  $\hat{\phi}_{\text{CP}}$  is out of its range, its value should be adjusted by adding or subtracting multiples of  $1/N$  until it matches the value obtained with the  $\hat{\phi}_{\text{RPB}}$  metric.

### 3.1.4 Subchannelization and Channel Equalization

Subchannelization in WiMAX involves three operations: interleaving, randomization of subcarriers according to some permutation scheme, and pilot insertion. This structure is specified in the downlink map (DL-MAP) and uplink map (UL-MAP) messages sent by the BS in each frame. As described in Section 2.3, the DL-MAP message is always mapped onto

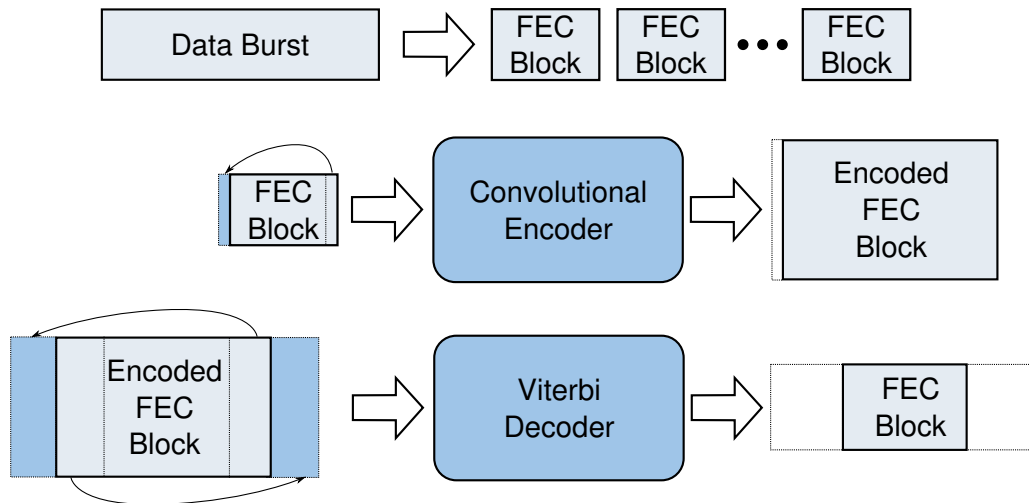


Figure 3.3: Operation of the convolutional coding and decoding with tail-biting.

the first two symbols of the downlink subframe, hence providing a complete description of the permutation schemes used and bursts contained inside the subframe. At the receiver, the task of decoding DL-MAP messages showed itself as a critical one since most of the processing of the downlink subframe at the receiver cannot start until this message is completely decoded.

Taking these issues into account, subchannelization and channel equalization processes were implemented in the DSPs to provide maximum flexibility regarding FFT sizes, burst mapping, and eventual support of other permutation schemes. In the MS, the extraction of DL-MAP messages is optimized through the different design layers to minimize the delay of the decoding pipeline rather than implementing a hardware low-level Medium Access Control (MAC) for this purpose [25].

The selected channel estimation algorithm was piecewise linear interpolation of the channel coefficients estimated at the pilot positions, and the equalization algorithm was zero-forcing. Several analysis of channel estimation and equalization algorithms for WiMAX can be found in the literature showing that the selected method offers an acceptable performance in terms of Mean Squared Error (MSE) and Bit Error Ratio (BER) with a low complexity implementation [70, 94].

### 3.1.5 Channel Coding

Information bits received from higher layers are mapped into constellation points after a channel coding process that includes randomization and bit interleaving. Additionally, the repetition coding step is performed over the constellation-mapped data in a slot by slot manner. Recall that, as explained in Section 2.3, a slot is the minimum size of a burst, corresponding to 48 data subcarriers. In the proposed design, channel coding is mainly implemented in the Virtex-II FPGA, although the optional repetition coding step and the processing control are carried out

in the DSP, using the FPGA as a coprocessor. In this work we focus on the TBCC coding scheme with variable rate and constellation sizes from QPSK, 16-QAM, and 64-QAM, both in the downlink and in the uplink.

The encoder in a tail-biting scheme has a complexity similar to that of a zero-tail encoder, and an overview of the encoding and decoding process is shown in Fig. 3.3. At the encoding side, the data bursts are first split in FEC blocks of the same size, and then each block is encoded independently. This process is reversed after decoding. The encoder was implemented adding a CP to each Forward Error Correction (FEC) block with a size equal to the constraint length of the shift register (in the case of Mobile WiMAX this value is seven). The decoder has a higher complexity because the starting state of the trellis is unknown before decoding. Maximum Likelihood (ML) decoding achieves optimum performance but it requires decoding the received block starting with all the possible initial states, which increases decoding complexity to unacceptable levels [29]. The implemented channel decoding process uses a suboptimal technique which provides a good compromise between decoding quality and complexity, where the first bits of the block are appended after the block and the last bits are appended at the beginning of the block [34]. The size of the chunks added at the beginning and at the end of the blocks is equal to the traceback length configured in the Viterbi decoder. If a block is shorter than the traceback length, it is just sent three times to the decoder and only the output corresponding to the second repetition is taken into account.

Additionally, the decoder performs a Carrier-to-Interference and Noise Ratio (CINR) estimation based on the demodulated data symbols by estimating the Error Vector Magnitude (EVM). This estimation was implemented in the soft-decoder by mapping the soft-bits back to symbols, hence obtaining a reliable estimation of the transmitted symbols. Then, the MSE between the received signal and the estimated transmitted symbol is calculated and saved in a register in order that the DSP subsequently reads this value. This algorithm provides an accurate estimation of the CINR as long as decision errors are kept at low levels. If this is not the case, an overestimation of the CINR will occur.

#### 3.1.6 Physical Layer (PHY) Control

The subframes structure is controlled from the higher layers in the BS using a Service Access Point (SAP) protocol and is sent to the MS through MAC-management messages (DL-MAP, UL-MAP, Downlink Channel Descriptor (DCD), and Uplink Channel Descriptor (UCD)). This SAP is based on the protocol defined by Intel for its BSs [14] and properly extended to support the particular features of the MSs. This SAP allows for defining the subframes structure, and for sending and receiving data bursts.

The downlink subframe must follow some constraints regarding the permutation zone and burst definitions. First of all, bursts must be time-frequency rectangular-shaped, and should

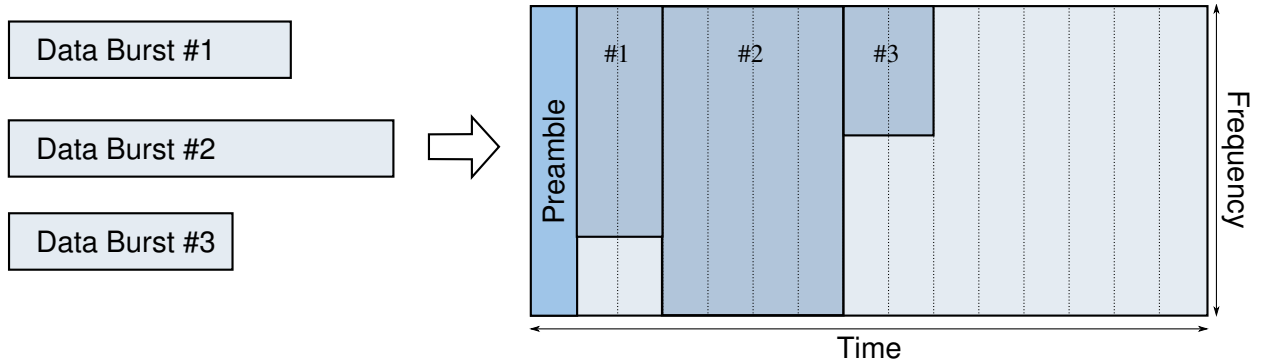


Figure 3.4: Mapping of data bursts to the downlink subframe with the Ohseki algorithm.

always span a multiple of two symbols in time and a multiple of a subchannel size in frequency (this is the so-called slot unit according to WiMAX terminology). Moreover, several users can be grouped into a single burst to reduce overhead in the DL-MAP definition and to speed-up the generation of bursts. Finally, the BS has to distribute the available resources between users taking into account their Quality of Service (QoS) requirements.

There are several solutions to face these problems [80] but in our implementation the Ohseki algorithm [68] was chosen because of its good compromise between computational complexity and allocation losses. In Fig. 3.4 this algorithm is sketched out. The general idea is to assign all users with equal burst profile to the same burst, and to allocate its resources in a frequency-first policy, hence avoiding any burst overlapping in the frequency domain.

### 3.1.7 Advanced WiMAX

The proposed architecture can be readily adapted to give support to an implementation of the Advanced Air Interface (AAI). As an example, an adaptation of the architecture is shown in Figure 3.5 in which an Advanced Base Station (ABS) and an Advanced Mobile Station (AMS) are configured to support a  $2 \times 1$  Multiple-Input Multiple-Output (MIMO) scheme, which would require an increase of hardware resources to support the implementation of the new functionalities. The *Frame Control*, *Synchronization*, and *FFT/IFFT* blocks must be enhanced to support the new subframe structure. The new subchannelization scheme can be implemented in the same DSP as the old *PUSC* blocks, as well as the channel equalization step. The ABS MIMO requirements impose the need for replicating the transmit and receive chains, forcing an increase of hardware resources in the FPGA and in the DSP modules since they have to implement the new precoding techniques. Also, the Hybrid Automatic Repeat Request (H-ARQ) technique requires an increase in memory due to the need for storing the received bursts. Finally, the new FEC schemes have to be implemented in a larger FPGA as the Virtex-II has not enough resources.

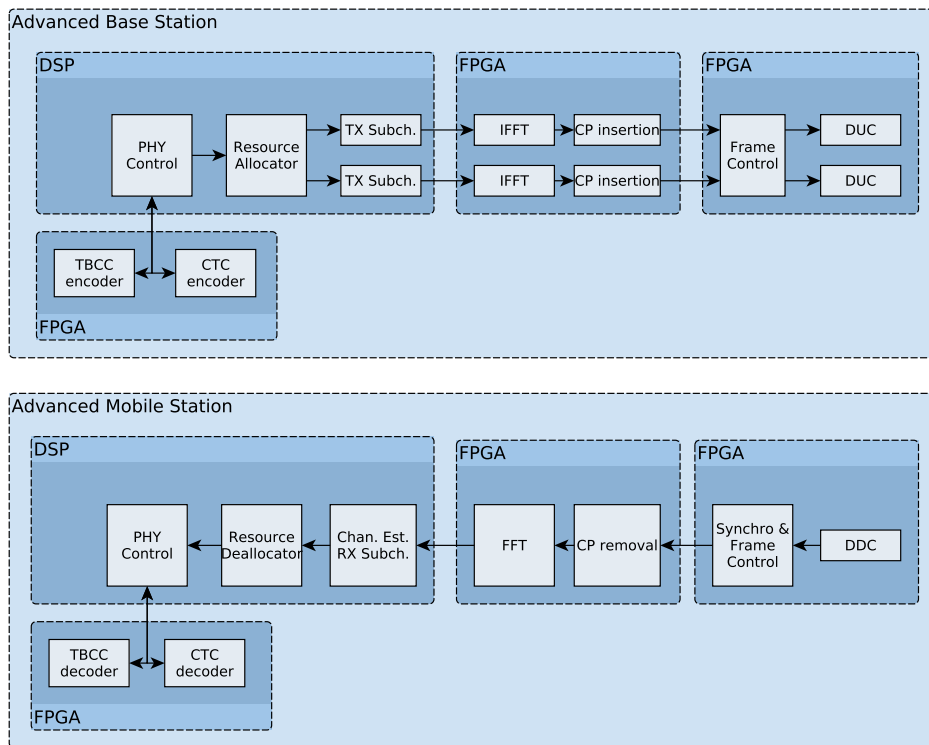


Figure 3.5: Proposed 802.16m architecture.

## 3.2 Conclusions

In this chapter, the design and implementation of real-time OFDMA-TDD PHYs compliant with the WiMAX standard has been addressed. Moreover, the different design decisions adopted to accomplish this stringent objective have been explained. Finally, the utilization of the proposed hardware architecture to implement the WirelessMAN-Advanced Air Interface is also discussed.

---

## Chapter 4

# Evaluation of the Proposed OFDMA SDR Architecture under Doubly-Selective Channels

In this chapter, evaluation techniques and results of several tests that were conducted will be described to evaluate the performance of the proposed Single-Input Single-Output (SISO) Orthogonal Frequency Division Multiple Access (OFDMA)-Time-Division Duplexing (TDD) WiMAX Physical layer (PHY) architecture described in Chapter 3. In order to carry out the evaluation in a repeatable as well as in a reproducible way, we set up an evaluation system that uses a real-time channel emulator that implements different time-varying channel models.

This chapter is partly based on the publications [22, 82] and is organized as follows. Section 4.1 shows the details of the channel emulator implemented in programmable hardware, Section 4.2 show the results of the experiments carried out to validate the performance of the implemented architecture, and finally Section 4.3 contains the concluding remarks.

### 4.1 Channel emulator

Channel emulators are a convenient tool to evaluate the performance of communications hardware equipment. They provide a cost-effective mechanism to obtain realistic results of the behavior of a system without deploying measurement campaigns. It also has the advantage of making easier to control the scenario, avoiding interferences from other sources that can be observed in a field trial.

There are commercial channel emulators available in the market [4, 7], but in this work a custom-made emulator based on a Field Programmable Gate Array (FPGA) has been used. There are works in the literature where this kind of architectures have been used with satisfactory results [32].

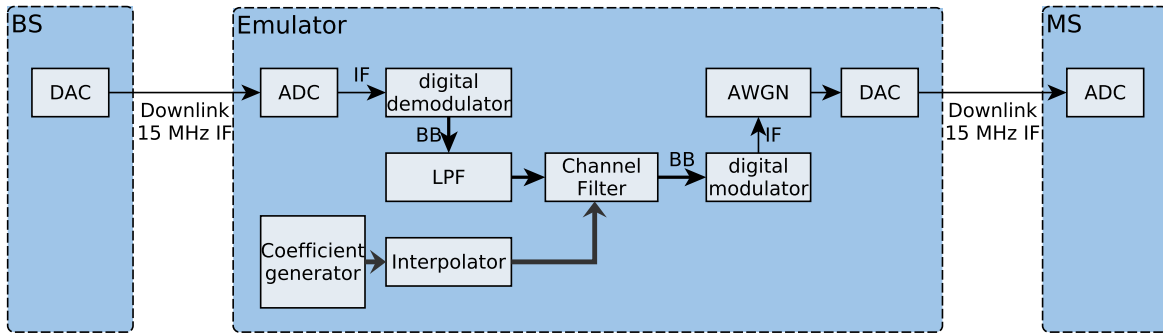


Figure 4.1: Block diagram of the OFDMA-TDD evaluation system configured to test the downlink.

Figure 4.1 plots the block diagram of the channel emulator. It consists of a channel coefficient generator, an interpolator, a channel filtering stage, and an Additive White Gaussian Noise (AWGN) generator. The emulator is configured to receive signals at an intermediate frequency (IF), which are downconverted to baseband (BB) to be processed, and then upconverted back to IF. It accepts parameters such as the average power and delay of each tap, the noise power, and the intermediate frequency of the input signal. The “Coefficient generator” block generates complex-valued Rice-distributed channel coefficients, according to the Jakes Doppler spectrum model. This generation is accomplished by filtering white Gaussian samples with the autocorrelation function associated with the Jakes model, which is done at a rate much lower than the input signal sampling rate. The “Interpolator” block is the responsible of adjusting the rates of the generated channel coefficients to that of the input signal.

The channel emulator was configured to implement the ITU-R M.1225 models [15]. Following the recommendations of the WiMAX Forum [17] four models were considered: Pedestrian A (3 km/h), Pedestrian B (3 km/h), and Vehicular A at 60 km/h and at 120 km/h. A summary of the tapped delay line features of these channel models is shown in Table 4.1.

All channel models use the Jakes Doppler power spectrum density and a 2.4 GHz carrier frequency was assumed for the Doppler spread calculations. The maximum delay of these channels ( $3.70 \mu\text{s}$ ) does not exceed in any case the default 1/8 Cyclic Prefix (CP) length ( $11.43 \mu\text{s}$ ), hence Intersymbol Interference (ISI) is avoided. It is important to note that the Pedestrian A scenario stands out because it has a low multipath diversity. Multipath diversity is an inherent property of wireless channels that occurs whenever the channel power delay profile is rich enough to provide replicas of the transmitted signal at the receiver input. In time varying scenarios, the amplitude and the phase of such replicas change over time. The Pedestrian A channel model only contains four paths with the last two being rather attenuated. Furthermore, the path delay spread is rather small so the frequency selectivity of this channel is rather low, hence allowing for a good channel equalization. On the contrary, notice that the Pedestrian B and Vehicular A scenarios have higher multipath diversity and larger path delay spreads.

	Pedestrian A	Pedestrian B	Vehicular A
Number of paths	4	6	6
Power gain of each path [dB]	0, -9.7, -19.2, -22.8	0, -0.9, -4.9, -8.0, -7.8, -23.9	0, -1.0, -9.0, -10.0, -15.0, -20.0
Path delay [ns]	0, 110, 190, 410	0, 200, 800, 1200, 2300, 3700	0, 310, 710, 1090, 1730, 2510
Speed [km/h]	3	3	60, 120

Table 4.1: ITU-R M.1225 channel models.

As explained in Section 3.1, Mobile Stations (MSs) estimate the SNR of the received signal using the values obtained during the synchronization process. These estimated SNR values were used to calibrate the AWGN generator, hence matching the noise power added in the emulator with the estimated SNR in the MS. This way, the SNR at the receiver is under control in all scenarios.

## 4.2 Results

### 4.2.1 Experiments under static scenarios

Tests under static scenarios were done, both by direct connection by cable and over the air using antennas. In the latter case, transmit and receive antennas were located with line-of-sight at a distance of 2 m between them. The RF tests were carried out using the Agilent VSG E4438C signal generator as upconverter and the ACSC-RX-5255 downconverter, built by the Spanish company Acorde Technologies. Figure 4.2 shows the setup of the hardware platform, with two computers configured as transmitter and receiver, along with the radio-frequency equipment. The carrier frequency used for these tests was 5.255 GHz. Error Vector Magnitude (EVM) measures were obtained from 100 frames made up of two OFDM symbols each, transmitted with a power value equal to -10 dBm. The EVM is calculated according to the following equation

$$\text{EVM}(\text{dB}) = 10 \log_{10} \left( \frac{\sum_{n=0}^{N-1} |D(\hat{x}_k[n]) - \hat{x}_k[n]|^2}{\sum_{n=0}^{N-1} |D(\hat{x}_k[n])|^2} \right),$$

where  $\hat{x}_k[n]$  are the received symbols after equalization, and  $D(\cdot)$  is the decider function which searches for the closest constellation point of the transmission alphabet. This measurement is an approximation of the SNR, but it can differ due to synchronization and channel estimation



Figure 4.2: Setup of the hardware platform during the radio-frequency measurements.

	3.5 MHz	5 MHz	7 MHz	8.75 MHz	10 MHz
IF	-40.70 dB	-37.88 dB	-40.83 dB	-40.70 dB	-37.42 dB
RF	-35.81 dB	-34.66 dB	-34.59 dB	-34.03 dB	-33.50 dB

Table 4.2: EVM levels for different profiles for intermediate frequency by cable and for over-the-air radio frequency transmissions using antennas separated 2 m.

errors, non-linear effects such as I/Q-imbalances, or due to wrong estimations of the ideal symbols  $I(i)$ .

Table 4.2 show the EVM values obtained, and it can be seen that high quality constellations are observed in this scenarios, with a 3-6 dB loss in the wireless scenario. As an example, Figures 4.3 and 4.4 show the constellations received for a sample transmission with 64-QAM.

#### 4.2.2 Experiments under emulated mobile scenarios

In this set of experiments, the channel emulator described in Section 4.1 was used. First of all, experiments were carried out to evaluate the performance of the frame detection stage. Towards this aim, at least  $10^4$  frames were transmitted in the downlink direction and the number of frames detected is counted at the MS. The frame detection performance over AWGN and ITU-R channels is shown in Figure 4.5 with 90% confidence intervals for the mean computed using bootstrapping [31]. The best results are clearly obtained over the AWGN channel, with

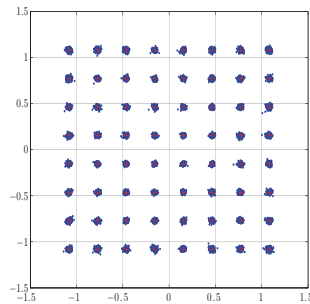


Figure 4.3: Constellation of the RF test with the profile of 8.75 MHz.

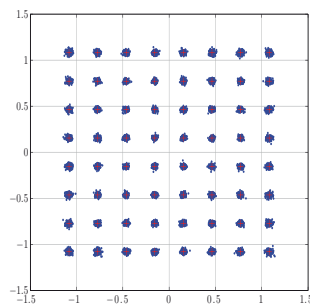


Figure 4.4: Constellation of the RF test with the profile of 10 MHz.

almost perfect detection at a SNR value of 0 dB. In the case of ITU-R channels, the performance degrades significantly due to channel fades. Similar results were obtained for Pedestrian B and Vehicular A channels where the SNR has to be increased up to 12 dB in order to achieve Frame Error Rate (FER) values below  $10^{-3}$ . The worst results were obtained for the Pedestrian A channel model because its multipath diversity is smaller than in the other channel models.

Regarding Bit Error Ratio (BER) performance, downlink measurements were done over the AWGN and the ITU-R channels. In order to measure the BER, a fixed and known structure of subframes was used. As explained in Section 2.3, the first two symbols of the downlink are reserved to deliver its structure with the messages Frame Control Header (FCH) and downlink map (DL-MAP). If any of these messages arrives corrupted to the MS, the downlink cannot be decoded. Defining a predefined burst structure, known in advance at the receiver, allows us to measure BER even when these messages are not decoded, although the undetected frames remain ignored regarding BER measurements. Figure 4.6 plots the coded BER with respect to the Signal-to-Noise Ratio (SNR) for the 3.5 MHz downlink profile when transmitting over an AWGN channel. As expected, curves are shifted to the right-hand side as the spectral efficiency increases.

Figure 4.7 shows the results of coded BER tests for the 8.75 MHz downlink profile considering the ITU-R channels. The lack of multipath diversity explains its poor performance at low and medium SNR values. At higher SNR levels, however, the results in Pedestrian A improve and outperform the others because its channel frequency response is easier to equalize.

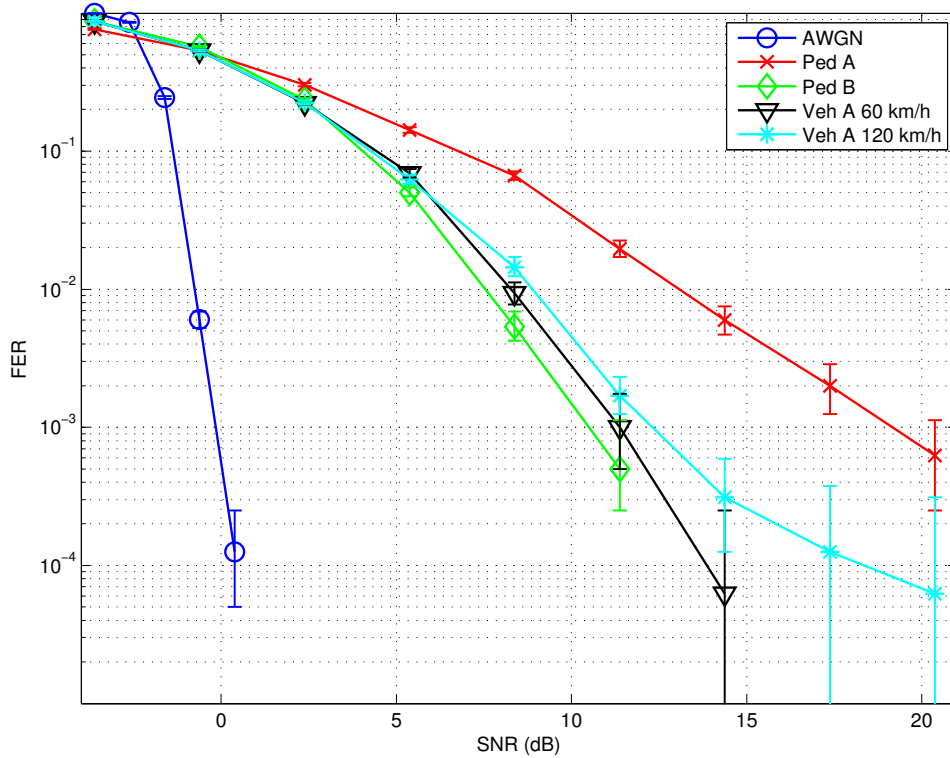


Figure 4.5: Downlink frame detection error rate in AWGN and ITU-R channels.

Regarding Vehicular A channel models, an error floor can be observed because channel estimation has not been designed to compensate for the Inter-Carrier Interference (ICI) generated by the channel fast time-variations. The ICI results in a source of noise for all subcarriers due to the loss of orthogonality between them, which produces the error floor appearing for the Vehicular A channel. Also, this error floor increases when considering higher speed scenarios, and it could be lowered if the channel estimation and equalization algorithms considered this effect of the channel.

Finally, Figures 4.8 shows the FER over the ITU-R channel models. These FER measurements are not affected by the undetected frames, contrarily to the previous FER measurements. The measured burst occupies 15 subchannels over 18 OFDM symbols, with a total of 6480 data subcarriers per downlink subframe. The FER results are consistent with the BER ones. The only significant difference is the worse results in the Pedestrian B caused by the higher frequency selectivity, which increases the probability of isolated errors in every burst. This leads to a higher FER but does not affect significantly the BER measurement. In general, the results of Pedestrian A are improved when the FER is measured since the erroneous bursts occur more often due to the lower multipath diversity.

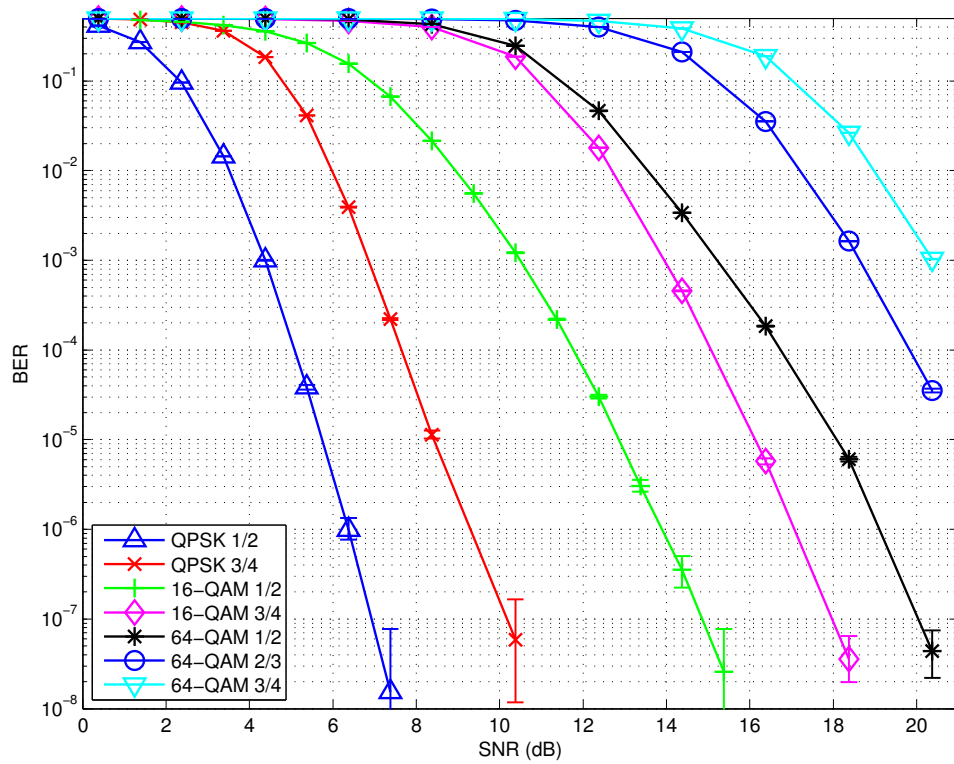


Figure 4.6: Coded BER over AWGN channel using the 3.5 MHz downlink profile.

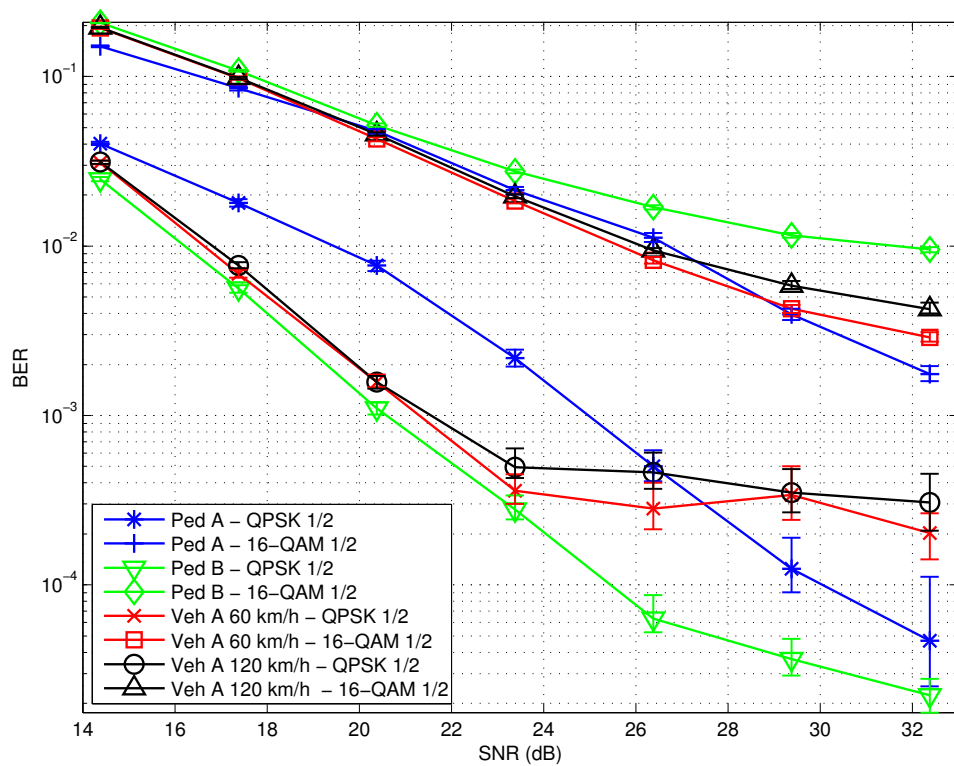


Figure 4.7: Coded BER over ITU-R channels using the 8.75 MHz downlink profile.

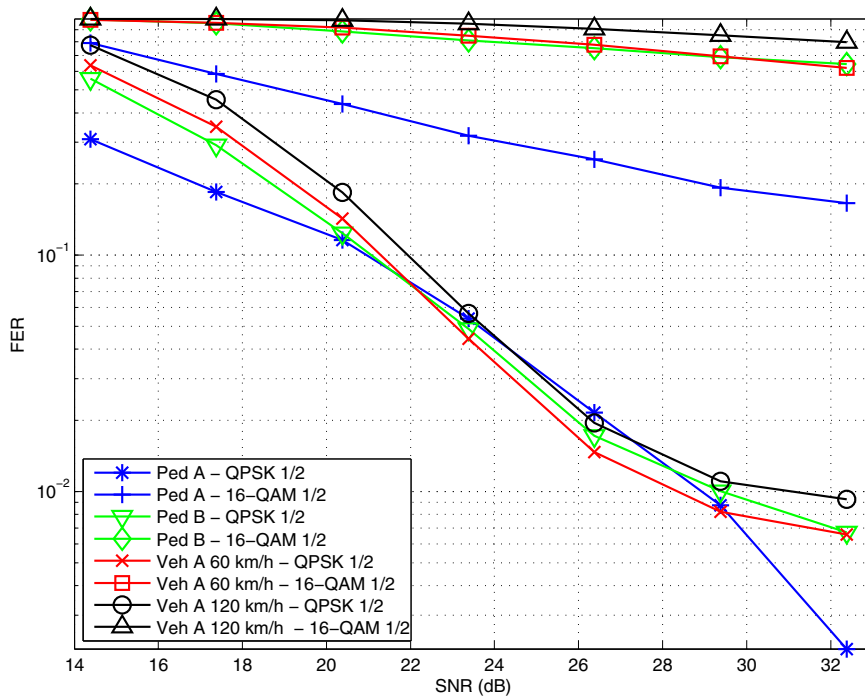


Figure 4.8: FER over ITU-R channel using the 8.75 MHz downlink profile. Bursts of 6480 bits for QPSK 1/2 and 12960 bits for 16-QAM 1/2.

### 4.3 Conclusion

In this chapter, results of the evaluation of the hardware architecture for the WiMAX PHY downlink described in the previous chapter have been shown. These tests were carried out with real transmissions over the wire, over the air, and over a channel emulator that emulates AWGN and ITU-R channels. Specific performance metrics that take into account the frame detection were considered to illustrate the adequate performance of the proposed design, as well as EVM, FER, and BER measurements.

---

# Chapter 5

## Estimation of MIMO-OFDM

### Doubly-Selective Channels

MIMO-OFDM is the transmission method adopted by the last generations of broadband wireless communication systems. MIMO-OFDM combines Multiple-Input Multiple-Output (MIMO) transmissions over multiple transmit and receive antennas together with Orthogonal Frequency Division Multiplexing (OFDM) modulation. The primary advantage of MIMO-OFDM is its ability to achieve large spectral efficiencies while equalizing frequency-selective channels with low-complexity receivers. Nevertheless, the performance of MIMO-OFDM degrades severely when transmitting over rapidly time-varying channels such as those encountered in high mobility applications. In MIMO-OFDM, fast channel time variations cause symbols received in an OFDM subcarrier to be affected by symbols in adjacent subcarriers. This harmful effect is known as Inter-Carrier Interference (ICI) and has to be estimated and compensated for MIMO-OFDM to perform adequately over rapidly time-varying wireless channels.

This chapter is partly based on the publications [83, 84], and the remainder of this chapter is organized as follows. Section 5.1 gives a brief review of the state of the art on ICI estimation and BEM design, Section 5.2 describes the signal model relevant for this chapter, based on that defined in Chapter 2, Section 5.3 focuses on the design of optimal BEMs for ICI estimation, and Section 5.4 shows simulation results. Finally, Section 5.5 concludes the chapter.

#### 5.1 State of the Art

In the literature, several works address ICI estimation in OFDM systems. Most of the proposed solutions make use of a Basis Expansion Model (BEM) in which the channel impulse response is decomposed as a linear combination of basis vectors in order to effectively reduce the number of coefficients to be estimated. As shown in (2.16), channel time variations are linearized

according to the basis vectors, which can be denoted in matrix form as

$$\mathbf{h}_{k,l} = \mathbf{B}\mathbf{c}_{k,l}, \quad (5.1)$$

where  $\mathbf{h}_{n,l}$  is a  $N \times 1$  vector with the time-variations of the  $l$ -th tap during the  $k$ -th OFDM symbol,  $\mathbf{B}$  is a  $N \times Q$  matrix with the basis vectors as columns, and  $\mathbf{c}_{n,l}$  is a  $Q \times 1$  vector containing the BEM coefficients. With this scheme, the  $N$  original channel parameters are reduced to  $Q$  for each tap.

Different BEMs have been proposed in the literature, being one of the first proposals the one based in Complex-Exponentials (CE-BEM) [35]. In this case, the matrix  $\mathbf{B}$  is defined as  $[\mathbf{B}]_{i,k} = e^{(j2\pi i/N)(k-\lfloor Q/2 \rfloor)}$ , which is equivalent to the columns of the DFT matrix corresponding to the frequencies in the interval  $[-Q/2, Q/2]$ . A variation of this BEM was proposed in [53] to obtain an oversampled version of the BEM coefficients. This variation defines the BEM as  $[\mathbf{B}]_{i,k} = e^{(j2\pi i/NO)(k-\lfloor Q/2 \rfloor)}$ , with  $O > 1$ , and is denoted in the literature as Generalized Complex Exponential BEM (GCE-BEM). Another popular approach is to approximate the channel by a  $Q$ -degree polynomial, with  $[\mathbf{B}]_{i,k} = (i+1)^k$ . This is referred to as Polynomial BEM (P-BEM) [92]. Finally, BEMs based on the statistics of the channel have been defined, being the two most prominent examples the Discrete Prolate Spheroidal BEM (DPS-BEM) [96], and the Karhunen-Loève BEM (KL-BEM) [89]. In the latter,  $\mathbf{B}$  is obtained by computing the  $Q$  most relevant eigenvectors of the channel covariance matrix, while the former is a particularization of the KL-BEM for the case of a flat Doppler spectrum.

ICI estimation using BEMs has been addressed for the case of Single-Input Single-Output (SISO)-OFDM, considering both single and multiple OFDM blocks [87, 88], as well as for MIMO-OFDM systems [81]. These works, however, assume a particular OFDM symbol structure in which clusters of pilot subcarriers are available in the frequency domain, and particularly the Kronecker delta model has been proved to be the optimal design under this estimation strategy [81]. Under this model, each pilot consists of a single symbol surrounded by null subcarriers, intended to minimize the interference received on that symbol from the unknown data symbols. On the one hand, this assumption is not typically found in most currently standardized wireless communication systems, such as LTE, in which pilots are typically placed in non-adjacent subcarriers. On the other hand, this technique impacts significantly on the spectral efficiency of the system since those additional null subcarriers do not convey user data.

Other works in the literature have specifically addressed ICI estimation in OFDM systems with arbitrary pilot structures using a two-step approach. In the first step a time-averaged channel impulse response estimation is computed for a group of OFDM symbols, and then these individual estimations are used in a second step to estimate the ICI. Least Squares (LS) polynomial fitting [37] and low-pass interpolation [38] have been proposed. Other approximations have considered the use of a LS interpolation based on a smoothness constraint

[58]. This scheme has been generalized to consider ICI estimation in MIMO-OFDM systems using a DPS-BEM [79].

The DPS-BEM has been shown to be optimum for time-varying channels with a flat Doppler spectrum. Nevertheless, only channels with a 3D model of the arrival paths exhibit a flat Doppler spectrum. For example, channel models for urban environments typically follow a symmetrical or asymmetrical Jakes' spectrum depending on the angle of arrival of the multipath components [97]. Non-flat Doppler spectrum shapes also appear in aeronautical [36] and satellite [69] channel models. Another example is the COST-207 channel model for GSM communications in mobile environments that utilizes a bi-Gaussian Doppler spectrum [13].

In this chapter a BEM obtained from a low-rank approximation to the Linear Minimum Mean Squared Error (LMMSE) estimation of the ICI is used in a MIMO-OFDM system. The proposed approach utilizes the individual frequency response estimations obtained from a frame of several consecutive MIMO-OFDM symbols without requiring any specific pilot subcarrier structure in the frequency domain. Information about the channel Doppler spectrum is incorporated into the LMMSE channel estimation while the Karhunen-Loève Transform (KLT) is used to obtain the low-rank approximation. The results of computer simulations show that the proposed BEM exhibits a superior performance when estimating the ICI originated by time-varying MIMO-OFDM channels with non-flat Doppler spectrum.

## 5.2 Signal Model

Recalling the signal model described in Section 2.1, and extended to the MIMO case in page 15, matrix  $\mathbf{G}_k$  is a block matrix built from the frequency response of the channel between each transmit-receive antenna pair

$$\mathbf{G}_k = \begin{pmatrix} \mathbf{G}_{k,1,1} & \mathbf{G}_{k,1,2} & \cdots & \mathbf{G}_{k,1,M_T} \\ \mathbf{G}_{k,2,1} & \mathbf{G}_{k,2,2} & \cdots & \mathbf{G}_{k,2,M_T} \\ \cdots & \cdots & \cdots & \cdots \\ \mathbf{G}_{k,M_R,1} & \mathbf{G}_{k,M_R,2} & \cdots & \mathbf{G}_{k,M_R,M_T} \end{pmatrix}, \quad (5.2)$$

where the timing and frequency offsets  $\theta$  and  $\epsilon$  are set to zero assuming these errors are negligible after synchronization, and consequently the matrices  $\boldsymbol{\varepsilon}_n$  and  $\boldsymbol{\Theta}$ , are equal to the identity matrix. If this were not the case, it can be interpreted that the synchronization offset effects are collected into the channel matrix, without estimating their particular value.

If the channels between the transmit and receive antennas are static, the individual frequency-domain channels  $\mathbf{G}_{k,i,j}$  have non-zero entries only on their main diagonal. However, if the channels are time-varying, non-zero off-diagonal entries will appear causing ICI between transmitted subcarriers and also between transmit antennas, as shown in Figure 2.1. In addition, recalling (2.8) and (2.10), a matrix  $\overline{\mathbf{G}}_{k,i,j}$  can be defined containing the elements of the main

diagonal of each of the matrices  $\mathbf{G}_{k,i,j}$  in  $\mathbf{G}_k$ , which corresponds to the time-averaged impulse response of the channel during the  $k$ -th OFDM symbol and the  $m$ -th subcarrier between the  $j$ -th transmit and the  $i$ -th receive antennas. The main diagonal elements of  $\overline{\mathbf{G}}_{k,i,j}$  are defined as

$$[\overline{\mathbf{G}}_{k,i,j}]_{m,m} = \frac{1}{N} \sum_{t=0}^{N-1} \sum_{l=0}^{L-1} h_{k,i,j}[t, l] e^{-j2\pi lm/N}. \quad (5.3)$$

Thus the channel frequency response can take the form

$$\mathbf{G}_{k,i,j} = \mathbf{F}(\overline{\mathbf{H}}_{k,i,j} + \Delta\mathbf{H}_{k,i,j})\mathbf{F}^H = \overline{\mathbf{G}}_{k,i,j} + \tilde{\mathbf{G}}_{k,i,j}, \quad (5.4)$$

where  $\mathbf{F}$  is the standard  $N \times N$  Discrete Fourier Transform (DFT) matrix, and  $[\overline{\mathbf{H}}_{k,i,j}]_{r,s} = \bar{h}_{k,i,j}[\text{mod}(r - s, N)]$ , with  $\bar{h}_{k,i,j}[l] = \frac{1}{N} \sum_{t=0}^{N-1} h_{k,i,j}[t, l]$  the time-averaged impulse response between the  $j$ -th transmit and  $i$ -th receive antenna for the  $l$ -th path after removing the cyclic prefix. Finally,  $\Delta\mathbf{H}_{k,i,j} = \mathbf{H}_{k,i,j} - \overline{\mathbf{H}}_{k,i,j}$  contains the variations of the channel relative to the average of the channel coefficients during the OFDM symbol. Since  $\overline{\mathbf{H}}_{k,i,j}$  is a circulant matrix,  $\overline{\mathbf{G}}_{k,i,j}$  is a diagonal matrix with the time-averaged channel frequency response whose elements are, according to (2.8) and (5.3),  $[\overline{\mathbf{G}}_{k,i,j}]_{m,m} = G_{k,i,j}[m]$ , and  $\tilde{\mathbf{G}}_{k,i,j}$  contains the ICI component of the frequency response. A receiver that ignores ICI will only estimate the elements contained in the main diagonal of  $\overline{\mathbf{G}}_{k,i,j}$ , treating the remaining components generated by  $\tilde{\mathbf{G}}_{k,i,j}$  as noise.

Finally, the received signal can be written as

$$\mathbf{y}_k = \overline{\mathbf{G}}_k \mathbf{x}_k + \underbrace{\tilde{\mathbf{G}}_k \mathbf{x}_k}_{\text{ICI}} + \mathbf{z}_k, \quad (5.5)$$

where  $\mathbf{x}_k = \mathbf{D}_k \mathbf{d}_k + \mathbf{P}_k \mathbf{p}_k$  contains the  $NM_T$  subcarriers transmitted in the  $k$ -th OFDM symbol. Such subcarriers consist of data  $\mathbf{d}_k$  and pilot symbols  $\mathbf{p}_k$ , with  $\mathbf{D}_k$  and  $\mathbf{P}_k$  being permutation matrices that assign each pilot and data symbol to its corresponding frequency subcarrier. Note that  $\mathbf{x}_k = [\mathbf{x}_{k,1}^T, \dots, \mathbf{x}_{k,M_T}^T]^T$  and  $\mathbf{y}_k = [\mathbf{y}_{k,1}^T, \dots, \mathbf{y}_{k,M_R}^T]^T$  stack the transmit and receive subcarriers for all antennas, with  $\mathbf{p}_k = [\mathbf{p}_{k,1}^T, \dots, \mathbf{p}_{k,M_T}^T]^T$  and  $\mathbf{d}_k = [\mathbf{d}_{k,1}^T, \dots, \mathbf{d}_{k,M_T}^T]^T$  the vectors containing the pilot and data symbols for all transmit antennas, and  $\mathbf{P}_k = \text{diag}\{\mathbf{P}_{k,1}, \dots, \mathbf{P}_{k,M_T}\}$  and  $\mathbf{D}_k = \text{diag}\{\mathbf{D}_{k,1}, \dots, \mathbf{D}_{k,M_T}\}$  are block-diagonal matrices with the subcarrier allocations for pilots and data for each transmit antenna.

### 5.3 ICI Estimation

In this work, an strategy based on estimating the ICI from the variations over time of the channel coefficients for each subcarrier will be used. Figure 5.1 shows a summary of this scheme, where the antenna subindices are not indicated for the sake of simplicity. First, frequency response estimations  $\hat{\mathbf{g}}_k$  from a set of  $K$  consecutive OFDM symbols are obtained, where  $\bar{\mathbf{g}}_k = \text{diag}\{\overline{\mathbf{G}}_k\}$ . The ICI estimation algorithm takes these values as the input, and then it

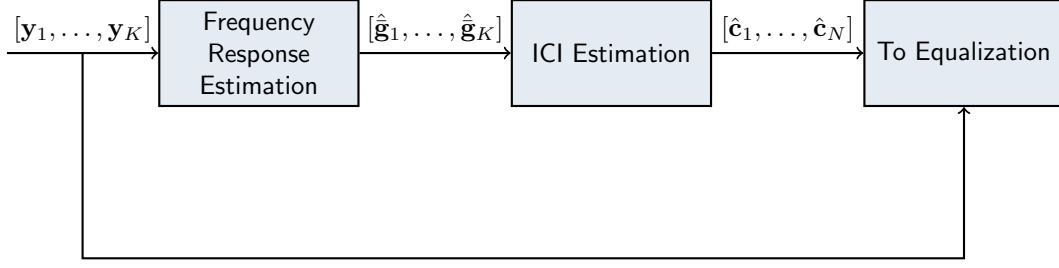


Figure 5.1: General scheme of the ICI estimation strategy. From the received OFDM symbols an initial frequency response estimations are obtained, which are eventually used to obtain the ICI per subcarrier from the variations in the time direction.

completes its task by obtaining the set of  $Q$  coefficients for each of the  $N$  subcarriers of the symbol. Finally, these estimations together with the input are used by the equalizer to recover the transmitted signal.

The first stage is a conventional frequency response estimation algorithm corresponding to each symbol inside the group of  $K$  OFDM symbols. For example, the LMMSE estimator, when a set of pilot subcarriers are allocated, can be expressed as [51]

$$\hat{\mathbf{g}}_{\text{LS},k,i,j}^{(p)} = \mathbf{Q}_{k,j}^{-1} \mathbf{y}_{k,i,j}^{(p)}, \quad (5.6)$$

$$\hat{\mathbf{g}}_{\text{LMMSE},k,i,j} = \mathbf{R}_{gg_p} (\mathbf{R}_{g_p g_p} + (\sigma_w/E_p)^2)^{-1} \hat{\mathbf{g}}_{\text{LS},k,i,j}^{(p)}, \quad (5.7)$$

where  $\mathbf{y}_{k,i,j}^{(p)} = \mathbf{P}_{k,j}^T \mathbf{y}_{k,i}$  represents the  $P \times 1$  vector of received pilot symbols transmitted from the  $j$ -th antenna and received by the  $i$ -th antenna for the  $k$ -th OFDM symbol,  $\mathbf{Q}_{k,j} = \text{diag}\{\mathbf{p}_{k,j}\}$  is a  $P \times P$  matrix with the transmitted pilot symbols on its main diagonal,  $\hat{\mathbf{g}}_{\text{LS},k,i,j}^{(p)}$  is a  $P \times 1$  vector with the Least Squares (LS) estimation of the channel coefficients at the pilot subcarriers,  $\mathbf{R}_{gg_p}$  is the  $N \times P$  cross-correlation matrix of the channel coefficients with the pilot positions,  $\mathbf{R}_{g_p g_p}$  is the  $P \times P$  autocorrelation matrix of the frequency response in the pilot positions,  $E_p$  is the energy of the pilot subcarriers, and  $\sigma_w^2$  is the noise variance. In a time-selective fading channel, the noise caused by ICI can be considered as part of the channel noise variance  $\sigma_w^2$ . The coefficients of  $\hat{\mathbf{g}}_{\text{LMMSE},k,i,j}$  will correspond to the elements of the main diagonal of  $\overline{\mathbf{G}}_{k,i,j}$ , so an estimation of the time-averaged frequency response of the channel during the symbol for each subcarrier will be obtained.

The MSE of this estimator is [51]

$$\text{MSE}_k = \frac{1}{N} \text{tr}(\mathbf{R}_{gg} - \mathbf{R}_{gg_p} (\mathbf{R}_{g_p g_p} + (\sigma_w/E_p)^2)^{-1} \mathbf{R}_{g_p g}). \quad (5.8)$$

Let us now define  $\mathbf{g}_n$  as the vector containing the frequency response of the  $n$ -th subcarrier during  $K$  consecutive OFDM symbols with  $N$  samples each, after removing the cyclic prefix, in a transmission between the  $j$ -th transmit and  $i$ -th receive antennas. We will drop these indices

from now on in this section to simplify the notation:

$$\mathbf{g}_n = [\mathbf{h}_1, \mathbf{h}_2, \dots, \mathbf{h}_L] \mathbf{f}_n, \quad (5.9)$$

where the  $\mathbf{h}_l = [h[G, l], \dots, h[N_T - 1, l], h[N_T + G, l], \dots, h[KN_T - 1, l]]^T$  are  $KN \times 1$  vectors which stack the channel impulse response for the  $l$ -th path,  $\mathbf{f}_n$  is the  $L \times 1$  vector with the first  $L$  rows of the  $n$ -th column of the matrix  $\mathbf{F}$ .

Using a  $Q$ -dimensional BEM,  $\mathbf{g}_n$  can be approximated as follows

$$\mathbf{g}_n = \mathbf{B} \mathbf{c}_n, \quad (5.10)$$

where  $\mathbf{B} = [\mathbf{b}_1^T, \mathbf{b}_1^T, \dots, \mathbf{b}_Q^T]$  is an  $KN \times Q$  matrix with the basis vectors that define the BEM, and  $\mathbf{c}_n$  is a  $Q \times 1$  vector of BEM coefficients for the  $n$ -th subcarrier. To obtain the channel evolution during the  $k$ -th OFDM symbol, matrix  $\mathbf{B}$  can be split in  $K$  different matrices  $\mathbf{B}_k$  with dimensions  $N \times Q$ , hence defining a BEM matrix for each symbol inside the group of  $K$  symbols as  $\mathbf{B}_k = [\mathbf{b}_{(k-1)N+1}, \mathbf{b}_{(k-1)N+2}, \dots, \mathbf{b}_{kN}]^T$ , where the  $\mathbf{b}_i$  vectors represent the  $i$ -th column of  $\mathbf{B}^T$ .

In a SISO-OFDM system, the ICI can be estimated from the channel estimates obtained in the frequency domain using the following expression of the channel matrix  $\mathbf{G}_k$  in terms of a BEM for the  $k$ -th OFDM symbol [79]

$$\mathbf{G}_k = \sum_{q=1}^Q \mathbf{D}_{k,q} \text{diag} \{ \mathbf{d}_q \}, \quad (5.11)$$

with

$$\mathbf{D}_{k,q} = \mathbf{F} \text{diag} \{ \mathbf{b}_{k,q} \} \mathbf{F}^H, \quad (5.12)$$

where  $\mathbf{b}_{k,q}$  represents the  $q$ -th column of the matrix  $\mathbf{B}_k$ , and  $\mathbf{d}_q = [[\mathbf{c}_1]_q, [\mathbf{c}_2]_q, \dots, [\mathbf{c}_N]_q]$ . Note that, in this estimation scheme, the vectors  $\mathbf{c}_n$  contain the values to be estimated instead of the original  $\mathbf{g}_n$ . In the ensuing subsection, a low-rank approximation of the LMMSE estimation of  $\mathbf{g}_n$  will be used to obtain the BEM coefficients  $\mathbf{c}_n$ .

### 5.3.1 Optimal BEM Design

In this work, the  $\mathbf{g}_n$  vectors are obtained from the evolution over time of the frequency response coefficients per subcarrier, as shown in Figure 5.2. Once an estimation of the frequency response of the channel for a group of consecutive OFDM symbols is available, the correlation properties in the time domain can be exploited to reconstruct the evolution of the channel over time at each subcarrier frequency. The frequency response estimations only produce a single channel coefficient per subcarrier for the duration of an OFDM symbol, which lasts for  $NT_s$  seconds in the time-domain, while the actual channel could have changed during that  $NT_s$  time interval.

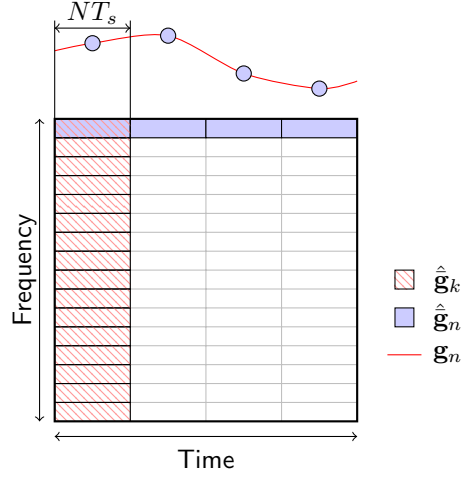


Figure 5.2: Overview of the ICI estimation scheme for  $K = 4$  consecutive OFDM symbols.  $\hat{\mathbf{g}}_k$  is the frequency response estimation for the  $k$ -th OFDM symbol. The estimates per subcarrier in the time direction  $\hat{\mathbf{g}}_n$  are used to recover the evolution of the channel frequency response over time  $\mathbf{g}_n$  for the  $n$ -th subcarrier.

Using a set of consecutive OFDM symbols allows for reconstructing the original channel although only a single sample is available from each OFDM symbol period and subcarrier.

Let us define  $\bar{\mathbf{g}}_n = [[\bar{\mathbf{G}}_1]_{n,n}, [\bar{\mathbf{G}}_2]_{n,n}, \dots, [\bar{\mathbf{G}}_K]_{n,n}]^T$  as a  $K \times 1$  vector with the time-averaged (over a single OFDM symbol) channel coefficients for the  $n$ -th subcarrier of  $K$  OFDM symbols, and whose elements are  $[\bar{\mathbf{g}}_n]_k = \frac{1}{N} \sum_{i=0}^{N-1} [\mathbf{g}_n]_{kN+i}$ . An estimate of  $\bar{\mathbf{g}}_n$  can be obtained from a frequency response estimation step, as defined in the previous section, which can be decomposed in

$$\hat{\mathbf{g}}_n = \bar{\mathbf{g}}_n + \mathbf{e}_n, \quad (5.13)$$

where  $\hat{\mathbf{g}}_n$  is a  $K \times 1$  vector which contains the estimated values for  $\bar{\mathbf{g}}_n$ ,  $\mathbf{e}_n$  is a  $K \times 1$  vector of error components from the estimation method used in the frequency response estimation step with a variance  $\sigma_{\text{MSE}}^2$ . It will be assumed that the estimation error  $\mathbf{e}_n$  and the channel coefficients  $\bar{\mathbf{g}}_n$  are uncorrelated, and also the estimation error between different symbols for a given subcarrier.

Let us also define a  $KN \times K$  matrix  $\mathbf{W}$  to obtain the LMMSE estimation of  $\mathbf{g}_n$  from the estimated channel frequency response with the form

$$\hat{\mathbf{g}}_{\text{LMMSE},n} = \mathbf{W} \hat{\mathbf{g}}_n = \mathbf{W}(\bar{\mathbf{g}}_n + \mathbf{e}_n), \quad (5.14)$$

with matrix  $\mathbf{W}$  defined as follows

$$\mathbf{W} = \mathbf{C}_{g\bar{g}}(\mathbf{C}_{\bar{g}\bar{g}} + \sigma_{\text{MSE}}^2 \mathbf{I})^{-1} \quad (5.15)$$

where  $\mathbf{C}_{g\bar{g}}$  is the  $KN \times K$  cross-correlation matrix of the channel coefficients with the average of the channel coefficients during an OFDM symbol, and  $\mathbf{C}_{\bar{g}\bar{g}}$  is the  $K \times K$  autocorrelation

matrix of the average of the channel coefficients. These matrices can be readily computed from the elements of  $\mathbf{C}_{gg}$ , with  $\mathbf{C}_{gg} = \mathbb{E}\{\mathbf{g}_n \mathbf{g}_n^H\}$  and assuming that this correlation in the time direction is indifferent of the subcarrier index, hence

$$\begin{aligned}
 [\mathbf{C}_{g\bar{g}}]_{i,j} &= [\mathbb{E}\{\mathbf{g}_n \bar{\mathbf{g}}_n^H\}]_{i,j} = \mathbb{E}\{[\mathbf{g}_n]_i [\bar{\mathbf{g}}_n]_j^*\} \\
 &= \mathbb{E}\left\{[\mathbf{g}_n]_i \frac{1}{N} \sum_{k=0}^{N-1} [\mathbf{g}_n]_{jN+k}^*\right\} \\
 &= \frac{1}{N} \sum_{k=0}^{N-1} \mathbb{E}\{[\mathbf{g}_n]_i [\mathbf{g}_n]_{jN+k}^*\} \\
 &= \frac{1}{N} \sum_{k=0}^{N-1} [\mathbf{C}_{gg}]_{i,jN+k},
 \end{aligned} \tag{5.16}$$

and

$$\begin{aligned}
 [\mathbf{C}_{\bar{g}\bar{g}}]_{i,j} &= [\mathbb{E}\{\bar{\mathbf{g}}_n \bar{\mathbf{g}}_n^H\}]_{i,j} = \mathbb{E}\{[\bar{\mathbf{g}}_n]_i [\bar{\mathbf{g}}_n]_j^*\} \\
 &= \mathbb{E}\left\{\frac{1}{N} \sum_{k=0}^{N-1} [\mathbf{g}_n]_{iN+k} \frac{1}{N} \sum_{l=0}^{N-1} [\mathbf{g}_n]_{jN+l}^*\right\} \\
 &= \frac{1}{N^2} \sum_{k=0}^{N-1} \sum_{l=0}^{N-1} \mathbb{E}\{[\mathbf{g}_n]_{iN+k} [\mathbf{g}_n]_{jN+l}^*\} \\
 &= \frac{1}{N^2} \sum_{k=0}^{N-1} \sum_{l=0}^{N-1} [\mathbf{C}_{gg}]_{iN+k,jN+l}.
 \end{aligned} \tag{5.17}$$

The following SVD decompositions can be applied

$$\mathbf{C}_{g\bar{g}} = \mathbf{U}_1 \mathbf{S}_1 \mathbf{V}_1^H \tag{5.18}$$

$$\mathbf{C}_{\bar{g}\bar{g}} = \mathbf{U}_2 \mathbf{S}_2 \mathbf{V}_2^H \tag{5.19}$$

where  $\mathbf{U}_1$ ,  $\mathbf{V}_1$ ,  $\mathbf{U}_2$  and  $\mathbf{V}_2$  are unitary matrices, and  $\mathbf{S}_1$  and  $\mathbf{S}_2$  are matrices with the singular values arranged in decreasing order on their main diagonal. Substituting in (5.14) we obtain

$$\hat{\mathbf{g}}_{\text{LMMSE},n} = \mathbf{U}_1 \mathbf{S}_1 \mathbf{V}_1^H \mathbf{V}_2 \mathbf{\Lambda} \mathbf{U}_2^H \hat{\mathbf{g}}_n, \tag{5.20}$$

where  $\mathbf{\Lambda} = \text{diag}\{[\sigma_1 + \sigma_{\text{MSE}}^2, \sigma_2 + \sigma_{\text{MSE}}^2, \dots, \sigma_K + \sigma_{\text{MSE}}^2]\}^{-1}$  and the  $\sigma_k$  elements are the singular values of  $\mathbf{C}_{\bar{g}\bar{g}}$ . A rank-reduced version of this estimator can be obtained by considering only the first  $Q$  coefficients in the main diagonal of  $\mathbf{S}_1$ , and assigning to zero the remaining elements.

This expression can be interpreted as a BEM (see (5.10)) with  $\mathbf{B} = \mathbf{U}_1$  and  $\mathbf{c}_n = \mathbf{S}_1 \mathbf{V}_1^H \mathbf{V}_2 \mathbf{\Lambda} \mathbf{U}_2^H \hat{\mathbf{g}}_n$ .

The MSE of this estimator for the  $n$ -th subcarrier is

$$\begin{aligned}
 \text{MSE}_n &= \frac{1}{KN} \mathbb{E}\{(\mathbf{g}_n - \hat{\mathbf{g}}_{\text{LMMSE},n})(\mathbf{g}_n - \hat{\mathbf{g}}_{\text{LMMSE},n})^H\} \\
 &= \frac{1}{KN} \text{tr}(\mathbf{C}_{gg} - 2\Re(\mathbf{W}\mathbf{C}_{g\bar{g}}) + \mathbf{W}\mathbf{C}_{\bar{g}\bar{g}}\mathbf{W}^H).
 \end{aligned} \tag{5.21}$$

### 5.3.2 Optimal BEM Design under Spatially Correlated Channels

If spatial correlation is present between transmit and/or receive antennas, the previous estimation model can be extended to include this information. Starting from a similar model as in the previous section, but extending it to the MIMO case

$$\hat{\mathbf{g}}_{\text{LMMSE},n}^{M_T \times M_R} = \mathbf{W} \hat{\mathbf{g}}_n^{M_T \times M_R} = \mathbf{W} (\bar{\mathbf{g}}_n^{M_T \times M_R} + \mathbf{e}_n), \quad (5.22)$$

where  $\hat{\mathbf{g}}_n^{M_T \times M_R} = [\hat{\mathbf{g}}_{n,1,1}^T, \dots, \hat{\mathbf{g}}_{n,1,M_T}^T, \dots, \hat{\mathbf{g}}_{n,M_R,M_T}^T]^T$  is a  $K M_T M_R \times 1$  vector with the complex coefficient for the  $n$ -th subcarrier during  $K$  OFDM symbols for all  $M_R M_T$  paths, with  $\bar{\mathbf{g}}_{n,i,j} = [\bar{\mathbf{G}}_{1,i,j}(n, n), \bar{\mathbf{G}}_{2,i,j}(n, n), \dots, \bar{\mathbf{G}}_{K,i,j}(n, n)]$ ,  $\mathbf{W}$  is a  $K N M_T M_R \times K M_T M_R$  matrix, and  $\mathbf{e}$  is a  $K M_T M_R \times 1$  vector of white Gaussian noise variables, with variance  $\sigma_{\text{MSE}}^2$  equal to the MSE of the frequency response estimation method used in the previous step. If  $\mathbf{W}$  corresponds to an LMMSE estimator, this matrix takes the form

$$\mathbf{W} = \mathbf{C}_{g\bar{g}}^{M_T \times M_R} (\mathbf{C}_{g\bar{g}}^{M_T \times M_R} + \sigma_{\text{MSE}}^2 \mathbf{I}_{K M_T M_R})^{-1}, \quad (5.23)$$

where  $\mathbf{C}_{g\bar{g}}^{M_T \times M_R}$  is the  $K N M_T M_R \times K M_T M_R$  cross-correlation matrix of the channel coefficients with the average of the channel coefficients during an OFDM symbol, and  $\mathbf{C}_{g\bar{g}}^{M_T \times M_R}$  is the  $K M_T M_R \times K M_T M_R$  autocorrelation matrix of the average of the channel coefficients. These matrices can be readily computed from the elements of  $\mathbf{C}_{g\bar{g}}^{M_T \times M_R} = \mathbb{E} \left\{ \mathbf{g}_n^{M_T \times M_R} \mathbf{g}_n^{M_T \times M_R H} \right\} = \mathbf{R} \otimes \mathbf{C}_{gg}$  for the MIMO case, where  $\mathbf{R}$  is the  $M_R \times M_T$  spatial correlation matrix, as

$$[\mathbf{C}_{g\bar{g}}^{M_T \times M_R}]_{i,j} = [\mathbf{R}]_{[i/(KN)], [j/K]} \left( \frac{1}{N} \sum_{k=0}^{N-1} [\mathbf{C}_{gg}]_{\text{mod}(i,KN), \text{mod}(j,K)N+k} \right), \quad (5.24)$$

and

$$[\mathbf{C}_{g\bar{g}}^{M_T \times M_R}]_{i,j} = [\mathbf{R}]_{[i/K], [j/K]} \left( \frac{1}{N^2} \sum_{k=0}^{N-1} \sum_{l=0}^{N-1} [\mathbf{C}_{gg}]_{\text{mod}(i,K)N+k, \text{mod}(j,K)N+l} \right). \quad (5.25)$$

Next, let us apply an SVD decomposition and write the correlation matrices in the form

$$\begin{aligned} \mathbf{C}_{g\bar{g}}^{M_T \times M_R} &= \mathbf{U}_{g\bar{g}} \mathbf{S}_{g\bar{g}} \mathbf{V}_{g\bar{g}}^H, \\ \mathbf{C}_{g\bar{g}}^{M_T \times M_R} &= \mathbf{U}_{g\bar{g}} \mathbf{S}_{g\bar{g}} \mathbf{V}_{g\bar{g}}^H. \end{aligned} \quad (5.26)$$

Alternatively, this decomposition can be written as

$$\mathbf{C}_{g\bar{g}}^{M_T \times M_R} = (\mathbf{U}_s \otimes \mathbf{U}_1) (\mathbf{S}_s \otimes \mathbf{S}_1) (\mathbf{V}_s^H \otimes \mathbf{V}_1^H), \quad (5.27)$$

$$\mathbf{C}_{g\bar{g}}^{M_T \times M_R} = (\mathbf{U}_s \otimes \mathbf{U}_2) (\mathbf{S}_s \otimes \mathbf{S}_2) (\mathbf{V}_s^H \otimes \mathbf{V}_2^H), \quad (5.28)$$

where  $\mathbf{U}_1 \mathbf{S}_1 \mathbf{V}_1^H$  and  $\mathbf{U}_2 \mathbf{S}_2 \mathbf{V}_2^H$  are the SVD decompositions of the expression in parentheses in Eq. (5.24) and Eq. (5.25), respectively;  $\mathbf{U}_s \mathbf{S}_s \mathbf{V}_s^H$  is the SVD decomposition of  $\mathbf{R}$ ;  $\mathbf{U}_1, \mathbf{V}_1, \mathbf{U}_s,$

$\mathbf{V}_s$ ,  $\mathbf{U}_2$  and  $\mathbf{V}_2$  are unitary matrices; and  $\mathbf{S}_1$ ,  $\mathbf{S}_s$ , and  $\mathbf{S}_2$  are matrices with their singular values arranged in decreasing order on the main diagonal. If the singular values of  $(\mathbf{S}_s \otimes \mathbf{S}_1)$  and  $(\mathbf{S}_s \otimes \mathbf{S}_2)$  are reordered on the main diagonals, the columns and rows of the matrices containing the singular vectors will have to be reordered accordingly.

Replacing these expressions in (5.23), we obtain

$$\hat{\mathbf{g}}_{\text{LMMSE},n}^{M_T \times M_R} = \mathbf{U}_{g\bar{g}} \mathbf{S}_{g\bar{g}} \mathbf{V}_{g\bar{g}}^H \mathbf{U}_{g\bar{g}} (\mathbf{S}_{g\bar{g}} + \sigma_{\text{MSE}}^2 \mathbf{I}_{KM_T M_R})^{-1} \mathbf{V}_{g\bar{g}}^H \hat{\mathbf{g}}_n^{M_T \times M_R}. \quad (5.29)$$

Again, a rank-reduced version of this estimator can be obtained by considering only the  $Q$  higher elements on the main diagonal of  $\mathbf{S}_{g\bar{g}}$ , and setting to zero the remaining values. This expression can be interpreted as a BEM (see Eq. (5.10)) where  $\mathbf{B} = \mathbf{U}_{g\bar{g}}$  and  $\mathbf{c}_n = \mathbf{S}_{g\bar{g}} \mathbf{V}_{g\bar{g}}^H \mathbf{U}_{g\bar{g}} (\mathbf{S}_{g\bar{g}} + \sigma_{\text{MSE}}^2 \mathbf{I}_{KM_T M_R})^{-1} \mathbf{V}_{g\bar{g}}^H \hat{\mathbf{g}}_n$ .

It is important to note that in this estimation method it is not necessary to make an assumption on the samples chosen from the original matrix  $\mathbf{B}$  to make the projection, hence avoiding the definition of an arbitrary time index [37, 79]. Also, the information about the average of the coefficients is taken into account when the BEM is defined which reflects more accurately the behavior of the channel. The order of this BEM is related to the joint spatial and temporal correlations, so the values of  $Q$  will be larger compared with systems where only the temporal correlation is considered.

### 5.3.3 Channel BEM Coefficients Estimation

Let us assume we have estimations of the main diagonal of  $\overline{\mathbf{G}}_k$  for a set of  $K$  OFDM symbols and define the  $N \times 1$  column vectors  $\hat{\mathbf{g}}_k = \text{diag} \{ \overline{\mathbf{G}}_k \}^T$ . No specific method is assumed to compute such estimates. In this sense, if an LS or LMMSE estimator is used, ICI corresponding to pilot and data subcarriers will interfere in the estimation.

The LS estimator of the coefficients can be written as [79]:

$$[\hat{\mathbf{c}}_1, \hat{\mathbf{c}}_2, \dots, \hat{\mathbf{c}}_N] = (\mathbf{M}^H \mathbf{M})^{-1} \mathbf{M}^H [\hat{\mathbf{g}}_1, \hat{\mathbf{g}}_2, \dots, \hat{\mathbf{g}}_K]^T, \quad (5.30)$$

where  $\mathbf{M} = [\mathbf{m}_1, \dots, \mathbf{m}_Q]$  is a matrix composed by the basis vectors sampled at the OFDM symbol period, with  $\mathbf{m}_q = [[\mathbf{b}_q]_{G+N/2}, [\mathbf{b}_q]_{N/2+N}, \dots, [\mathbf{b}_q]_{N/2+(K-1)N}]^T$  a  $K \times 1$  vector obtained by selecting  $K$  samples from the  $q$ -th basis vector  $\mathbf{b}_q$ , and with  $\hat{\mathbf{c}}_n$  the  $Q \times 1$  vectors containing the estimated ICI coefficients. This method is equivalent to a LS fitting of the coefficients according to the vectors of the BEM. It is important to note that the LS method defined in (5.30) depends on the sampling of the basis vectors of the BEM in some arbitrarily chosen indices, in this case those corresponding to the middle of each OFDM symbol. This approach considers that the frequency response coefficients in  $\hat{\mathbf{g}}_k$  come from the channel response in the middle of the OFDM symbol, and not from the averaged channel response during the symbol.

With the result obtained in the previous section, and under the assumption that the coefficients in all subcarriers have the same Doppler Power Spectral Density (PSD) we can define a low-rank approximation of the LMMSE channel estimator, and the coefficients to compute the ICI component per antenna pair are obtained as follows

$$[\hat{\mathbf{c}}_1, \hat{\mathbf{c}}_2, \dots, \hat{\mathbf{c}}_N] = \mathbf{S}_1 \mathbf{V}_1^H \mathbf{V}_2 \mathbf{\Lambda} \mathbf{U}_2^H [\hat{\mathbf{g}}_1, \hat{\mathbf{g}}_2, \dots, \hat{\mathbf{g}}_K]^T, \quad (5.31)$$

and extended to the spatially correlated MIMO case as

$$[\hat{\mathbf{c}}_1, \hat{\mathbf{c}}_2, \dots, \hat{\mathbf{c}}_N] = \mathbf{S}_{g\bar{g}} \mathbf{V}_{g\bar{g}}^H \mathbf{U}_{g\bar{g}} (\mathbf{S}_{g\bar{g}} + \sigma_{\text{MSE}}^2 \mathbf{I}_{K M_T M_R})^{-1} \mathbf{V}_{g\bar{g}}^H [\hat{\mathbf{g}}_1^{M_T \times M_R}, \dots, \hat{\mathbf{g}}_K^{M_T \times M_R}]^T, \quad (5.32)$$

which reduces to (5.31) when  $\mathbf{R} = \mathbf{I}_{M_T M_R}$ . Also, under the spatially correlated setup, the  $\hat{\mathbf{c}}_n$  vectors have dimensions  $Q M_T M_R \times 1$ , and contain the  $Q$  coefficients for all the  $M_T \times M_R$  antenna pairs, and the corresponding subvector for each pair must be selected to obtain its ICI.

Finally, once the estimates of  $\mathbf{c}_q$  are calculated, they can be plugged in (5.11) and  $\hat{\mathbf{G}}_k$  can be computed. To build the full  $\hat{\mathbf{G}}_k$  matrix for a MIMO case, as defined in (5.2), the algorithm described in this section is repeated for each pair of transmit and receive antennas. Summarizing, the steps to obtain the ICI estimates are the following:

1. Frequency response estimations  $\hat{\mathbf{g}}_k$  are obtained from the arriving signal vectors  $\mathbf{y}_k$ .
2. Once a group of frequency response estimations for  $K$  consecutive OFDM symbols are available, they are used in (5.31) to obtain the  $\hat{\mathbf{c}}_n$  for each subcarrier.
3. The  $\hat{\mathbf{c}}_n$  are used to construct the vectors  $\mathbf{d}_q$  which are plugged in (5.11) to obtain the ICI affecting the  $K$  OFDM symbols considered. A different matrix  $\mathbf{D}_{k,g}$  will be used for each OFDM symbol inside the group.

### 5.3.4 Computational Complexity

In this section, an analysis of the computational complexity of the ICI estimation algorithms described previously is provided, without considering the cost of signal equalization, which depends on the particular algorithm chosen.

The computation of the  $\hat{\mathbf{c}}_n$  vectors, assuming that the estimation matrix is known, has a computational complexity  $\mathcal{O}(N K M_T M_R Q)$ . Computing the  $\hat{\mathbf{G}}_k$  matrix has a computational complexity of  $\mathcal{O}(N^2 M_T M_R Q)$ . This complexity can be lowered if only some off-diagonal elements are assumed to be different than zero. If the number of considered diagonals different from the main diagonal is denoted as  $N_{\text{off}}$ , the complexity has the form  $\mathcal{O}(N N_{\text{off}} M_T M_R Q)$ . The order  $Q$  as defined in previous sections is larger in the spatially correlated setup, but if we examine the structure of the matrix  $\mathbf{U}_{g\bar{g}}$  as a result of a Kronecker product (see (5.27)), it can be observed that some of the coefficients of  $\mathbf{c}_n$  could operate with scaled versions of the same

column of  $\mathbf{U}_1$  depending on the antenna-pair considered, turning out to be possible to further reduce the computation of  $\tilde{\mathbf{G}}_k$ .

It must be highlighted that the estimation of the correlation matrices, the noise variance and the ICI are not considered in this analysis, as well as the SVD decomposition to build the BEM. These steps would increase the overall computational complexity of the estimator.

## 5.4 Results

Computer simulations were carried out to illustrate the performance of the time-varying MIMO-OFDM channel estimation method described in previous sections. We considered a MIMO-OFDM system with  $N = 128$  subcarriers and baseband bandwidth  $F_s = 1$  MHz. The cyclic prefix length was set to 1/8 of the number of subcarriers, i.e.,  $N_g = 16$ . The pilot structure is specified by the WiMAX standard for MIMO  $2 \times 2$  and  $4 \times 4$  transmissions in the open-loop mode [44]. The carrier frequency is  $f_c = 5.2$  GHz and the maximum Doppler spread is  $f_d = v f_c / c$ , being  $v$  the relative velocity between transmitter and receiver.

Regarding Doppler spectrum, the Jakes model assumes that the angles of arrival of paths are uniformly distributed in the interval  $[-\pi, \pi]$  in the azimuth plane of the receiving antennas. The autocorrelation function of this model is given by [47, 63]

$$r(\tau) = J_0(2\pi f_d \tau), \quad (5.33)$$

where  $J_0(\cdot)$  is the zeroth-order Bessel function. When the angles of arrival are constrained to arrive from a narrower interval, an asymmetrical Jakes spectrum model arises, and its autocorrelation function is [27]

$$r(\tau) = \int_{\sin^{-1}(f_{\min})}^{\sin^{-1}(f_{\max})} \cos(2\pi f_d \tau \sin \phi) d\phi \quad (5.34)$$

$$-j \int_{\cos^{-1}(f_{\min})}^{\cos^{-1}(f_{\max})} \sin(2\pi f_d \tau \cos \phi) d\phi, \quad (5.35)$$

where  $f_{\min} = f_{d,\min}/f_d$  and  $f_{\max} = f_{d,\max}/f_d$  are the normalized minimum and maximum Doppler frequencies, respectively. In our simulations an asymmetrical Jakes spectrum model will be considered. These autocorrelation functions depend on the normalized Doppler spread  $f_d T$ ,  $T = NT_s$  the duration in seconds of a single OFDM symbol, which is related to the relative speed between the transmitter and the receiver.

The Doppler spectrum follows an asymmetrical Jakes model with  $f_{\min} = 0.4$  and  $f_{\max} = 1.0$ . It is also interesting to note how this estimation algorithm is affected by the number of transmit antennas, regardless of the considered BEM. Since this algorithm takes as input the channel frequency response of individual OFDM symbols, and we have considered a pilot-aided MMSE estimation, these starting estimations will be affected by ICI generated by the

unknown data subcarriers from all the transmit antennas. In our implementation, the power of the ICI is assumed to be part of the noise vector for this initial frequency response estimation, deriving it from the time correlation of the channel [54].

### 5.4.1 Estimation under Spatially Uncorrelated Channels

In these simulations, the results obtained with the proposed estimation method defined in (5.31) (denoted as “Proposed KL-BEM” in the result figures) are compared to those obtained with DPS-BEM [96] and KL-BEM [89] using the method based on the LS estimation of the ICI with order  $Q = 3$  given by (5.30). The ICI estimation algorithm is applied to groups of  $K = 6$  MIMO-OFDM symbols, starting from the LMMSE estimation of the frequency response of the channel for each symbol. In order to compute Bit Error Ratio (BER) estimations, an approximation of the LS ICI cancellation algorithm is applied [48] and properly adapted to the MIMO-OFDM case. Up to  $N_{\text{off}} = 4$  diagonals at each side of the main diagonal of the channel frequency response matrix were considered.

Table 5.1 shows the power delay profile of the channel impulse responses considered in the simulations. The same power delay profile was used for the  $M_T M_R$  channels between each transmit-receive antenna pair. We considered spatially uncorrelated MIMO channels in which the impulse responses of the different channel pairs between all transmit and receive antennas are uncorrelated.

Figure 5.3 plots the resulting channel estimation MSE for a given SNR = 30 dB and different Doppler spreads for  $2 \times 2$  and  $4 \times 4$  MIMO-OFDM systems. The MSE is measured at the receiver, comparing the estimated coefficients with the channel generated during the simulations. All diagonals of the matrices are considered to compute the MSE. It can be seen that the proposed ICI estimation method with a modified KL-BEM outperforms those based on previous estimation algorithms, hence obtaining a constant gain independent from the Doppler spread.

Figure 5.4 plots the resulting channel estimation MSE for a given normalized Doppler spread  $f_d T = 0.20$  and different SNR levels. Notice how the proposed KL-BEM method outperforms DPS-BEM and classical KL-BEM.

Figure 5.5 plots the uncoded BER for the MIMO-OFDM receiver, a given Doppler spread value  $f_d T = 0.20$ , and different SNR levels. The curve denoted as “Ideal” was obtained by equalizing the received signal assuming all the channel coefficients are known. It can also be observed that larger estimation errors shown in previous plots translate into higher BER values in scenarios with more transmit antennas.

Tap	Power [dB]	Delay [ns]
1	0	0
2	-1	100
3	-9	300
4	-10	500

Table 5.1: Power delay profile of the channel model considered for the computer simulations under spatially uncorrelated channels.

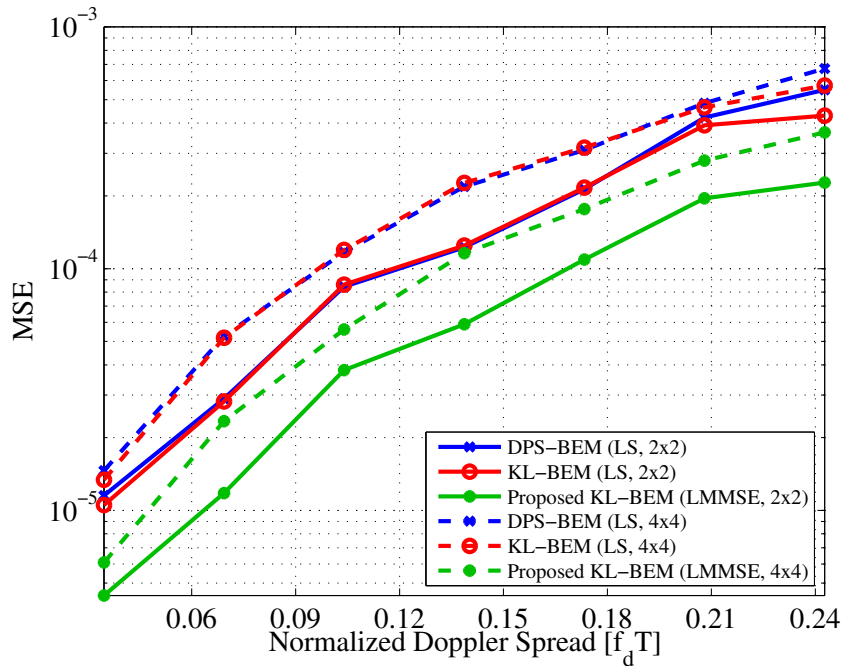


Figure 5.3: MSE of the channel matrix estimation over normalized Doppler spread for SNR = 30 dB and under spatially uncorrelated channels.

Tap	Power [dB]	Delay [ns]
1	0	0
2	-1	100
3	-9	300
4	-10	500
5	-15	800
6	-20	1200

Table 5.2: Power delay profile of the channel model considered for the computer simulations under spatially correlated channels.

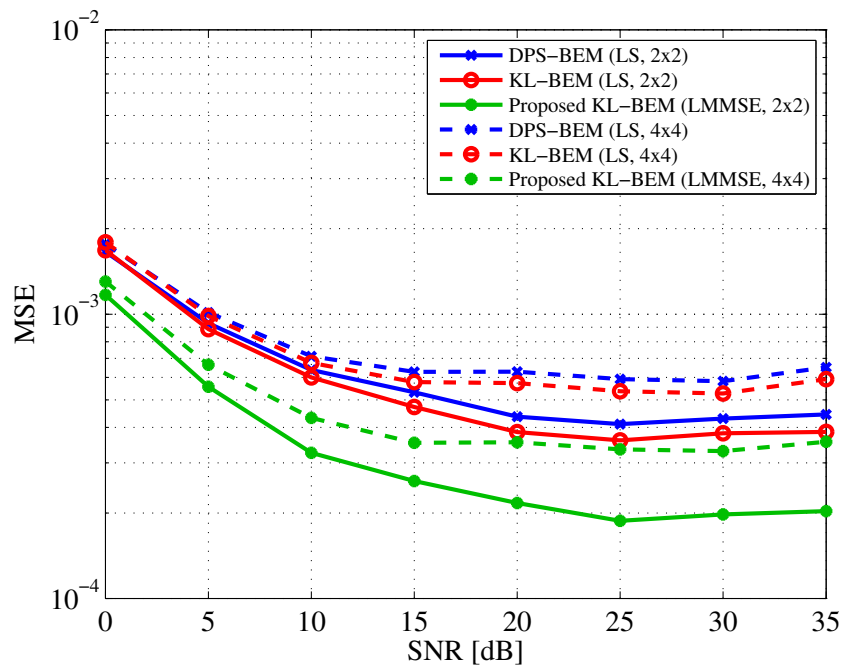


Figure 5.4: MSE of the channel matrix estimation over SNR for a normalized Doppler spread value  $f_d T = 0.20$  and under spatially uncorrelated channels.

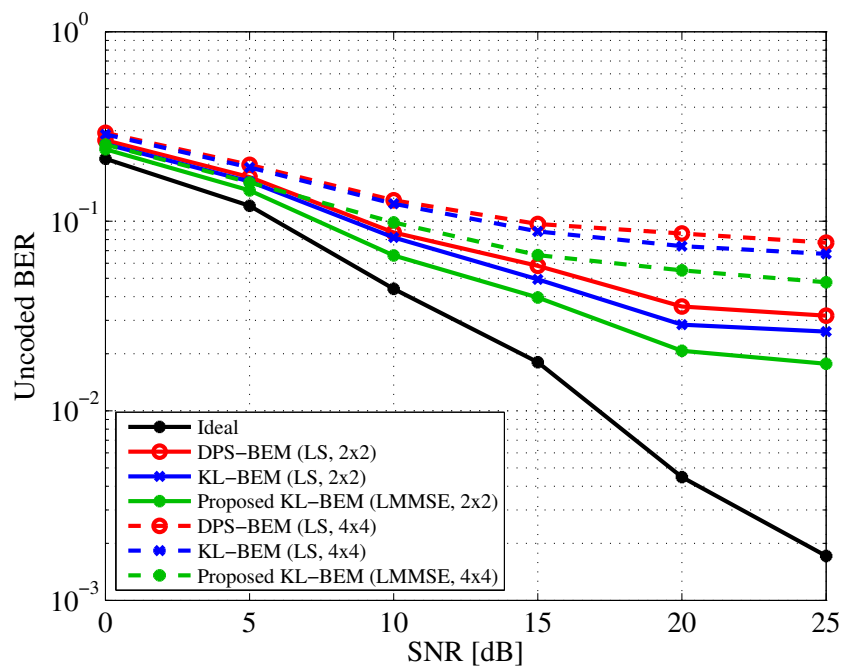


Figure 5.5: BER over SNR for  $2 \times 2$  and  $4 \times 4$  MIMO transmissions for normalized Doppler spread value  $f_d T = 0.20$  and under spatially uncorrelated channels.

### 5.4.2 Estimation under Spatially Correlated Channels

In our simulations, the results obtained with the proposed estimation method are compared to those obtained with DPS-BEM using the method based on the LS estimation of the ICI with orders  $Q^{M_T \times M_R} = 16$  and  $Q^{M_T \times M_R} = 32$ . Since  $Q$  is related with the joint spatial and temporal representation of the channel, in the case of the estimators which ignore spatial correlation, it is equivalent to use a BEM with order  $Q = 1$  and  $Q = 2$ , respectively, for each TX-RX antenna pair in this  $4 \times 4$  setup. The ICI estimation algorithm is applied to groups of  $K = 6$  MIMO-OFDM symbols, starting from the MMSE estimation of the frequency response of the channel for each symbol. In this initial estimate, the noise variance and the power of ICI are assumed to be known, computing the latter from the time correlation function of the channel [54]. The results of this section show the performance of the LMMSE ICI estimators which ignore spatial correlation from (5.31), the one which includes spatial correlation from (5.32), and also the LS ICI estimator from (5.30).

Table 5.2 shows the power delay profile of the channel impulse response considered in the simulations. The same power delay profile was used for the  $M_T M_R$  channels between each transmit-receive antenna pair. The simulations were done assuming a Kronecker spatial correlation model, where the matrix  $\mathbf{R}$  from 5.3.2 is decomposed as  $\mathbf{R} = \mathbf{R}_t \otimes \mathbf{R}_r$ , with

$$\mathbf{R}_t = \mathbf{R}_r = \begin{pmatrix} 1 & 0.9 & 0.7 & 0.5 \\ 0.9 & 1 & 0.9 & 0.7 \\ 0.7 & 0.9 & 1 & 0.9 \\ 0.5 & 0.7 & 0.9 & 1 \end{pmatrix}. \quad (5.36)$$

Figure 5.6 shows the channel estimation MSE over the SNR in a  $4 \times 4$  setup, for  $f_d T = 0.18$ . It can be seen that the proposed KL-BEM outperforms the DPS-BEM for every SNR level. On the other hand, only a small gain is observed by increasing the order when spatial correlation is considered, while the other methods achieve significant gains.

Figure 5.7 plots the resulting channel estimation MSE over the normalized Doppler spread for a fixed SNR = 30 dB. Again, the proposed estimator outperforms the LS estimator with the DPS-BEM experiencing a constant gain for every considered Doppler spread values.

Figure 5.8 shows the channel estimation MSE over the OFDM symbol index. In this case the results are again better when the proposed KL-BEM is used, but the error in the central symbols of the block is lower than in the edges. This would allow for the definition of a windowed estimation algorithm (see Section 6.2.2), where only those symbols are considered to make estimations in order to lower the estimation errors.

These results shows that with a low-order BEM in this highly spatially correlated environment, the same performance can be achieved as with higher order BEMs which ignore this correlation.

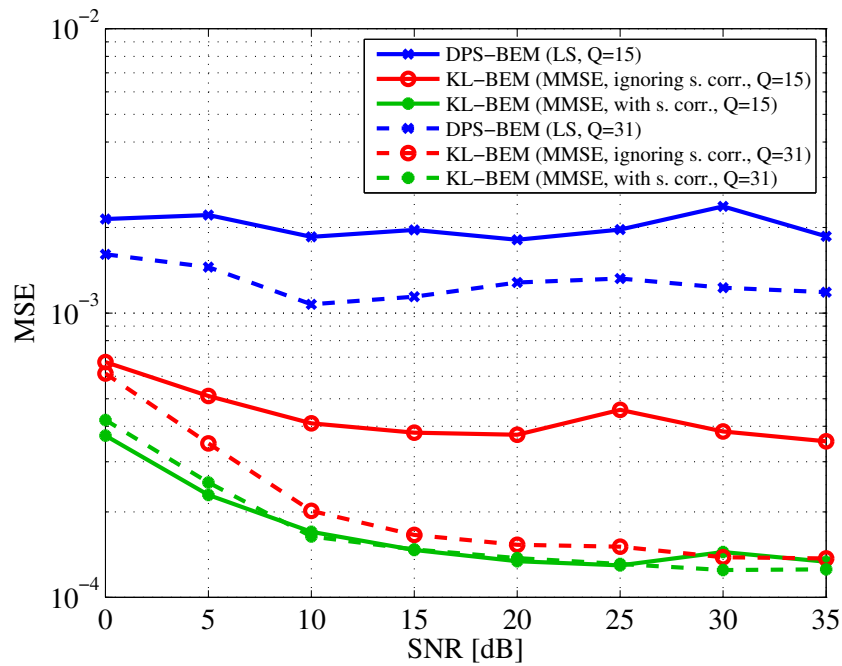


Figure 5.6: MSE over SNR of the channel matrix estimation for the  $4 \times 4$  MIMO system, a normalized Doppler spread value  $f_d T = 0.18$ , and under spatially correlated channels.

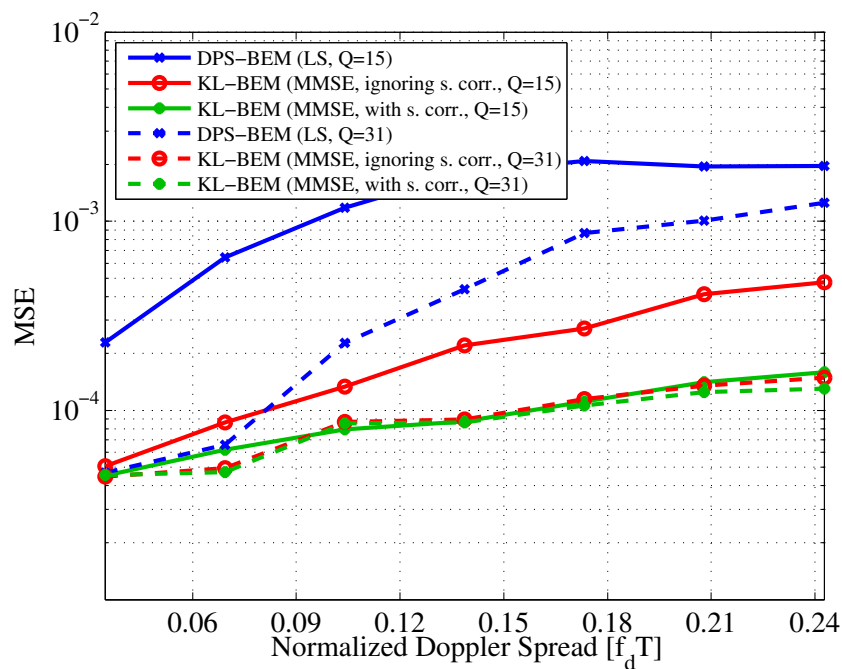


Figure 5.7: MSE over normalized Doppler spread of the channel matrix estimation for the  $4 \times 4$  MIMO system, a fixed SNR = 30 dB, and under spatially correlated channels.

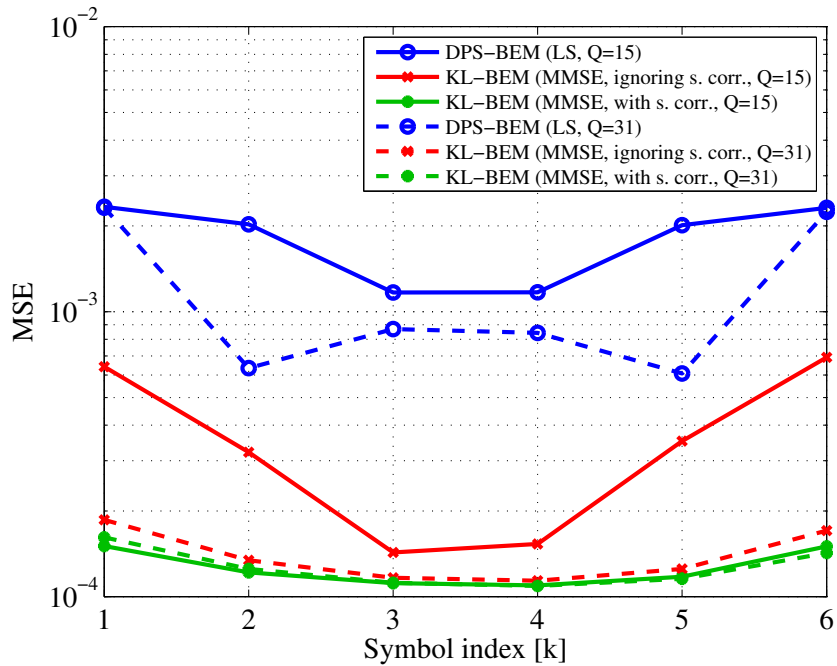


Figure 5.8: MSE over OFDM symbol index of the channel matrix estimation for the  $4 \times 4$  MIMO system, a fixed SNR = 30 dB, a normalized Doppler spread value  $f_d T = 0.18$ , and under spatially correlated channels.

## 5.5 Conclusions

In this chapter, a technique for the estimation of rapidly time-varying channels in MIMO-OFDM systems has been presented. The method utilizes a BEM obtained from a low-rank approximation to the LMMSE estimation of the ICI. The proposed approach incorporates the knowledge of the channel Doppler spectrum and does not require a specific pilot subcarrier structure. The results of computer simulations show that the proposed BEM exhibits a superior performance when estimating and canceling the ICI of rapidly time-varying MIMO-OFDM channels with non-flat Doppler spectra.

---

## Chapter 6

# Experimental Evaluation under Doubly-Selective Channels

Experimental performance evaluations of 4G technologies in high-mobility situations are scarce in the literature due to the huge difficulties of carrying out experiments in such scenarios. In this chapter, we follow an approach where the time-selective wireless channels of high mobility situations are recreated from experiments carried out at low speeds and hence are more cost-efficient to implement [72]. The approach consists in time-interpolating Orthogonal Frequency Division Multiplexing (OFDM) symbols prior to its transmission over the air, which leads to a reduction of the bandwidth of the whole OFDM signal. This produces OFDM waveforms which convey exactly the same information as the original one but with a reduced subcarrier spacing, hence artificially increasing the waveform sensitivity to Inter-Carrier Interference (ICI). At reception, and prior to its demodulation, the interpolation operation is inverted via a simple decimation operation. The resulting OFDM symbols are affected by ICI similarly as if they were transmitted over a high-mobility wireless channel. In fact, interpolating the original signal by a factor  $I$  will affect the transmitted signal similarly to what would happen if it were transmitted while moving at  $I$  times the original speed.

This chapter is partly based on the publications [85, 86] and it is organized as follows. Section 6.1 summarizes the signal model and the technique employed to induce large Doppler spreads, Section 6.2 describes the estimation and equalization techniques used to obtain the results, Section 6.3 describes the hardware testbed deployed for the measurements, and Section 6.4 shows the results obtained after the campaign. Finally, Section 6.5 concludes the chapter.

## 6.1 Signal Model

Following the notation already defined in Chapter 2, let  $\mathbf{x}_{k,m} \in \mathbb{C}^{N \times 1}$ ,  $k = 1, \dots, K$ ,  $m = 1, \dots, M_T$  be the column vector that represents the  $N$  complex-valued information symbols transmitted in the  $k$ -th OFDM symbol over the  $m$ -th antenna. Such vectors contain data, pilot and guard symbols. Similarly,  $\mathbf{s}_{k,m} \in \mathbb{C}^{N_T \times 1}$  contains the  $N_T$  samples corresponding to the  $k$ -th OFDM symbol transmitted over the  $m$ -th antenna.

Elaborating the signal model of a  $M_T \times M_R$  MIMO-OFDM system, the discrete-time representation of the transmitted MIMO-OFDM symbols is

$$\mathbf{s}_k = (\mathbf{I}_{M_T} \otimes \mathbf{G}_1 \mathbf{F}^H) \mathbf{x}_k, \quad k = 1, \dots, K, \quad (6.1)$$

where  $\mathbf{x}_k = [\mathbf{x}_{k,1}^T, \mathbf{x}_{k,2}^T, \dots, \mathbf{x}_{k,M_T}^T]^T$  is the  $NM_T \times 1$  column vector containing the information, pilot and guard symbols transmitted in the  $k$ -th MIMO-OFDM symbol;  $\mathbf{F}$  is the standard  $N \times N$  Discrete Fourier Transform (DFT) matrix;  $\mathbf{G}_1$  is a  $N_T \times N$  matrix which appends the  $N_g$  samples of the cyclic prefix;  $\otimes$  denotes the Kronecker product;  $\mathbf{I}_{M_T}$  is the  $M_T \times M_T$  identity matrix; and  $\mathbf{s}_k = [\mathbf{s}_{k,1}^T, \mathbf{s}_{k,2}^T, \dots, \mathbf{s}_{k,M_T}^T]^T$  is the  $N_T M_T \times 1$  column vector with the samples of the  $k$ -th MIMO-OFDM symbol. We assume the samples in  $\mathbf{s}_{k,m}$  are serially transmitted over the  $m$ -th antenna at a sampling rate  $F_s = 1/T_s$ , where  $T_s$  is the sampling period.

The information symbol vectors are constructed as  $\mathbf{x}_{k,m} = \mathbf{P}_{k,m} \mathbf{p}_{k,m} + \mathbf{D}_{k,m} \mathbf{d}_{k,m}$  where  $\mathbf{p}_{k,m}$  is a  $P \times 1$  vector containing the pilot symbols in the  $k$ -th OFDM symbol transmitted over the  $m$ -th transmit antenna, whereas  $\mathbf{P}_{k,m}$  is the  $N \times P$  matrix that defines the positions of the pilots in such a symbol. Similarly,  $\mathbf{d}_{k,m}$  is the  $D \times 1$  vector containing the data symbols and  $\mathbf{D}_{k,m}$  is the  $N \times D$  matrix that defines their positions. Data symbols are the output of a QAM constellation mapper whose inputs are the channel encoded source bits. Note that  $P + D < N$ , with  $N - (P + D)$  being the number of guard subcarriers. Matrices  $\mathbf{P}_{k,m}$  and  $\mathbf{D}_{k,m}$  consist only of ones and zeros, and they are designed so that data and pilots are assigned to disjoint subcarriers. For example, according to the Mobile WiMAX standard, pilot subcarriers allocated in the  $m$ -th antenna are set to zero in all other antennas.

When transmitting MIMO-OFDM symbols over time-varying channels, the amount of ICI relates to the normalized Doppler spread value given by  $D_n = f_d T$ , where  $f_d$  is the maximum Doppler frequency and  $T = NT_s$  is the duration of an OFDM symbol excluding the cyclic prefix. It is possible to adjust the parameter  $T$  by time interpolation by a factor  $I$ , yielding an OFDM symbol duration  $T^I = IT_s N$  [72]. Therefore, the normalized Doppler spread impacting the time-interpolated OFDM signal is

$$D_n^I = f_d T^I = f_d I T_s N = \frac{T_s N I f_c v}{c} = \frac{T_s N f_c}{c} v^I,$$

with  $f_c$  the carrier frequency,  $c$  the speed of light, and  $v^I = Iv$  the emulated speed as a result of an actual measurement speed  $v$  and a time-interpolation factor  $I$ . Consequently, enlarging

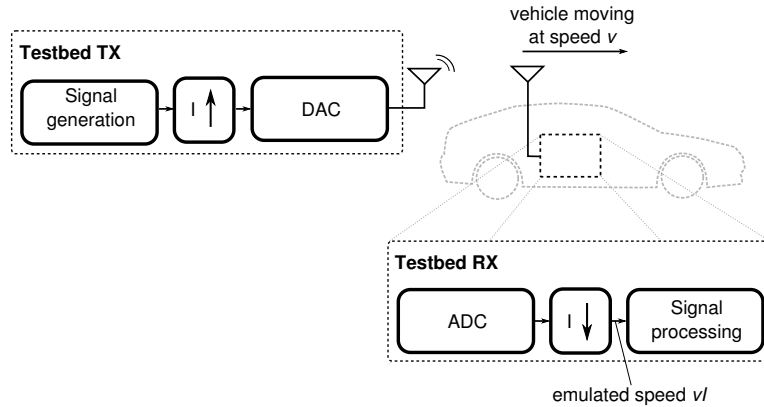


Figure 6.1: Block diagram of the outdoor-to-outdoor measurement setup. The transmit antennas are placed outdoors and the receive antennas are installed outside the car on its roof. The interpolator at the transmitter side and the decimator at the receiver side enable the recreation of high speed conditions during low speed experiments. The corresponding outdoor-to-indoor setup is basically the same. The only difference is that receiving antennas are placed inside the car instead of outside.

the symbol length  $T^I$  allows for the emulation of a velocity  $v^I$ , which is  $I$  times higher than the actual speed of the receiver, namely  $v$ .

Figure 6.1 shows the graphical representation of a measurement setup designed according to the previous premises. Interpolating the MIMO-OFDM waveforms prior to its transmission allows for emulating high velocity conditions while conducting low-velocity experiments. Due to the interpolation step, signals over the air will suffer from severe ICI degradation, although the maximum Doppler frequency is low.

It should be noticed that interpolation does not allow for a perfect recreation of high mobility channels because the signals over the air have a reduced bandwidth and are less sensitive to the channel frequency selectivity.

Nevertheless, note that in this work we are mostly interested in conducting experiments to test the performance of ICI cancellation methods in WiMAX receivers over real-world channels, rather than channel equalization methods which can be tested in static experiments. Time interpolation does not reproduce the exact conditions of high mobility scenarios but provide a cost-efficient approximation to them [73].

## 6.2 Receiver Structure

Figure 6.2 shows the block diagram of the receiver structure utilized along this work. The samples captured with the hardware equipment are first decimated to undo the interpolation applied at the transmitter to induce the ICI. The decimated samples are input to an OFDM

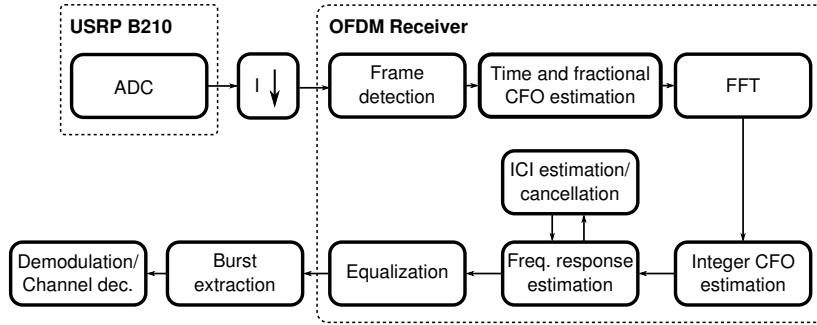


Figure 6.2: Block diagram of the receiver structure with decimation and the OFDM receiver with ICI cancellation. The OFDM receiver is the same for the experimental and the simulation results.

receiver that performs frame detection, and time and fractional Carrier Frequency Offset (CFO) estimation before the DFT; and channel estimation, ICI cancellation, data subcarriers equalization, and channel decoding after the DFT. Figure 6.2 shows the general structure of the receiver. The same OFDM receiver is used to obtain the experimental results and the simulation results.

The ensuing subsections present a more detailed description of each processing block represented in Figure 6.2.

### 6.2.1 Frame Detection and Synchronization

Frame detection is carried out using the correlation properties of the preamble symbol. WiMAX defines a preamble symbol with pilot subcarriers generated from a pseudo-noise sequence modulated as BPSK, with a spacing of two guard subcarriers between them. This structure leads to a three-fold repetition in the time domain, which can be exploited for frame detection, and time and fractional CFO estimation. Integer frequency shifts are corrected after the DFT by performing a cross-correlation between the differential sequences of the transmitted and received preamble pilot sequences, algorithms used also in the real time architecture described in Chapter 3.

### 6.2.2 ICI Cancellation and Equalization

The frequency response and ICI estimation follows the steps already described in Chapter 5 using the Discrete Prolate Spheroidal (DPS) Basis Expansion Model (BEM) and the Karhunen-Loève (KL) BEM. Such a DPS-BEM is built on the Slepian sequences arising from time sequences whose energy is localized on a given frequency interval. For the purpose of ICI estimation, the frequency interval is the one corresponding to the Doppler spectrum, whose domain is bounded by the maximum Doppler frequency. Recall that the use of DPS-BEMs is

equivalent to assuming a time-selective channel with a flat Doppler spectrum. Consequently, to determine the specific DPS-BEM appropriate for a given scenario, it is necessary to know the mobile speed, and more specifically, the emulated speed after interpolation [96]. The same applies to the KL-BEM, but under the assumption of a Jakes Doppler spectrum, which also depends on the maximum Doppler frequency. Regarding the estimation technique, the Least Squares (LS) ICI method from (5.30) is used, since second-order statistics of the channel in the time domain have not been obtained experimentally.

Once the full frequency response matrices for all antenna pairs are obtained, both ICI cancellation and equalization of the received signal is done to obtain estimates of the information symbols  $s_k$ . In the literature, both Block Interference Cancellation (BIC) and Sequential Interference Cancellation (SIC) schemes have been proposed [21, 39]. In this chapter, a LMMSE SIC receiver of seven taps is used to remove the ICI and equalize the channel. Such a method has been chosen due to its good trade-off between computational cost and performance.

The ICI estimation algorithm described in Chapter 5 works on groups of  $R$  OFDM symbols, and as it is shown in the results section (and also shown in Figure 5.8), the estimation error inside the group is not uniform along the OFDM symbols. Lower errors are achieved in the central symbols and this is taken into account by the equalizer implemented in our receiver. Denoting with  $\hat{C}_r$  the matrix with the estimated coefficients, as defined in (5.30), for the  $r$ -th group of  $R$  OFDM symbols inside the frame of  $K$  OFDM symbols, ICI cancellation and channel equalization is carried out according to the following steps:

1. Obtain the matrices  $\hat{C}_r$  for the  $K - R + 1$  groups in a frame.
2. Remove ICI from each OFDM symbol as follows:
  - (a) For symbols  $k \in [1, R/2]$ , ICI is suppressed with the coefficients obtained from  $\hat{C}_1$ .
  - (b) For symbols  $k \in [R/2+1, K-R/2]$ , ICI is suppressed with the coefficients obtained from  $\hat{C}_{k-R/2+1}$ .
  - (c) For symbols  $k \in [K - R/2 + 1, K]$ , ICI is suppressed with the coefficients obtained from  $\hat{C}_{K-R+1}$ .
3. Obtain a new frequency response estimate from the ICI-reduced received signal and return to step 1.

As it can be seen, except for the first and last symbols of the frame, ICI is estimated and canceled for the central OFDM symbol of each set. The final equalization of the ICI-reduced signal is done by zero forcing. Detected information symbols are demapped and sent to a Viterbi decoder to obtain the information bits.

Parameter	Value
Sampling frequency	8 MHz
Useful bandwidth	7 MHz
Number of subcarriers	1024
Number of data subcarriers	720
Number of pilot subcarriers	120
Subcarrier spacing	7.81 kHz
Cyclic prefix length	128 samples
Permutation zone	PUSC

Table 6.1: Parameter values of the WiMAX profile used in the experiments.

### 6.3 Experimental Setup

The testbed employed for the experimental evaluation in this work is an upgrade of that employed in the measurement campaigns described in [72, 85] which, at the same time, has evolved from the one described in [74]. The testbed consists of three USRP B210 boards [9] (see Figs. 6.3 and 6.4) built from the AD9361 chip [3] by Analog Devices, which supports a continuous frequency coverage from 70 MHz to 6 GHz; full-duplex Multiple-Input Multiple-Output (MIMO) operation with two antennas and up to 56 MHz of bandwidth; USB 3.0 connectivity; on-chip 12 bit Analog-to-Digital Converters (ADCs) and Digital-to-Analog Converters (DACs) up to 61.44 Msample/s; automatic gain control; and configurable transmit and receive gain values.

A single board is used in continuous transmit-only mode for implementing the base station transmitter for the downlink. The base station is equipped with two Mini-Circuits TVA-11-422 high-power amplifiers [6], two Interline SECTOR IS-G14-F2425-A120-V vertically polarized transmit antennas [5], and an Ubiquity AM-2G15-120 cross polarized transmit antenna [10]. Notice that a single vertically polarized antenna was used for the Single-Input Single-Output (SISO) transmissions, while the cross polarized antenna was employed for measuring the  $2 \times 2$  MIMO ones.

The remaining two USRP B210 boards are used for implementing two different mobile receivers, both mounted on a car. The first one is connected to a couple of eRize ERZA240-09MBR omnidirectional 9 dBi-gain antennas placed outdoors, on the roof of the car. The second mobile receiver is connected to another two omnidirectional antennas placed inside the car, between the two front seats. Using both mobile receivers allows us to capture, at the same time, the signals transmitted by the base station to both outdoor and indoor receivers.

With respect to the software, we use a multi-thread receiver implemented in C++ with Boost and using the Ettus USRP Hardware Driver (UHD) software. The main thread of the receiver

is responsible for retrieving the samples coming from the USRP through the USB 3.0 bus and store them in a set of buffers in the main memory of a host laptop. The second thread reads the samples from such buffers and saves them persistently in a dedicated solid-state drive. Finally, there is a low-priority thread for logging important information for documenting the measurement campaign. On the other hand, the transmitter is a single-thread process since the same signals are cyclically transmitted over-the-air. Therefore, the signals to be radiated are first stored in a temporary buffer and next transmitted in a loop to the USRP through the USB 3.0. The rest of the software was implemented in Matlab.

For the measurements we use the WiMAX profile corresponding to 7 MHz of bandwidth at a sampling rate of  $F_b = 8 \text{ Msample/s}$ ,  $N = 1024$  subcarriers, and a cyclic prefix of  $1/8$  ( $N_g = 128$ ). Table 6.1 summarizes the parameter values of this WiMAX profile. At the base-station, once the OFDM signals were generated, they are time interpolated with the interpolation factors  $I \in \{4, 12, 20\}$ , hence producing signals with bandwidth values ranging from 1.75 MHz for  $I = 4$  to 350 kHz for  $I = 20$ . Next, the energy of the signals corresponding to each interpolation factor  $I$  is scaled (in the time domain) by a factor  $\sqrt{I}$  in order that signals corresponding to all interpolation factors be transmitted with the same energy, and thus keeping constant the energy per bit sent over the air regardless the value of the interpolation factor. The three time-interpolated frames are then frequency-shifted 1.2 MHz to avoid the DC leakage at both the transmitter and the receiver. Hence, the DC subcarrier is frequency-shifted 1.2 MHz to avoid the distortion caused by the DC leakage to the subcarriers around the DC, since the subcarrier spacing is reduced and we are dealing with direct-conversion transceivers. In order to facilitate the Signal-to-Noise Ratio (SNR) estimation at the receiver, after transmitting the three time-interpolated frames the transmitter is kept silent during a small time lapse which allows for estimating the noise variance at the receiver. These small silent periods are also useful to ensure that the channel is free of interferences. Finally, all generated signals are stored in a file in the disk of the base station transmitter.

Once the transmit signals have been generated, the base-station is notified and the over-the-air transmission process starts. First, the signals are read from the corresponding source file and transferred to the USRP, where they are again interpolated in the FPGA before reaching the DACs. Note that this interpolation stage is needed for adapting the signal sampling rate to the sampling frequency of the DACs, thus not affecting the signal bandwidth. Next, the signals are up-converted to the central frequency  $f_c = 2.6 \text{ GHz}$  (thus the final subcarrier is equal to 2.6 GHz plus the 1.2 MHz, resulting 2.6012 GHz), pre-amplified inside the USRP (configured with a gain value of 60 dB out of 89.5 dB), amplified by the two Mini-Circuits TVA-11-422 high-power amplifiers (one per transmit antenna) at their maximum gain of 40 dB, and finally radiated by the antennas (we use the vertically polarized transmit antennas for SISO transmissions, while the cross polarized ones are employed for  $2 \times 2$  MIMO transmissions). The mean transmit power value measured at each antenna input is +17.5 dBm when a single transmit antenna is



Figure 6.3: Base station downlink transmitter is placed outdoors, on the second floor of the CITIC building located in the Campus de Elviña at the University of A Coruña. Note that only one of the two vertically polarized antennas is used for  $1 \times 1$  transmissions, while both cross polarized antennas are used for the  $2 \times 2$  MIMO transmissions.

used. In case both transmit antennas are employed, the transmit gain is reduced in 3 dB per antenna to keep the total transmit power equal despite of the number of transmit antennas.

Figure 6.3 shows the base-station placed outdoors, on the second floor of the CITIC building located in the Campus de Elviña at the University of A Coruña. It also shows the power amplifiers, the antennas (vertically or cross polarized), the USRP B210, and the laptop running the software for the base-station. Looking at the picture of the cross-polarized antennas in Fig. 6.3 one can also see part of the road traversed by the car during the measurements.

The two receivers are also built around the USRP B210 and the UHD with the software installed on two laptops, one per receiver. Notice that during the measurements, the acquired signals are persistently stored in dedicated solid state drives attached to laptop receivers, but they are not processed using the WiMAX receiver at that moment. As shown in Fig. 6.4, the two outdoor receive antennas are stucked on the roof of the car used for measuring and they are connected directly to the USRP B210, which is powered by its corresponding laptop. The receive gain of the USRP is set to 35 dB (out of 73 dB), ensuring a linear operation. The second receiver is completely installed inside the car used for the measurements, with the antennas between the two front seats of the car. We use another laptop for running the receiver software and for persistently storing the signals acquired by the indoor receiver. Unlike the outdoor receiver, the receive gain of the indoor receiver is set to 45 dB to better accommodate the amplitude of the acquired signals to the range of the ADCs while ensuring that the receive signal is not distorted by the amplifiers.

Figures 6.5 and 6.6 show the measurement scenarios. In the first scenario the length of the course is 240 m, which is traversed by the car in 43.2 s at a speed of 20 km/h. In the second



Figure 6.4: Mobile receivers mounted on a car. Two antennas corresponding to the outdoor receiver are placed on the roof of the car, while another two antennas for the second receiver are inside the car, between the two front seats.

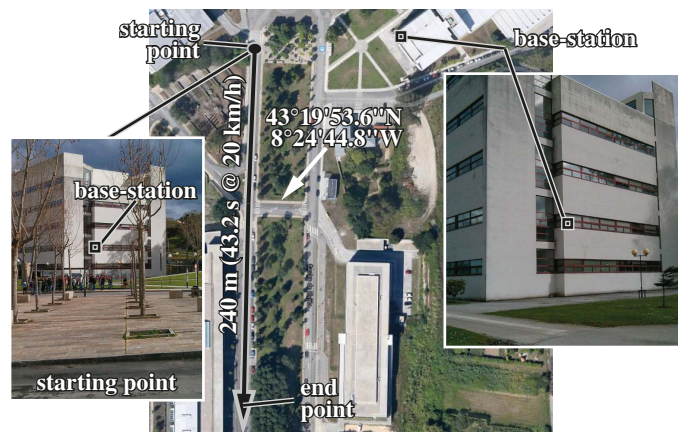


Figure 6.5: First measurement scenario at the Campus de Elviña, A Coruña. The measurement trajectory as well as the location of the base station are shown.

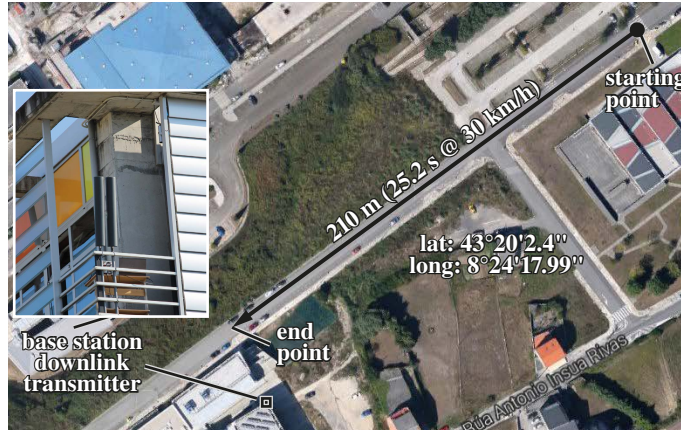


Figure 6.6: Second measurement scenario at the Campus de Elviña, A Coruña. The measurement trajectory as well as the location of the base station are shown.

scenario, the starting to the end points there is a distance of 210 m, which is traversed by the car in 25.2 seconds at a constant speed of 30 km/h, up to four times.

### 6.3.1 Physical Layer Configuration

The OFDM symbol structure of the transmitted signal follows the downlink of Mobile WiMAX standard regarding subcarrier allocation, symbol mapping and channel encoding. The frames consists of  $K = 25$  symbols with the first one reserved for the preamble signal transmitted only by the first antenna. The permutation matrices  $\mathbf{P}_k^{(m)}$  and  $\mathbf{D}_k^{(m)}$  are generated according to the PUSC (Partial Usage of Subcarriers) zone with the corresponding modifications for MIMO as specified in the standard, and pilot subcarriers on  $\mathbf{p}_k^{(m)}$  generated as a boosted BPSK sequence obtained by mapping the output of a linear feedback shift register. Channel coding is performed by the convolutional encoder defined in the standard, which features tail-biting to terminate coding blocks.

Two frame and bursts configuration have been tested. In the first burst scheme, the same modulation and coding is used for all the symbols of a frame, and it is maintained during all the course, repeating the process for each interpolation factor. The other configuration carries six bursts with the modulation and channel coding profiles: 4-QAM 1/2, 4-QAM 3/4, 16-QAM 1/2, 16-QAM 3/4, 64-QAM 1/2, and 64-QAM 3/4. Each burst spans during four consecutive OFDM symbols along all the available data subcarriers. Moreover, in order to ensure similar channel characteristics for all the interpolation factors in each measurement, a super-frame consisting of four different parts is built. The first part is a small time period during which the base station is kept silent to allow for noise variance estimation at the receiver as it was already explained. The remaining three parts are built from the same Mobile WiMAX frame consisting of the six burst plus the preamble that was described above. Consequently, the second part of the super-frame

corresponds to the aforementioned Mobile WiMAX frame interpolated in time by the factor  $I = 4$ . Next, the third part is the same as the second one but using  $I = 12$ , while the fourth part employs  $I = 20$ . Finally, the super-frame is cyclically transmitted from the base station to both mobile receivers, one placed outside the car and the other installed inside.

Finally, under the  $2 \times 2$  MIMO configuration, the slots of a burst (see Section 2.3) are mapped alternatively between transmit antennas, and consequently the burst size is doubled to fill the same frequency range. Therefore, this MIMO configuration focuses on doubling the throughput, and not on obtaining a more robust link.

## 6.4 Results

This section presents the results obtained from the measurements described above. We also carried out simulations to support the experimental results. Simulations were designed to create scenarios comparable to those obtained from the measurements. Parameters estimated from the real-data captured are the mean SNR of each frame, and the K-factor of the wireless channel. The mean SNR is estimated taking as a reference the noise variance estimated during the silence preceding each frame; and the K-factor is estimated and averaged for all frames. Regarding simulations, the estimated mean SNRs for each frame in the real scenario are applied to the simulated transmissions, all with the same average K-factor. Finally, full characterization of the channel frequency responses or spatial covariance matrices have not been obtained, so simplified assumptions have been made while conducting the simulations. Basically, we assumed a frequency-flat spatially-uncorrelated MIMO channel. The frequency-flat assumption arises from the fact that for the highest interpolation factors, the bandwidth of the transmitted signals will be rather narrow, and therefore the frequency selectivity observed by the receiver would be negligible. As for the MIMO channel, the coefficients for each pair of antennas are drawn from independent Rice distributions, although not identically distributed, picking random complex mean values for each MIMO channel matrix entry.

### 6.4.1 ICI Estimation Algorithms Evaluation

In this section, results of measurements of WiMAX downlink transmissions are shown. In this case, frames with the same interpolation factor are transmitted consecutively, corresponding to the first frame configuration described in Section 6.3.1. The plots shown in this section correspond to a round along the course of the first scenario described in Section 6.3. An ICI estimation employing DPS-BEM and KL-BEM, applied to ICI estimation in (5.30), was used to test their performance in real scenarios. To measure the performance of the different estimators, Error Vector Magnitude (EVM) values are computed from each burst, measuring

the error against the transmitted subcarriers.

$$\text{EVM}_F = \frac{\sum_{k=1}^K \sum_{n=1}^N \|\hat{\mathbf{x}}_k[n] - \mathbf{x}_k[n]\|^2}{\sum_{k=1}^K \sum_{n=1}^N \|\mathbf{x}_k[n]\|^2}, \quad (6.2)$$

being  $\text{EVM}_F$  the mean EVM for the  $F$ -th frame. Note that the original transmitted symbols  $\mathbf{x}_k$  are used to normalize the EVM. Moreover, a global estimation of the SNR received during each frame is computed by measuring the signal power in the data subcarriers, and the noise variance in the guard subcarriers not affected by ICI.

The frequency response estimators used in this sections are a pilot-based regularized LS estimator, and a pilot-based linear interpolation estimator. The first one is given by:

$$\hat{\mathbf{g}}_k = \mathbf{F}_L (\mathbf{F}_k^H \mathbf{F}_k + \alpha \mathbf{I}_L)^{-1} \mathbf{F}_k^H \mathbf{Q}_k^{-1} \mathbf{y}_k^{(p)}, \quad (6.3)$$

with  $\mathbf{y}_k^{(p)} = \mathbf{P}_k^T \mathbf{y}_k$ ,  $\mathbf{Q}_k = \text{diag} \{ \mathbf{p}_k \}$ ,  $\mathbf{F}_L$  denotes the  $N \times L$  matrix with the first  $L/2$  and last  $L/2$  columns of the DFT matrix. Although it is common to define this estimator taking the first  $L$  columns of the DFT matrix, this variation is used to compensate possible timing offset estimation errors in both directions. Also, the channel delay is set to  $L = 32$  and, although after interpolation the frequency selectivity of the channel diminishes and a lower  $L$  could be selected, a higher value is used to not take advantage of the features of this measurement setup. Finally,  $\mathbf{F}_k = \mathbf{P}_k^T \mathbf{F}_L$  is a  $P \times L$  matrix with the rows at the pilot positions of the  $k$ -th OFDM symbol, and  $\alpha$  is a regularization coefficient dependent on the estimated SNR. Also, we use the following pilot-based linearly interpolated frequency response estimator, given by

$$\hat{\mathbf{g}}_k = \mathbf{A}_k \mathbf{Q}_k^{-1} \mathbf{y}_k^{(p)}, \quad (6.4)$$

with  $\mathbf{A}_k$  being a  $N \times P$  matrix with the linear interpolation coefficients. Finally, an estimator which assumes to know all the transmitted subcarriers is used as a reference and will be denoted as ‘‘Perfect estimator’’.

In order to ease the visualization of the results, median values of both the EVM and the average SNR are shown. These median values are computed by grouping the frames in clusters, splitting the trajectory of the mobile receiver in sections of equal length, and assigning the corresponding median value to that sector.

Figures 6.7 and 6.8 respectively show the results corresponding to the perfect estimator and the pilot-based LS channel estimator, considering the ICI estimation method with a DPS-BEM, and order values  $Q = 3$ ,  $Q = 4$  and  $Q = 5$ . As a reference, the results when no ICI cancellation is applied are also shown. The interpolation factor was  $I = 32$ , hence generating a normalized Doppler spread value  $D_n = 0.2$ , which is equivalent to a speed of 640 km/h in our measurement

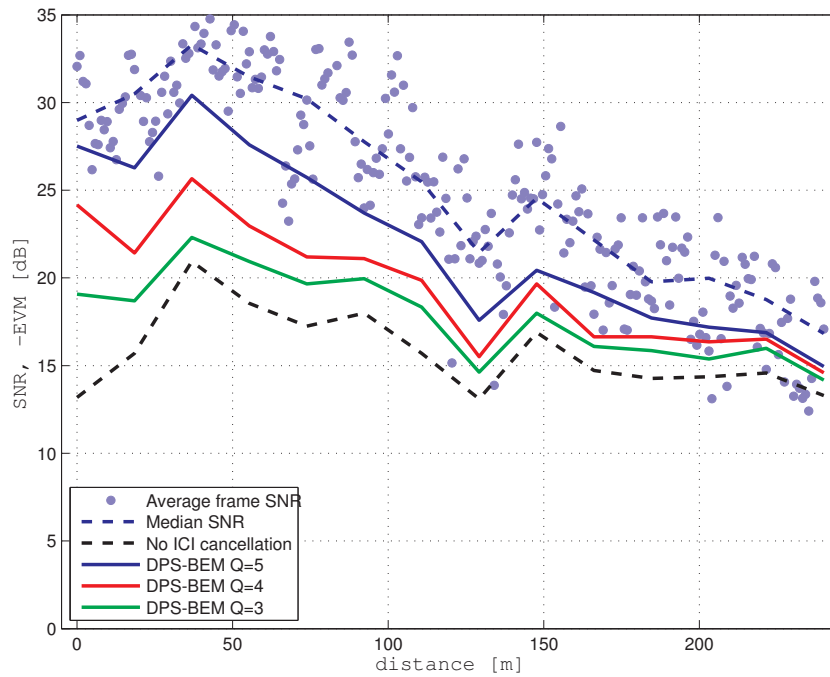


Figure 6.7: Perfect channel estimator and DPS-BEM with orders  $Q = \{3, 4, 5\}$  and with interpolation factor  $I = 32$ .

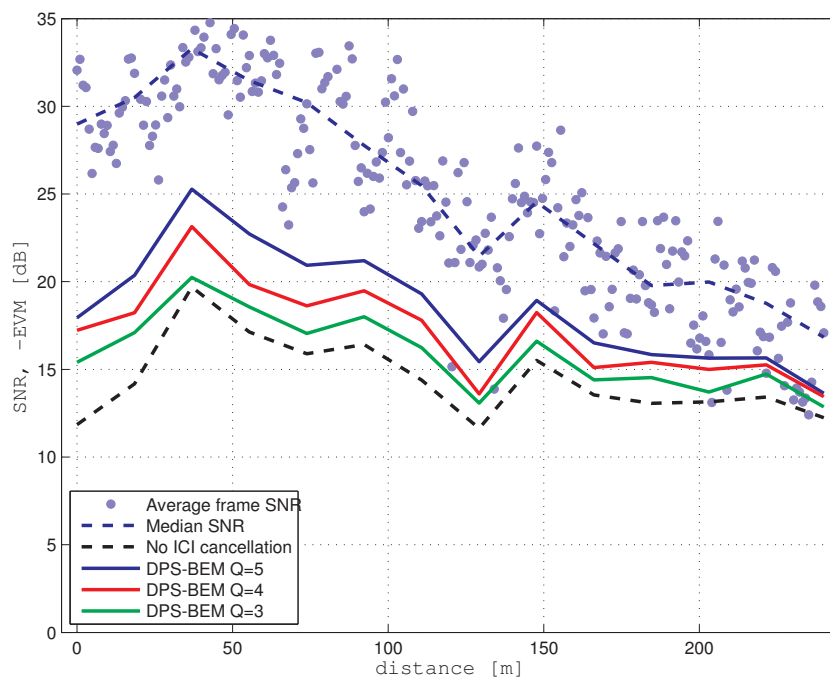


Figure 6.8: Comparison of pilot-based channel estimator and DPS-BEM with orders  $Q = \{3, 4, 5\}$  and with interpolation factor  $I = 32$ .

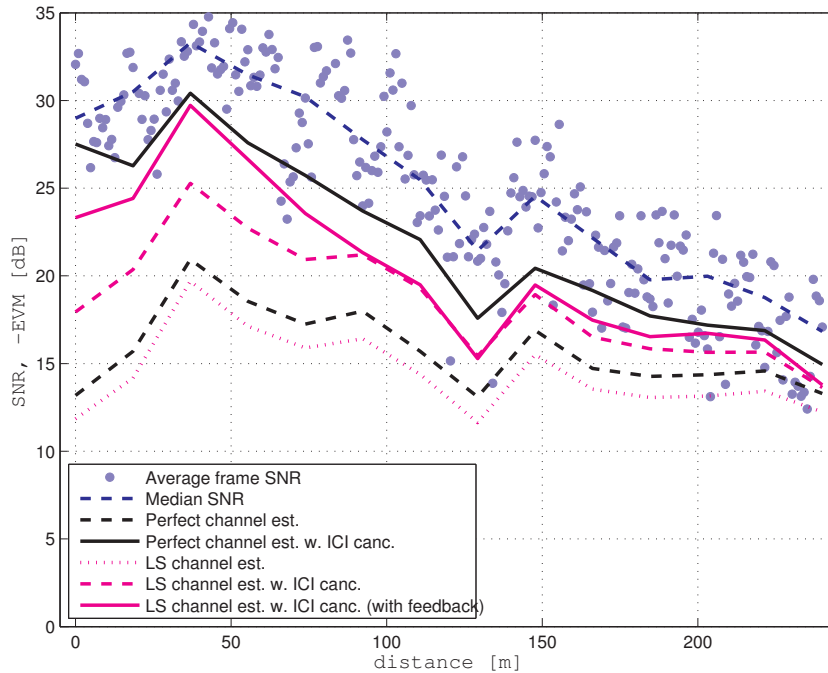


Figure 6.9: Comparison of perfect channel estimator and a pilot-based channel estimator (LS) with and without feedback, both with interpolation factor  $I = 32$ .

conditions. These experimental measurements verify that increasing the order of the BEM has an important impact on the quality of the ICI estimation, which translates into better EVM values after cancellation. Also, similar behavior is obtained with both channel estimators, although a loss is observed with the pilot-based LS, given that less training is considered to obtain the channel coefficients.

Figure 6.9 shows a performance comparison between the LS pilot-based estimator and the perfect channel estimator. Such comparison provides a better view of the loss in performance with the pilot-based estimator. In the case of perfect channel estimation, it is clear that almost all ICI is suppressed after the ICI cancellation step, getting very close to the bound defined by the estimated SNR. Comparatively, the pilot-based estimator performs worse, although it obtains results better than the perfect channel estimator which ignores ICI. Additionally, an iterative frequency response estimator is tested in which the decided symbols after equalization are used with the perfect estimator to obtain a refined ICI canceled signal, denoted in the plots with the annotation “with feedback”. EVMs closer to the perfect estimator are obtained with this scheme.

Similar results are shown in Figures 6.10 and 6.11 but for interpolation factors  $I = 20$  and  $I = 12$ , which correspond to emulated velocities of 400 km/h and 240 km/h respectively. The comparative behavior between estimators is similar in all cases, and also smaller gains are obtained for the lower interpolation factors. This is in the same line as the results shown in Figures 5.3 and 5.8, where the ICI estimation MSE is larger as long as the normalized Doppler

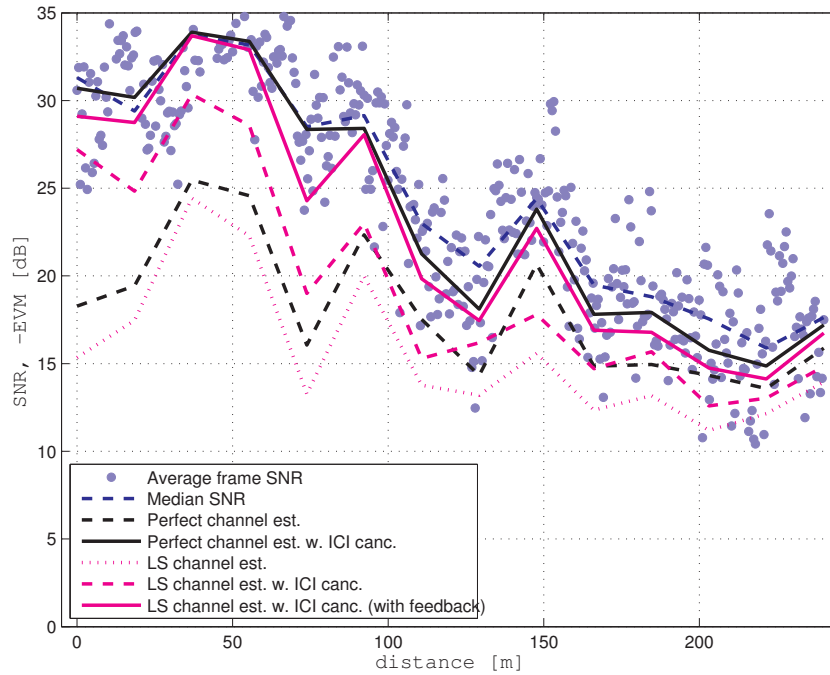


Figure 6.10: Comparison of perfect channel estimator and a pilot-based channel estimator (LS) with and without feedback, both with interpolation factor  $I = 20$ .

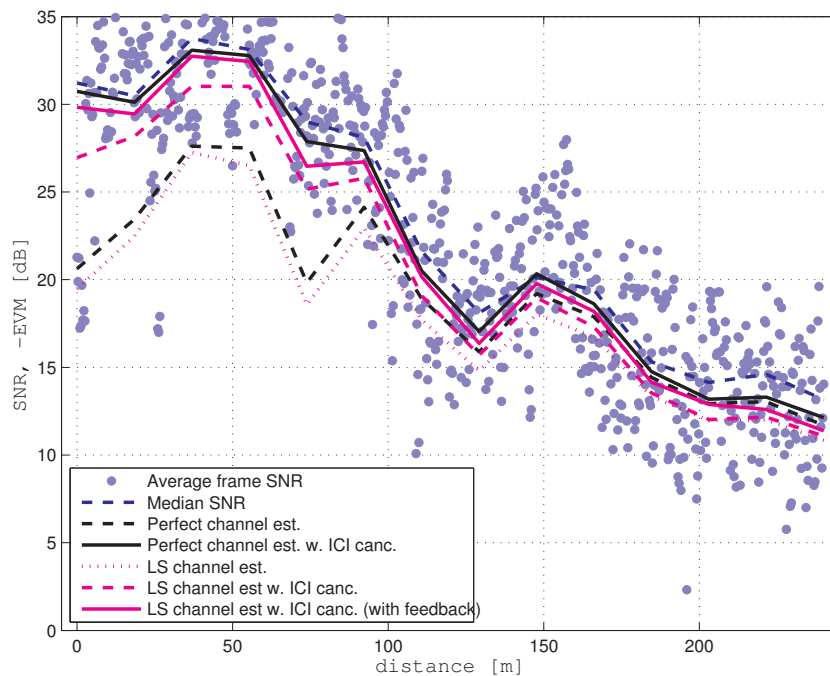


Figure 6.11: Comparison of perfect channel estimator and a pilot-based channel estimator (LS) with and without feedback, both with interpolation factor  $I = 12$ .

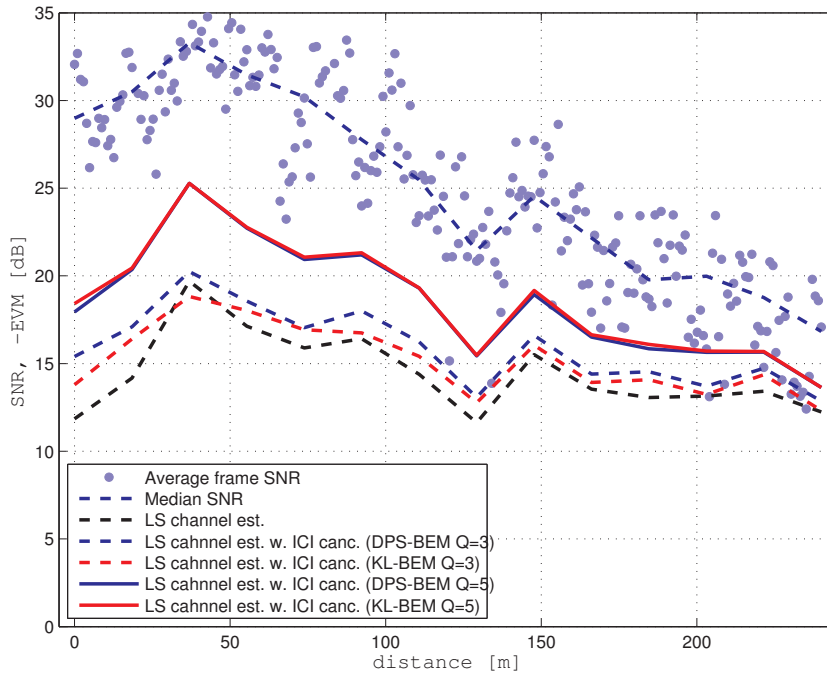


Figure 6.12: Comparison of pilot-based channel estimator (LS) with DPS-BEM and KL-BEM and interpolation factor  $I = 32$ .

spread increases.

Figure 6.12 shows the comparison of the performance of the same acquired frames processed with different BEMs, in this case the DPS-BEM and the KL-BEM, again with an interpolation factor  $I = 32$ . A Jakes Doppler spectrum was assumed when the KL-BEM was computed since the actual Doppler spectrum of the channel during the measurements was not characterized. Although for  $Q = 5$  the performance of both estimators is virtually the same, for  $Q = 3$  a small gain is obtained with the DPS-BEM. This is probably due to a mismatch between the actual Doppler spectrum during the measurements, and the one assumed when the KL-BEM is computed. Also, each frame is used to obtain a different frequency offset and corrected before channel estimation is applied. This frequency offset correction, if not accurate, can affect to the Doppler spectrum observed at the input of the channel estimator. There are methods in the literature to perform joint frequency-offset and channel estimation techniques for OFDM in time-varying scenarios, which could be useful to be used with a KL-BEM [67].

Finally, Figure 6.13 shows the performance of the pilot-based estimator with linear interpolation compared to the perfect estimator. Its performance after ICI cancellation is better than the regularized LS estimator, which can be due to the high  $L$  parameter selected. Also, this frequency response estimation algorithm is the one implemented in the real-time system described in Chapter 3, and shows that simpler estimation algorithms can provide good results regarding ICI cancellation in EVM terms.

With the results obtained in this subsection, two general observations can be made. First,

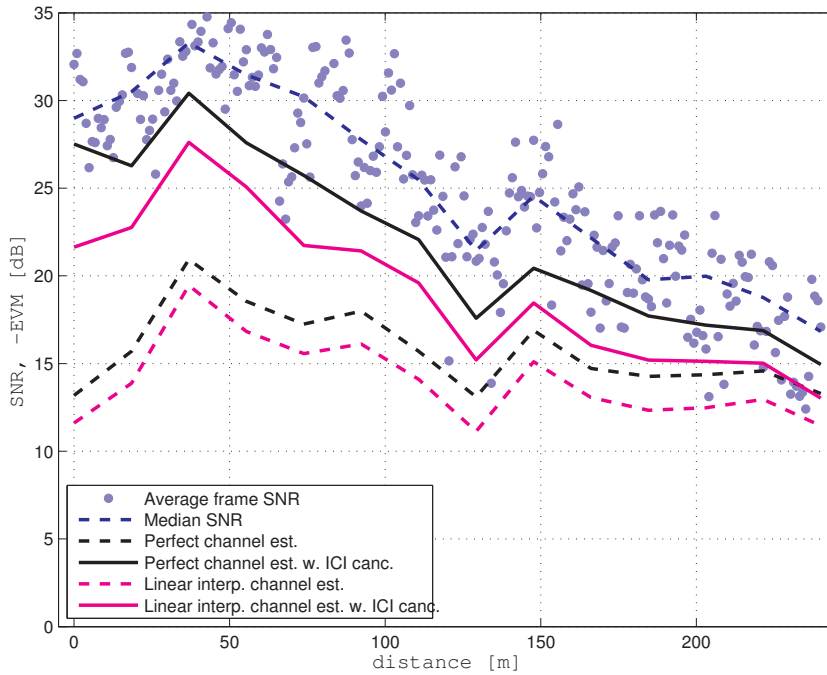


Figure 6.13: Comparison of perfect estimator and a pilot-based estimator with linear interpolation, both with interpolation factor  $I = 32$ .

the performance of the ICI estimation algorithms behave in general as predicted by previous simulations results (shown in Chapter 5), obtaining larger gains in terms of EVM when higher order BEMs are used. Also, using a DPS-BEM or a KL-BEM provides very similar results, being possible to obtain a worse performance for lower BEM orders for the case of KL-BEM if the assumed underlying Doppler model is not matched precisely. This differs with respect to the results obtained in Section 5.4.1, where the simulations were set up to perfectly match the assumptions of the model, and where synchronization issues were ignored.

## 6.4.2 Indoor, Outdoor and MIMO configurations

In this section, results with the DPS-BEM and  $Q = 5$  are shown to compare the difference in performance between signals received from the outside and the inside of the car, as well as MIMO transmissions, on the second measurement scenario. Also, in contrast to the previous subsection, frames with different interpolation factors  $I$  are sent interleaved, corresponding to the second frame configuration in Section 6.3.1. Again, the plots shown in this subsection correspond to a round along the course described in Section 6.3. Regarding the frequency response estimation, a LMMSE algorithm is used to obtain these results, given by

$$\hat{\mathbf{g}}_k = \mathbf{C}_{hh_p} (\mathbf{C}_{h_p h_p} + \sigma_w^2 \mathbf{I}_P)^{-1} \mathbf{Q}_k^{-1} \mathbf{P}_k^T \mathbf{y}_k, \quad (6.5)$$

where  $\mathbf{C}_{hh_p} = \mathbf{F}_L \mathbf{E} \{ \bar{\mathbf{h}}_k \bar{\mathbf{h}}_k^H \} \mathbf{F}_k^H$  and  $\mathbf{C}_{h_p h_p} = \mathbf{F}_k \mathbf{E} \{ \bar{\mathbf{h}}_k \bar{\mathbf{h}}_k^H \} \mathbf{F}_k^H$  are submatrices of the covariance matrix of the channel frequency response, where  $\bar{\mathbf{h}}_k$  is the  $L \times 1$  vector with the channel

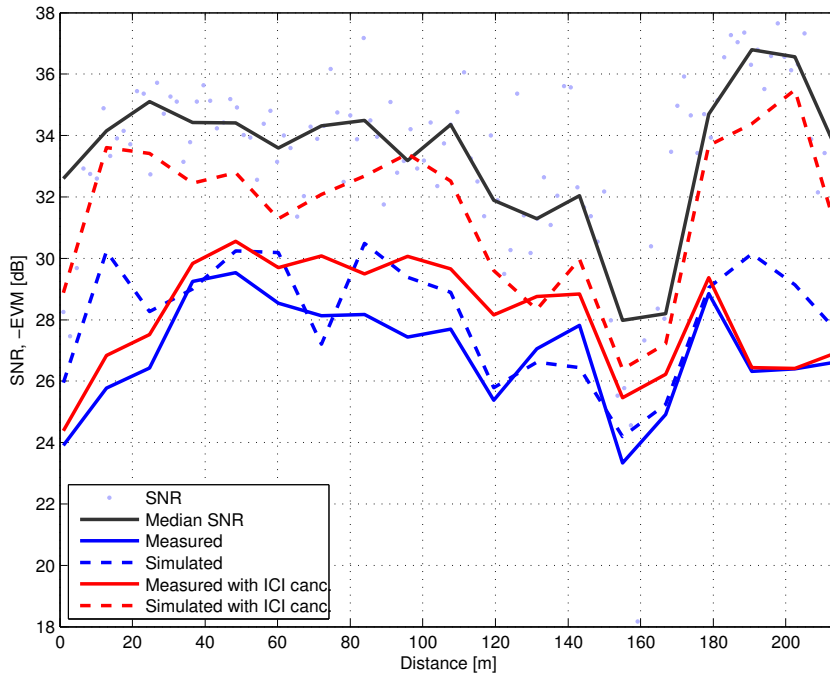


Figure 6.14: EVM and SNR for  $1 \times 1$  and  $v^I = 120$  km/h. The receive antennas are placed outside the car.

impulse response coefficients during the  $k$ -th symbol. The second-order statistics of the impulse response  $E\{\bar{\mathbf{h}}_k \bar{\mathbf{h}}_k^H\}$  are estimated by using all the received pilot subcarriers in a frame, assuming this statistics do not depend on the symbol index  $k$ .

Figures 6.14–6.16 show the EVM and SNR results versus distance for SISO transmissions with outdoor antennas for interpolation factors  $I = 4$ ,  $I = 12$ , and  $I = 20$ , respectively. The car moved at the actual speed of 30 km/h. The previous factors correspond to emulated speeds of 120 km/h, 360 km/h, and 600 km/h, respectively. Figures 6.14, 6.15 and 6.16 clearly show the performance gains obtained when ICI cancellation is performed at reception. The figures also show that comparable gains are obtained with simulation and real measurements, hence validating the performance of the ICI estimation and cancellation techniques utilized. Figure 6.14 shows a constant offset between simulations and measurements. Recall that simulation results were obtained assuming a frequency-flat channel. The soundness of this assumption weakens for low interpolation factors such as  $I = 4$ , so a significant difference between simulation and experimental results is to be expected. Conversely, better agreement between experiments and simulations is observed in Figures 6.15 and 6.16 which correspond to higher interpolation factors ( $I = 12$  and  $I = 20$ , respectively). In such cases, the frequency-flat channel response assumption is tighter.

Figures 6.17–6.19 show the results for the same measurements as before but with the mobile receiver inside the car. The most important difference compared to the previous figures is the

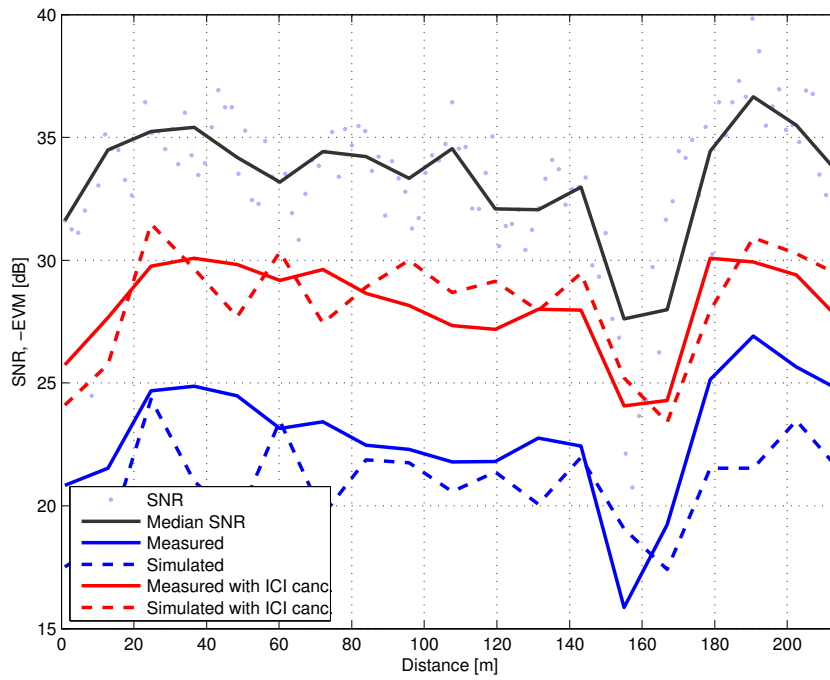


Figure 6.15: EVM and SNR for  $1 \times 1$  and  $v^I = 360$  km/h. The receive antennas are placed outside the car.

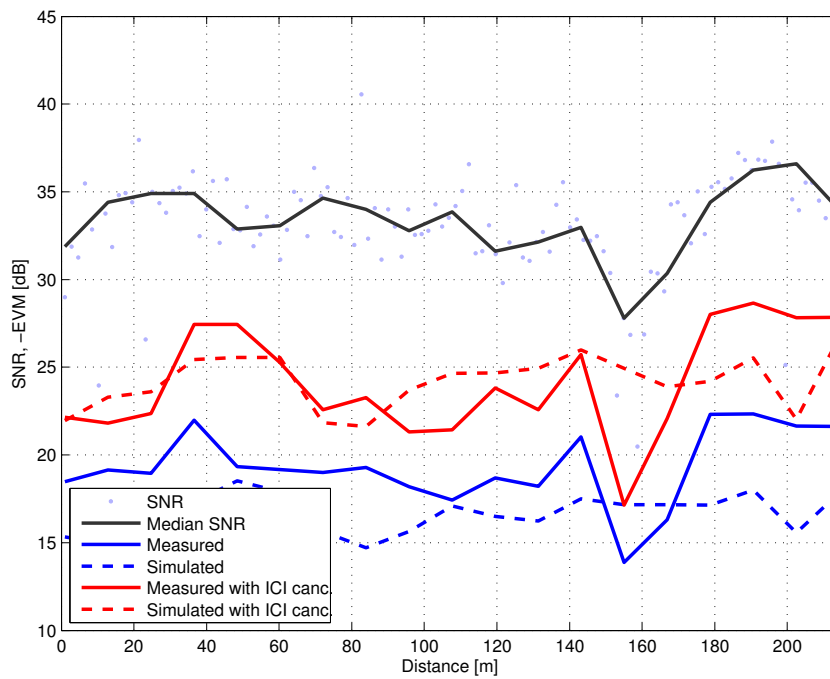


Figure 6.16: EVM and SNR for  $1 \times 1$  and  $v^I = 600$  km/h. The receive antennas are placed outside the car.

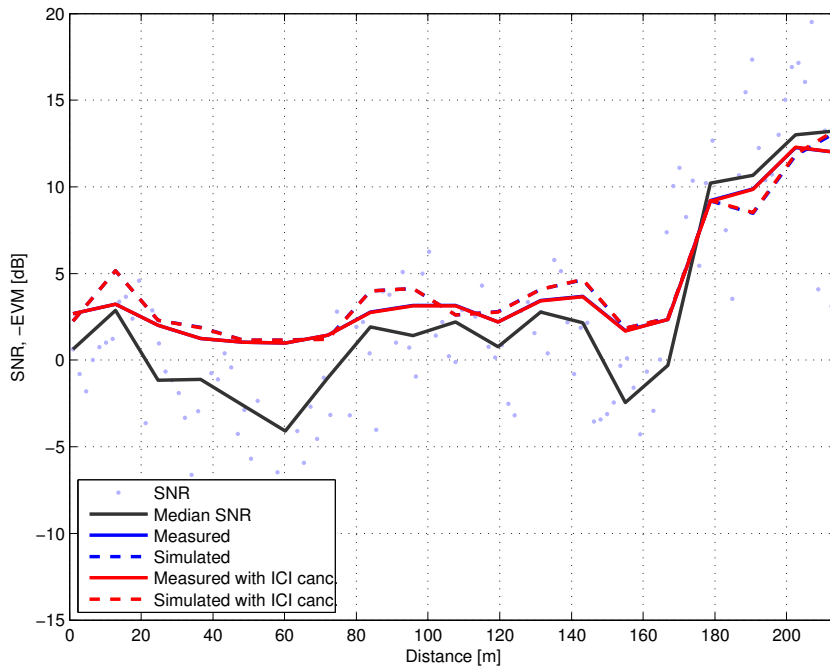


Figure 6.17: EVM and SNR for  $1 \times 1$  and  $v^I = 120$  km/h. The receive antennas are placed inside the car.

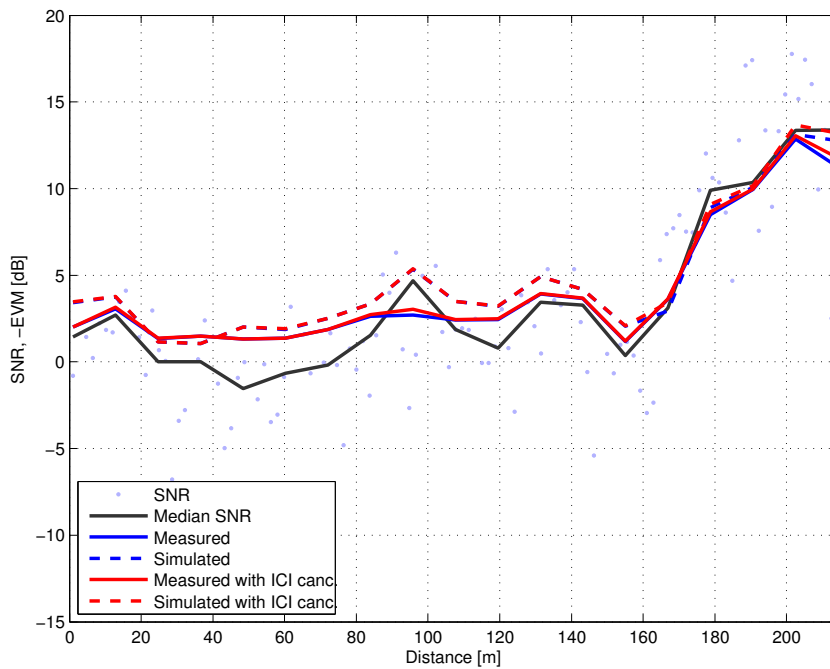


Figure 6.18: EVM and SNR for  $1 \times 1$  and  $v^I = 360$  km/h. The receive antennas are placed inside the car.

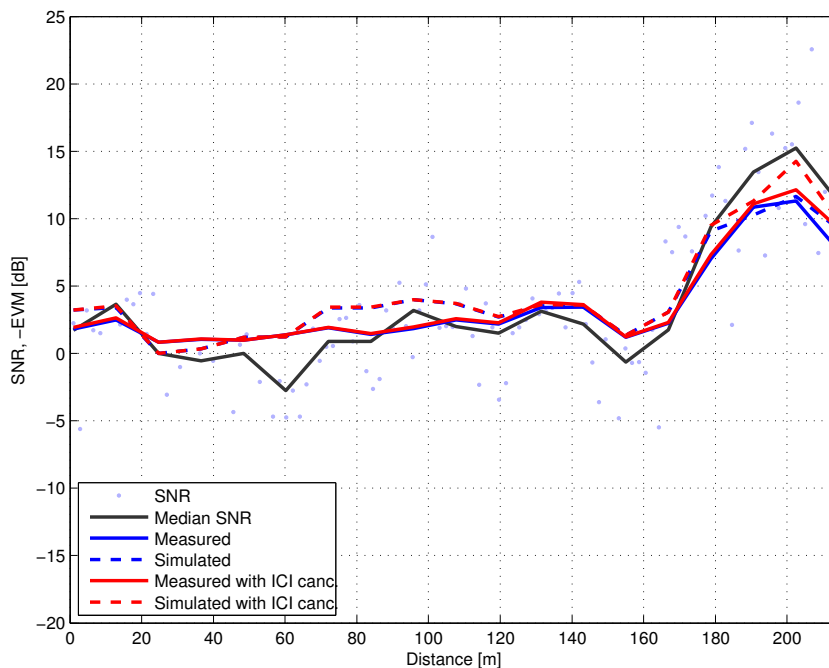


Figure 6.19: EVM and SNR for  $1 \times 1$  and  $v^I = 600$  km/h. The receive antennas are placed inside the car.

lower SNR of this scenario, where median values range between 0 and 10 dB, a large difference compared to the 30 to 35 dB achieved outside due to the strong attenuation introduced by the car structure. As a consequence, negligible performance gains are obtained with receivers that perform ICI cancellation because the noise at the receiver prevails over the interference of the neighbor subcarriers.

Figures 6.20–6.22 show the results corresponding to  $2 \times 2$  MIMO measurements with the receiving antennas placed outside the car for  $I = 4$ ,  $I = 12$ , and  $I = 20$ , respectively. Contrarily to the SISO case, ICI cancellation does not produce significant performance gains when  $I = 4$ . ICI cancellation produces significant performance gains for  $I = 12$  and  $I = 20$ . Again, this is because the received SNR is significantly smaller and the Gaussian noise dominates over the ICI. Also, although spatially uncorrelated channels have been assumed in simulations, the real scenario will show some spatial correlation between antennas (even though cross-polarized transmit antennas are used). Such correlation depends on the distance between antennas, and also on the distance between the transmitter and the receiver, an effect more evident when strong line-of-sight components are present [56]. This spatial correlation introduces interference between antennas, which impairs the gain that could be obtained by the ICI cancellation technique. Finally, notice also that spatial multiplexing is employed in this case, thus pursuing a throughput increase instead of the robustness of the wireless link. This also explains the lower EVM values for the MIMO case compared to those obtained for the

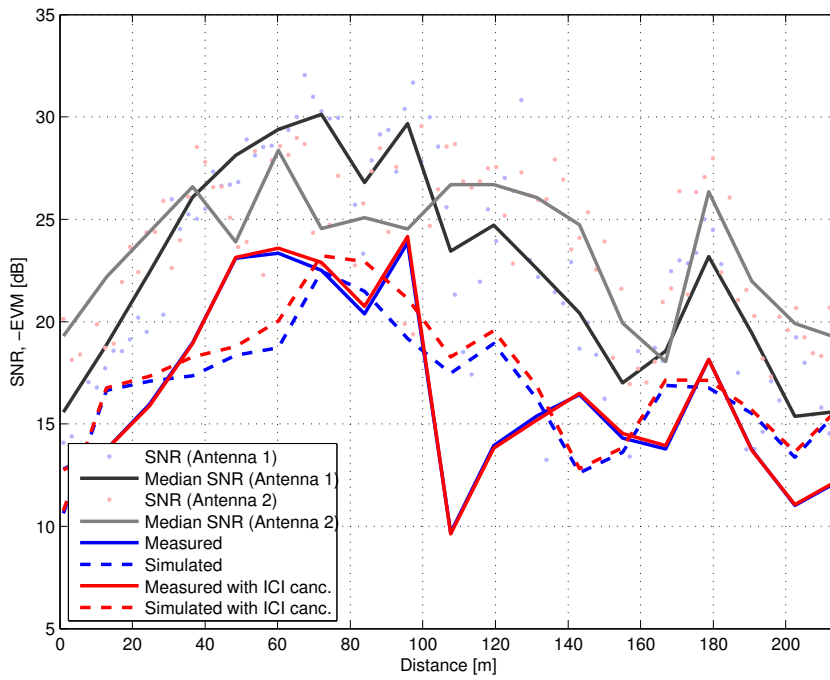


Figure 6.20: EVM and SNR for  $2 \times 2$  and  $v^I = 120$  km/h. The receive antennas are placed outside the car.

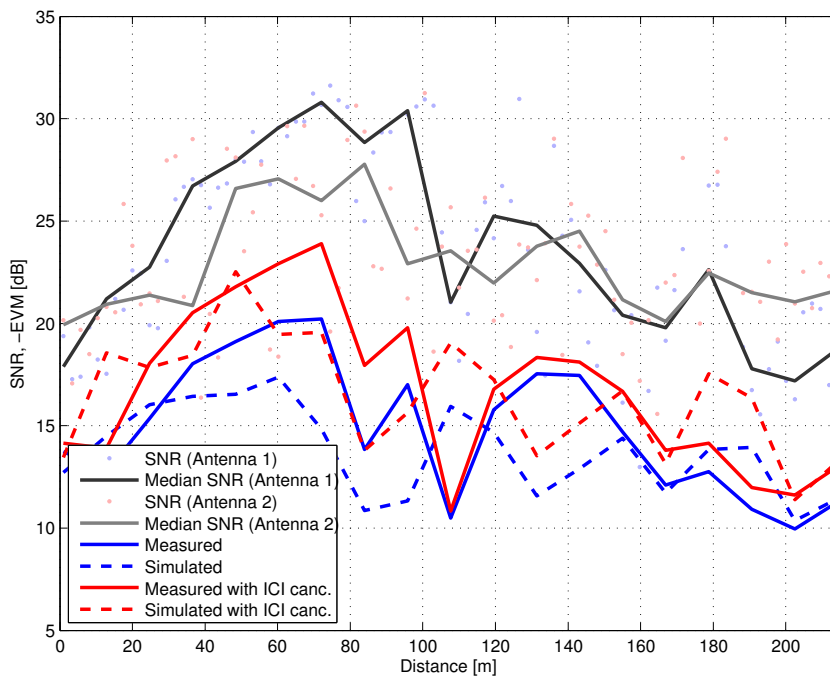


Figure 6.21: EVM and SNR for  $2 \times 2$  and  $v^I = 360$  km/h. The receive antennas are placed outside the car.

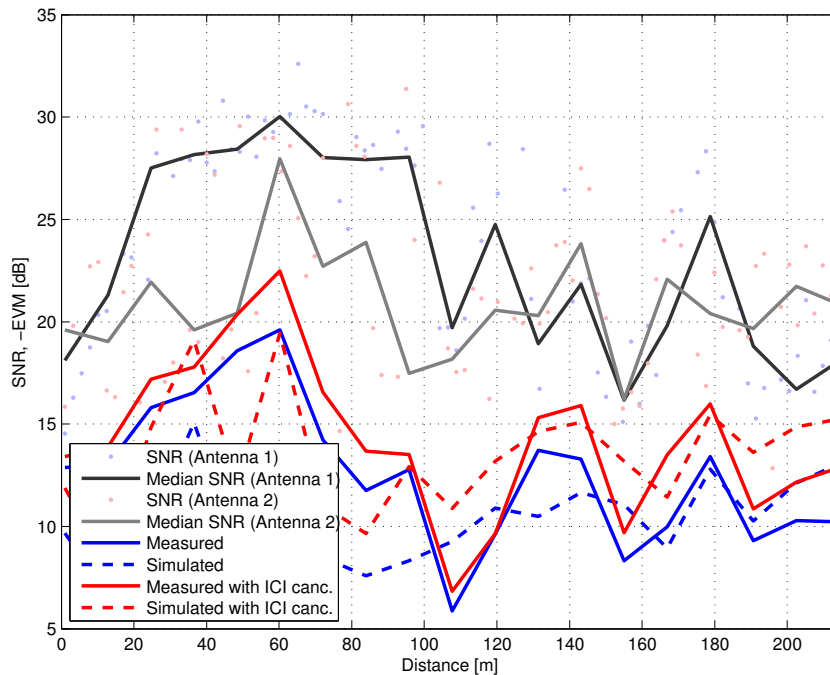


Figure 6.22: EVM and SNR for  $2 \times 2$  and  $v^I = 600$  km/h. The receive antennas are placed outside the car.

single-antenna transmissions.

### 6.4.3 Throughput

In order to evaluate the impact of the ICI cancellation methods on the final user Quality of Experience (QoE), throughput estimations have been carried out using the information conveyed in the bursts. Two types of throughput estimations have been considered. The first one assumes that the transmitter knows, for each frame, the optimal modulation and coding profile to be used. This case was modeled by estimating the BER of the six received bursts per

Profile	-EVM [dB]
4-QAM 1/2	5
4-QAM 3/4	8
16-QAM 1/2	10.5
16-QAM 3/4	14
64-QAM 1/2	16
64-QAM 3/4	20

Table 6.2: EVM to burst-profile mapping for throughput estimations.

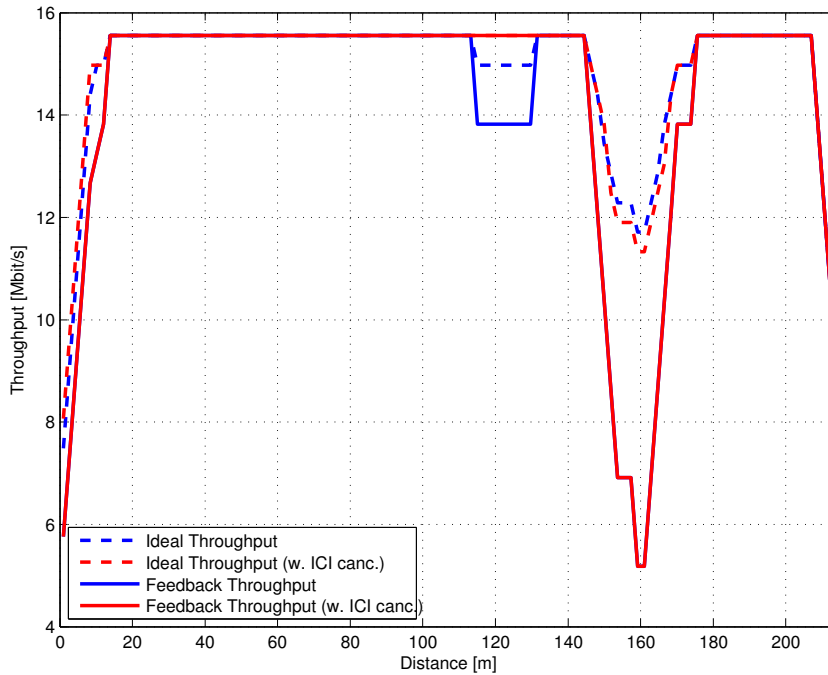


Figure 6.23: Throughput for  $1 \times 1$  and  $v^I = 120$  km/h. The receive antennas are placed outside the car.

frame, and assuming that the whole frame was transmitted with the profile which carries more information bits without suffering any bit error. The second method assumes that the transmitter estimates the most suitable burst profile, and consequently only transmits the corresponding profile during all the bursts. Errors are measured in this case assuming only the burst picked by the transmitter is available, regardless whether this burst has errors or not. This method is intended to determine the impact of the channel fast time-variations on this type of decisions.

To allow the transmitter to take these decisions, a frame by frame EVM metric is obtained in a similar way as the WiMAX standard proposes, i.e.

$$\text{EVM}_F = (1 - \alpha)\text{EVM}_{F-1} + \alpha\text{EVM}_F, \quad (6.6)$$

where  $\alpha$  is a forgetting factor. Along this work we assume  $\alpha = 1/4$ . This EVM value is used to pick a modulation profile and burst according to Table 6.2. Finally, for the sake of clarity, results are shown after applying a moving average to the raw throughput estimates.

Results for the  $1 \times 1$  setup with the antennas placed outside the car are shown in Figures 6.23–6.25 for interpolation factors  $I = 4$ ,  $I = 12$ , and  $I = 20$ , respectively. When  $I = 4$ , the performance gain when using the receiver with ICI cancellation is not significant because the throughput already saturates at the maximum value 15 Mbit/s without canceling the ICI (see Figure 6.23). On the contrary, significant performance gains are obtained for  $I = 12$  and  $I = 20$  when the ICI is canceled. Nevertheless, note the large throughput degradation when the profile is determined from delayed EVM measurements rather than from the actual

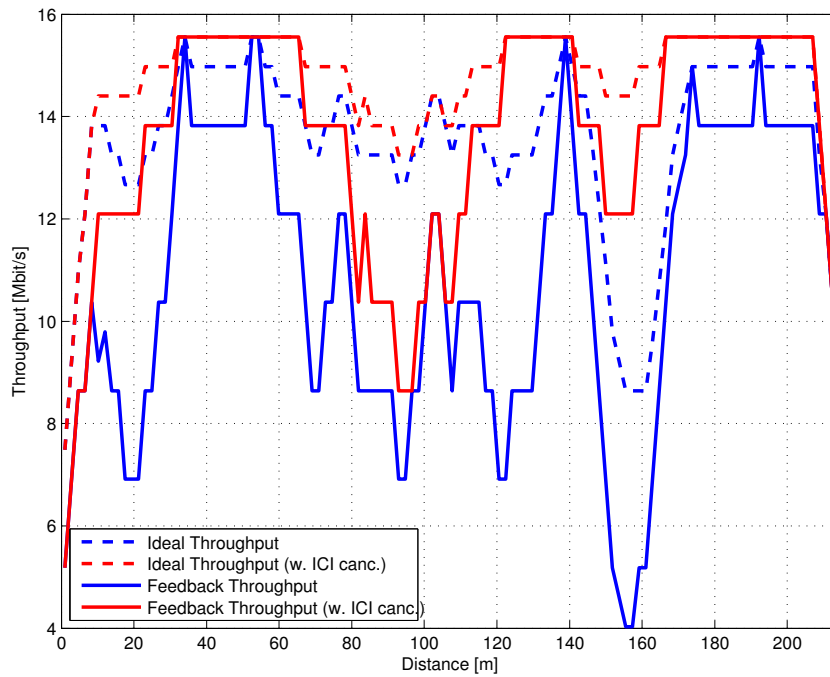


Figure 6.24: Throughput for  $1 \times 1$  and  $v^I = 360$  km/h. The receive antennas are placed outside the car.

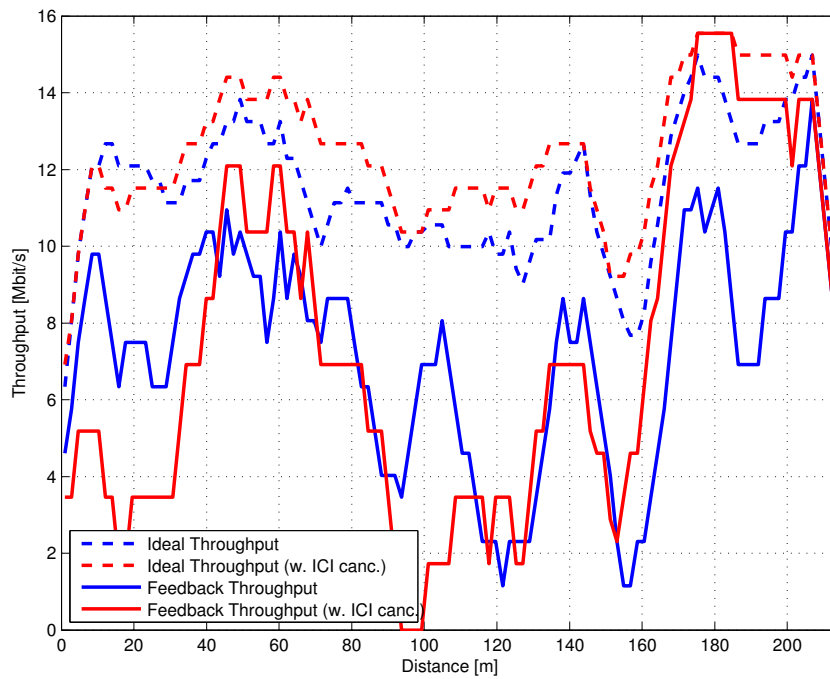


Figure 6.25: Throughput for  $1 \times 1$  and  $v^I = 600$  km/h. The receive antennas are placed outside the car.

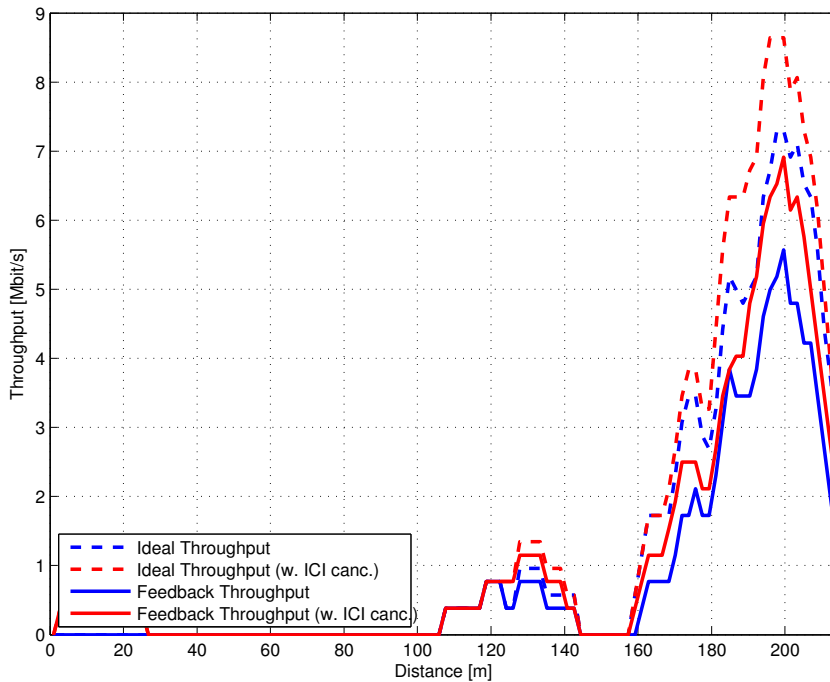


Figure 6.26: Throughput for  $1 \times 1$  and  $v^I = 120$  km/h. The receive antennas are placed inside the car.

ones. In channels with low coherence times, estimations of the EVM according to (6.6) are less reliable, thus increasing the probability of picking up an incorrect burst profile. This effect is more evident for the highest interpolation factor  $I = 20$ , where at some time instants even the ICI-canceled signal provides the lowest throughput.

Figures 6.26–6.28 show the results for the same measurement campaign as before but with the antennas placed inside the car. The most important effect is that the SNR is now much lower and the receiver is unable to detect any burst without errors during the first part of the measurement trajectory. The larger SNRs observed in the last sector of the measurement course allow for correctly decoding information bits, but leading to throughput values far from those observed from the antennas placed outside the car. Also, the throughput gains obtained after ICI cancellation are quite low.

Corresponding results for the  $2 \times 2$  MIMO setup are shown in Figures 6.29–6.31. The first evident feature is the larger achievable throughput, since two streams are being transmitted in each frame. As with EVM, low gains when  $I = 4$  are appreciated, but peak gains of 2 Mbit/s are observed when  $I = 12$  and  $I = 20$ .

A more meaningful way to represent the mean throughput values obtained during all measurement campaigns is the one shown in Tables 6.3 to 6.5. These averaged throughputs were obtained from the four runs over the course completed for the measurements. These throughput values show that, in general, some gain is obtained by using receivers that cancel the ICI, and how the throughput worsens with the interpolation factor. It is also important to

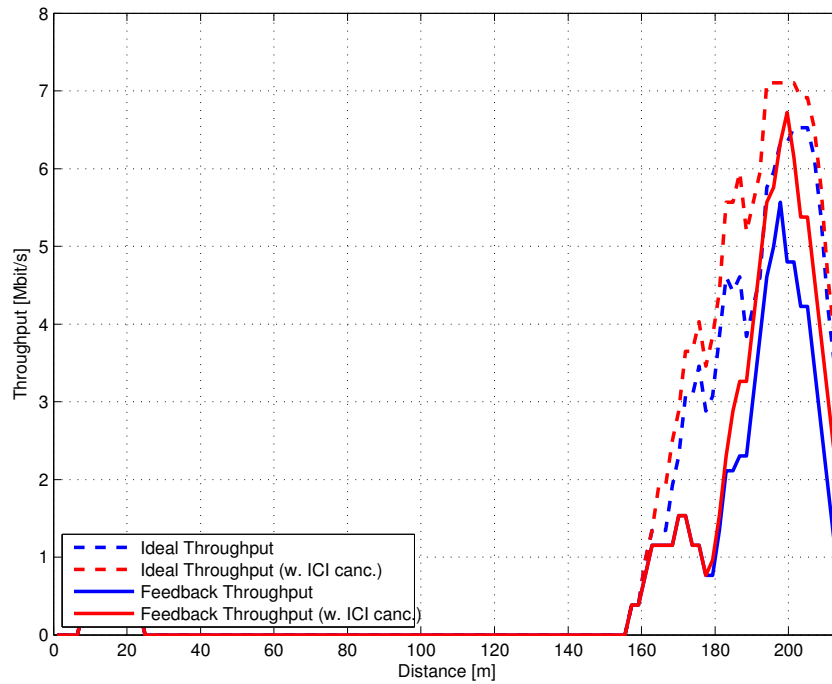


Figure 6.27: Throughput for  $1 \times 1$  and  $v^I = 360$  km/h. The receive antennas are placed inside the car.

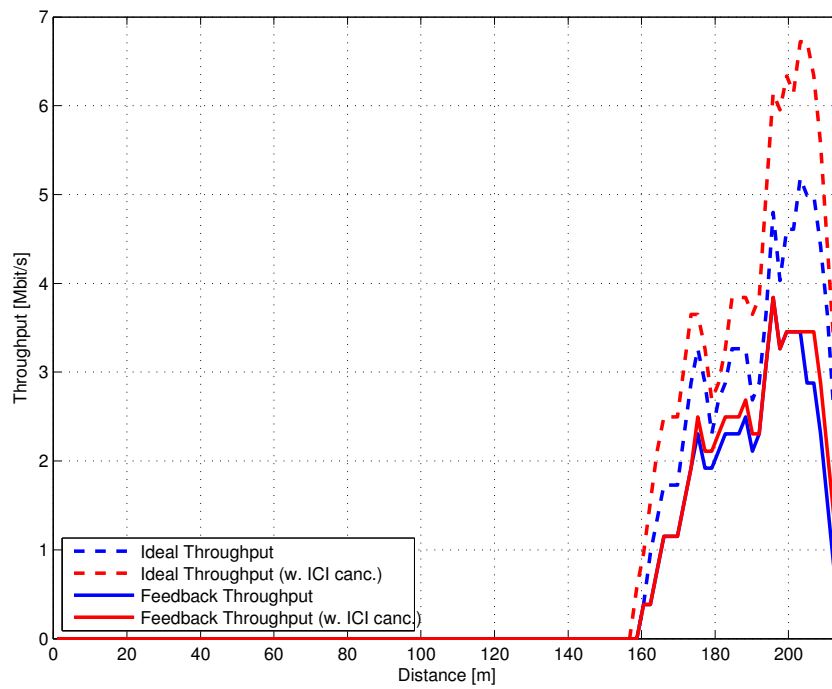


Figure 6.28: Throughput for  $1 \times 1$  and  $v^I = 600$  km/h. The receive antennas are placed inside the car.

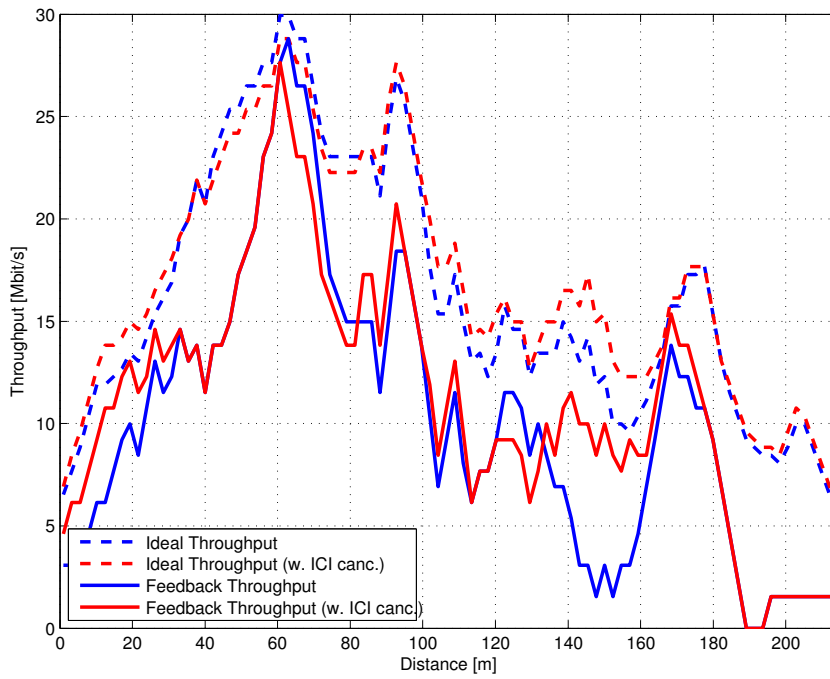


Figure 6.29: Throughput for  $2 \times 2$  and  $v^I = 120$  km/h. The receive antennas are placed outside the car.

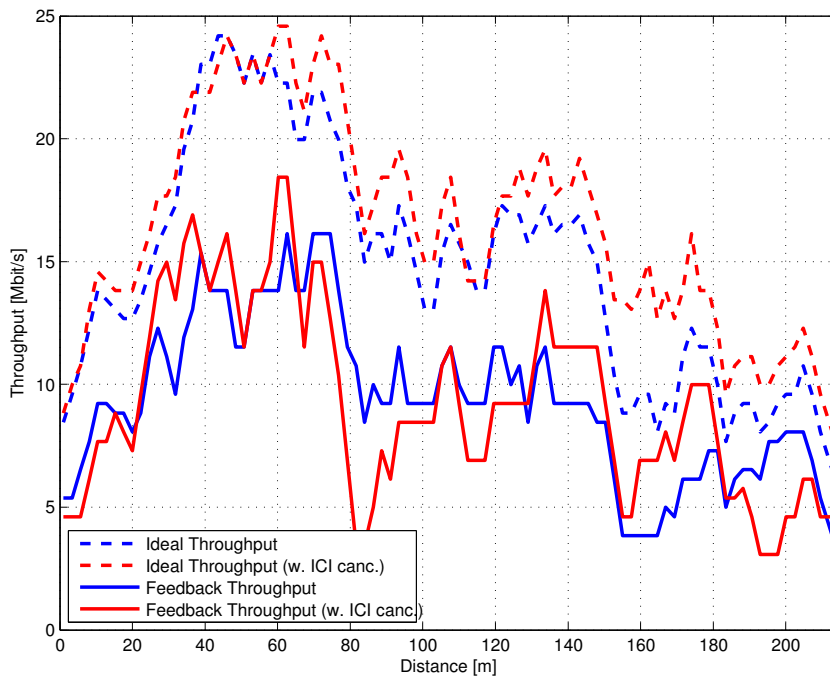


Figure 6.30: Throughput for  $2 \times 2$  and  $v^I = 360$  km/h. The receive antennas are placed outside the car.

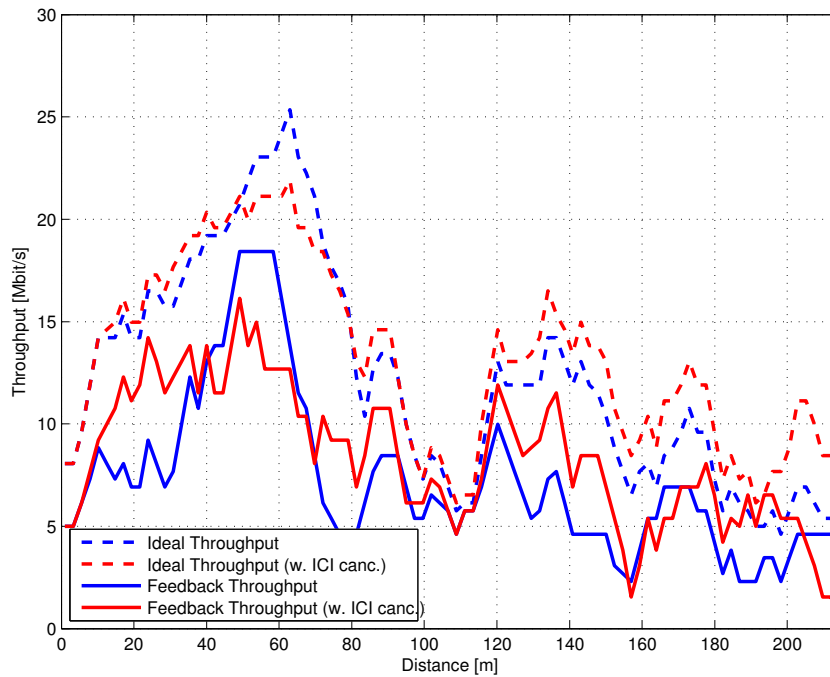


Figure 6.31: Throughput for  $2 \times 2$  and  $v^I = 600$  km/h. The receive antennas are placed outside the car.

	ideal throughput	ideal throughput (with ICI cancellation)	feedback throughput	feedback throughput (with ICI cancellation)
$I = 4$	14.32	14.73	13.01	13.93
$I = 12$	12.22	13.78	8.81	11.39
$I = 20$	9.76	11.37	5.48	6.51

Table 6.3: Mean throughput in Mbit/s for the  $1 \times 1$  scenario when the receive antennas are placed outside the car.

	ideal throughput	ideal throughput (with ICI cancellation)	feedback throughput	feedback throughput (with ICI cancellation)
$I = 4$	3.15	3.48	2.11	2.45
$I = 12$	2.90	3.26	1.96	2.23
$I = 20$	2.67	3.03	1.82	1.97

Table 6.4: Mean throughput in Mbit/s for the  $1 \times 1$  scenario when the receive antenna is placed inside the car.

	ideal throughput	ideal throughput (with ICI cancellation)	feedback throughput	feedback throughput (with ICI cancellation)
$I = 4$	16.95	17.46	10.56	10.99
$I = 12$	15.74	17.48	9.20	11.01
$I = 20$	12.61	13.99	7.49	8.87

Table 6.5: Mean throughput in Mbit/s for the  $2 \times 2$  scenario when the receive antennas are placed outside the car.

note that in some scenarios at low emulated speeds, negligible gains, or even less performance, is obtained with these methods. In general, a remarkable difference is observed between the ideal throughput and the realistic measure which considers the EVM metric to pick the burst profile. This is due to the inability of the EVM estimator to track the fast time-variations of the channel. Also, even though in the previous figures at some instants the ICI-canceled throughput was lower, it can be seen that in average the ICI cancellation techniques provide a better performance. Finally, in the case of MIMO  $2 \times 2$  (dual stream transmission), although almost no difference in terms of EVM is appreciated when  $I = 4$ , an average gain of approximately 0.50 Mbit/s has been obtained in terms of throughput. When  $I = 12$  and  $I = 20$  the average gains grow up to 1.8 Mbit/s and 1.4 Mbit/s approximately.

An apparent conclusion of this behavior, is that a burst selection algorithm based on the EVM can turn out to be unreliable in the short term, given the fast variations of the channel. Also, ICI cancellation algorithms can improve EVM without necessarily being sufficient to produce a change to a burst profile that supports a larger throughput. Therefore, a more interesting figure of merit could be the Packet Error Rate (PER) at MAC level. A more appropriate scheme could be evaluated based on picking a profile considering the PER. This result also suggests that picking a wrong burst profile can degrade more the throughput than making a conservative assumption about the quality of the channel. This could be critical under some applications, such as train control and signaling systems, where a loss of the connectivity during a long time period could lead to an emergency train stop for security reasons. Nevertheless, on average terms, throughput gains are observed after ICI cancellation, thus these observations would apply when it is more important to guarantee a minimum quality of the connectivity, rather than a higher average throughput performance.

## 6.5 Conclusions

In this chapter, evaluations of the performance of the WiMAX downlink physical layer in high-mobility scenarios have been done. Both SISO and MIMO transmissions (dual stream with

two transmit antennas) were considered, as well as placing the receive antennas outside and inside the car used for the experiments, thus assessing the outdoor-to-outdoor and the outdoor-to-indoor channels, respectively. We focused on the ICI caused by channel time-variations in such scenarios. Cost-effective measurement campaigns were carried out where high-mobility scenarios are emulated with a vehicle moving at a low speed. The key idea is the enlargement of the symbol period prior to its transmission over the air. Such enlargement reduces the frequency spacing between the OFDM subcarriers in WiMAX transmissions and hence induces high ICI values on the received signals. Experiments illustrate the performance of WiMAX receivers with and without ICI cancellation in terms of EVM and throughput. ICI cancellation produces significant performance gains mainly when the received SNR is high. Otherwise, thermal noise dominates over the ICI and gains are not so much appreciated. Furthermore, the spacing of subcarriers in this standard is sufficient to provide a robust behavior for moderate mobility environments, and the gain observed after ICI cancellation is not very significant for speeds up to 80 km/h. Note that the profile tested in this work is the WiMAX profile with the lowest subcarrier spacing, so it is foreseeable that other profiles present better performance under these scenarios.



---

# Chapter 7

## Conclusions and Future Work

The aim of this work is twofold. On the one hand, it introduces a Software Defined Radio (SDR) architecture for the implementation of an Orthogonal Frequency Division Multiplexing (OFDM)-based Physical layer (PHY), using reconfigurable hardware. On the other hand, it analyzes, and also experimentally evaluates, the effects of high mobility conditions on the OFDM signal, as well as the evaluation of techniques to mitigate Inter-Carrier Interference (ICI) caused by such high mobility conditions.

Chapter 1 shows an overview of the OFDM waveform. In particular, the effects of the synchronization errors and the channel time-variations on the received signal are studied. One of the first advantages of OFDM is its resilience to timing offsets which translates into a subcarrier-dependent constant phase shift, assimilated as part of the channel estimation process. However, this is not true for fractional frequency carrier offsets and channel time variations, being both phenomena a source of ICI. Also, when the model is extended to the Multiple-Input Multiple-Output (MIMO) setup, the spatial interference between transmit antennas also increases the impact on the ICI, thus demanding for specific estimation and equalization techniques for its mitigation. Finally, the physical layers of Mobile WiMAX and Advanced WiMAX are described, as examples of OFDM-based physical layers.

In Chapter 3, a SDR architecture for the implementation of OFDM-based systems is shown, and an example of its application to the downlink of Mobile WiMAX is also described. This architecture includes channel coding of data bursts, burst mapping to the WiMAX subframe, and preamble and pilot insertion according to the standard. The architecture was put into practice with the help of Field Programmable Gate Arrays (FPGAs) and Digital Signal Processors (DSPs). Also, the algorithms used in the receiver are described without taking into account the mobility of the channel.

The resulting implementation is evaluated under static and mobile scenarios with the help of a channel emulator, and the results are in Chapter 4. With these results, the effects of ICI on the OFDM signal could be observed, since the receiver is not prepared to deal with this kind of

interference.

On the other hand, ICI estimation and cancellation techniques are studied in Chapter 5. Optimal Basis Expansion Model (BEM) designs are defined for an estimation strategy which uses the frequency response estimations of consecutive OFDM symbols to obtain the ICI. BEMs for spatially uncorrelated and correlated MIMO channels are derived and results of their behavior are studied by simulations under an asymmetrical Jakes spectrum model. The obtained results show that these BEMs allow receivers to achieve better performance as long as such receivers know perfectly the second order statistics of the channel in the time domain.

In Chapter 6, the experimental evaluation of these algorithms, instead of a channel emulator, is based on a testbed –using Ettus USRP B210 nodes and the Ettus UHD software–, and on the introduction of the Doppler spreads by extending the symbol period of the OFDM symbols. The signals transmitted are based on Mobile WiMAX, and a software implementation of the algorithms used in the real-time architecture described in Chapter 3 is used. The measurements were carried out with a car in which the testbed equipment was deployed. The first results obtained allows us to validate the behavior of the ICI estimation algorithms under time-varying conditions. The performance of the KL-BEM is assessed assuming that the channel follows a Jakes model, but marginal gains are obtained for larger BEM orders. Also, a large gain difference is observed when comparing the results corresponding to the antennas located inside and outside the car, which is due to the shielding of the car, as well as the angle of arrival of the signals impinging the car structure.

Finally, throughput estimations are also made using a burst profile selection criteria based on the Error Vector Magnitude (EVM) of the received signals. In this case, although the EVM values are always better for the signals after the ICI cancellation, this does not necessarily translate into higher (or even sufficient) throughput values at every time instant. On average, throughput improves thanks to the use of ICI cancellation, but the fast variations of the channel lead to a performance degradation in the short term. More conservative approaches of burst profile selection, or criteria based on Packet Error Rate can be applied in order to keep a minimum link quality level instead of maximizing the average throughput.

### 7.1 Future Work

The topics discussed in this work are very broad: hardware architectures for multicarrier systems, signal processing algorithms designed to estimate the ICI under doubly-selective channels, and the evaluation of these systems under mobility scenarios. Any of these aspects can be further investigated, and the following points are of special interest.

### 7.1.1 ICI estimation on the Hardware Platform

The ICI estimation algorithms described in this work have the advantage of being possible to easily extend systems which already obtain channel estimations to perform equalization. An additional stage which relies on channel frequency response estimations can be included to obtain the coefficients describing the ICI.

The architecture shown for OFDM downlink systems has been put into practice with channel estimation and equalization techniques which ignored ICI. This architecture can be extended to incorporate these ICI estimation algorithms. Furthermore, as shown in the results section, it is possible to obtain a good performance using as an initial frequency response algorithm a pilot-based LS with linear interpolation, which is the technique currently employed in the hardware platform. However, ICI equalization is still a computationally demanding process since it requires the computation of matrix inversions or a search on the space of the transmitted symbols, and efficient ICI cancellation algorithms are of special interest for their implementation in dedicated hardware.

### 7.1.2 Channel Characterization

In Chapter 5 estimation techniques relying on the temporal and spatial second-order statistics of the channel are described. However, results of real-world measurements of these algorithms have not been presented, since a full characterization of the channel in the measurement scenarios has not been done. This characterization could require the definition of special waveforms, given that with a general-purpose multicarrier modulation some of the information required about these statistics could be lost, since for each subcarrier a single coefficient of the channel is obtained for all the duration of an OFDM symbol, as discussed in Chapter 5.

Regarding the evaluation, it would be interesting to investigate if the theoretical gains observed in simulations translate into the real-world measurements compared with more general BEMs, such as the DPS-BEM, and assessing if the additional complexity implied by the characterization of the channel has a meaningful impact on the performance of a receiver. Also, spatial correlation could be characterized to obtain better estimates of the channel in the MIMO scenarios. Some theoretical works have pointed out that channel capacity increases with spatial correlation at lower SNRs under some circumstances [24, 90], which could be experimentally evaluated.

### 7.1.3 Uplink Evaluation and beyond OFDM

Uplink transmissions in OFDM-based physical layers is usually done by allocating different sets of subcarriers to each user. If one of the users is under mobility conditions, it can interfere

in the users transmitting on adjacent subcarriers. Evaluations of the impact of this distortion, and of specific ICI estimation algorithms for the uplink setup can be addressed.

Practical comparisons with other physical layers such as that of LTE can be done with the help of testbeds, where the effects of different pilot pattern allocation strategies in the downlink and in the uplink can have a critical impact under mobility conditions. Another particular feature of LTE is the use of Single-Carrier Frequency Domain Equalization (SC-FDE), in which the users transmit in single carrier with pilots transmitted in the frequency domain at regular intervals. It could be evaluated if the theoretical robustness of SC-FDE against time-varying channels is impaired by the reduced number of pilots allocated, when compared to OFDM.

Finally, different multicarrier systems are being studied as possible replacements for OFDM in the next generation of communication standards, which feature a higher spectral efficiency and robustness against the interference produced by the wireless channel. Some examples of the most promising waveforms are Filter Bank Multicarrier (FBMC), Generalized OFDM (G-OFDM) and Universal Filtered Multicarrier (UFMC), each one with its own advantages and drawbacks. Specific ICI estimation and cancellation algorithms for these transmissions schemes can be designed, besides the evaluation of the performance of these techniques in mobility environments when compared with OFDM.

# Bibliography

- [1] "IEEE Standard for WirelessMAN-Advanced Air Interface for Broadband Wireless Access Systems," *IEEE Std 802.16.1-2012*, 2012.
- [2] "IEEE Standard for Air Interface for Broadband Wireless Access Systems," *IEEE Std 802.16-2012 (Revision of IEEE Std 802.16-2009)*, 2012.
- [3] "Analog devices AD9361 RFIC." URL: <http://www.analog.com/en/rfif-components/rfif-transceivers/ad9361/products/product.html>
- [4] "Anritsu Fading Simulator MF6900A." URL: <http://www.anritsu.com/en-US/Products-Solutions/Products/MF6900A.aspx>
- [5] "Interline sector is-g14-f2425-a120-v vertically polarized antenna." URL: <http://interline.pl/antennas/SECTOR-V120-14dBi-120deg-2.4-2.5GHz>
- [6] "Mini-circuits high-power amplifier TVA-11-422." URL: <http://www.minicircuits.com/pdfs/TVA-11-422.pdf>
- [7] "R&S ABFS Baseband Fading Simulator." URL: [http://www.rohde-schwarz.com/en/product/abfs-productstartpage\\_63493-7576.html](http://www.rohde-schwarz.com/en/product/abfs-productstartpage_63493-7576.html)
- [8] "TMS320C6414, TMS320C6415, TMS320C6416 Fixed-Point Digital Signal Processors."
- [9] "Ettus USRP B210." URL: <https://www.ettus.com/product/details/UB210-KIT>
- [10] "Ubiquity am-2g15-120 cross polarized antenna." URL: [http://dl.ubnt.com/datasheets/airmaxsector/airMAX\\_Sector\\_Antennas\\_DS.pdf](http://dl.ubnt.com/datasheets/airmaxsector/airMAX_Sector_Antennas_DS.pdf)
- [11] "Virtex-4 Family Overview."
- [12] "Xilinx Virtex-II Series FPGAs."
- [13] *COST 207 Digital Land Mobile Radio Communications*. Office for Official Publications of the European Communities, 1989.
- [14] "OFDMA PHY SAP Interface Specification for 802.16 Broadband Wireless Access Base Stations," Intel Corporation, Tech. Rep., 2007.
- [15] "Recommendation ITU-R M.1225: Guidelines for Evaluation of Radio Transmission Technologies for IMT-2000," ITU-R, Tech. Rep., 1997.
- [16] "Wimax forum." URL: <http://www.wimaxforum.org>
- [17] "Requirements and Recommendations for WiMAX Forum™ Mobility Profiles," WiMAX Forum™, Tech. Rep., 2005.

- [18] N. Al-Dhahir and A. Sayed, "The finite-length multi-input multi-output MMSE-DFE," *IEEE Transactions on Signal Processing*, vol. 48, no. 10, pp. 2921–2936, Oct 2000, doi:10.1109/78.869048.
- [19] A. Burg and M. Rupp, *EURASIP Book on Smart Antennas*. EURASIP, 2006, ch. Demonstrators and Testbeds.
- [20] B. B. C., R. Kunst, and F. Henes, "Channel Encoding Block for Mobile WiMAX Networks Using Reconfigurable Hardware," *Journal of Applied Computing Research*, vol. 1, no. 2, pp. 69–75, July–December 2011, doi:10.4013/jacr.2011.12.01.
- [21] X. Cai and G. Giannakis, "Bounding performance and suppressing intercarrier interference in wireless mobile OFDM," *IEEE Transactions on Communications*, vol. 51, no. 12, pp. 2047–2056, Dec 2003, doi:10.1109/TCOMM.2003.820752.
- [22] A. Carro-Lagoa, P. Suárez-Casal, J. A. García-Naya, P. Fraga-Lamas, L. Castedo, and A. Morales-Méndez, "Design and implementation of an OFDMA-TDD physical layer for WiMAX applications," *EURASIP Journal on Wireless Communications and Networking*, vol. 2013, no. 1, p. 243, 2013, doi:10.1186/1687-1499-2013-243.
- [23] K.-C. Chang, J.-W. Lin, and T.-D. Chiueh, "Design of a downlink baseband receiver for IEEE 802.16E OFDMA mode in high mobility," in *IEEE International SOC Conference, 2007*, September 2007, pp. 301–304, doi:10.1109/SOCC.2007.4545479.
- [24] C.-N. Chuah, D. Tse, J. Kahn, and R. Valenzuela, "Capacity scaling in MIMO wireless systems under correlated fading," *IEEE Transactions on Information Theory*, vol. 48, no. 3, pp. 637–650, Mar 2002, doi:10.1109/18.985982.
- [25] G. Chuang, P.-A. Ting, J.-Y. Hsu, J.-Y. Lai, S.-C. Lo, Y.-C. Hsiao, and T.-D. Chiueh, "A MIMO WiMAX SoC in 90nm CMOS for 300km/h mobility," in *IEEE International Solid-State Circuits Conference Digest of Technical Papers (ISSCC), 2011*, Feb. 2011, pp. 134–136, doi:10.1109/ISSCC.2011.5746252.
- [26] J. Cioffi and J. Forney, G.D., "Generalized Decision-Feedback Equalization for Packet Transmission with ISI and Gaussian Noise," in *Communications, Computation, Control, and Signal Processing*, A. Paulraj, V. Roychowdhury, and C. Schaper, Eds. Springer US, 1997, pp. 79–127. URL: [http://dx.doi.org/10.1007/978-1-4615-6281-8\\_4](http://dx.doi.org/10.1007/978-1-4615-6281-8_4)
- [27] R. Clarke, "A statistical theory of mobile-radio reception," *The Bell System Technical Journal*, vol. 47, no. 6, pp. 957–1000, July 1968, doi:10.1002/j.1538-7305.1968.tb00069.x.
- [28] R. Colda, T. Palade, E. Pucchita, I. Vermecan, and A. Moldovan, "Mobile WiMAX: System performance on a vehicular multipath channel," in *Proceedings of the Fourth European Conference on Antennas and Propagation (EuCAP), 2010*, April 2010, pp. 1–5.
- [29] R. Cox and C. Sundberg, "An efficient adaptive circular Viterbi algorithm for decoding generalized tailbiting convolutional codes," *IEEE Transactions on Vehicular Technology*, vol. 43, no. 1, pp. 57–68, Feb. 1994, doi:10.1109/25.282266.
- [30] O. Edfors, M. Sandell, J.-J. van de Beek, S. Wilson, and P. Ola Borjesson, "OFDM channel

- estimation by singular value decomposition,” in *IEEE 46th Vehicular Technology Conference, 1996. Mobile Technology for the Human Race.*, vol. 2, Apr-1 May. 1996, pp. 923 –927 vol.2, doi:10.1109/VETEC.1996.501446.
- [31] B. Efron and D. V. Hinkley, *An Introduction to the Bootstrap (CRC Monographs on Statistics & Applied Probability)*, 1st ed. Chapman & Hall, 1994. ISBN: 0412042312.
- [32] T. Fernandez-Carames, M. Gonzalez-Lopez, and L. Castedo, “FPGA-based vehicular channel emulator for evaluation of IEEE 802.11p transceivers,” in *9th International Conference on Intelligent Transport Systems Telecommunications,(ITST),2009*, Oct 2009, pp. 592–597, doi:10.1109/ITST.2009.5399287.
- [33] O. Font-Bach, N. Bartzoudis, A. Pascual-Iserte, and D. L. Bueno, “A real-time MIMO-OFDM mobile WiMAX receiver: Architecture, design and FPGA implementation,” *Computer Networks*, vol. 55, no. 16, pp. 3634 – 3647, 2011, doi:10.1016/j.comnet.2011.02.018.
- [34] “Viterbi Decoder Block Decoding - Trellis Termination and Tail Biting,” Xilinx. URL: [http://www.xilinx.com/support/documentation/application\\_notes/xapp551.pdf](http://www.xilinx.com/support/documentation/application_notes/xapp551.pdf)
- [35] G. Giannakis and C. Tepedelenlioglu, “Basis expansion models and diversity techniques for blind identification and equalization of time-varying channels,” *Proceedings of the IEEE*, vol. 86, no. 10, pp. 1969 –1986, Oct. 1998, doi:10.1109/5.720248.
- [36] E. Haas, “Aeronautical channel modeling,” *IEEE Transactions on Vehicular Technology*, vol. 51, no. 2, pp. 254 –264, Mar. 2002, doi:10.1109/25.994803.
- [37] H. Hijazi and L. Ros, “Polynomial Estimation of Time-Varying Multipath Gains With Intercarrier Interference Mitigation in OFDM Systems,” *IEEE Transactions on Vehicular Technology*, vol. 58, no. 1, pp. 140 –151, Jan. 2009, doi:10.1109/TVT.2008.923653.
- [38] H. Hijazi, L. Ros, and G. Jourdain, “OFDM Channel Parameters Estimation used for ICI Reduction in time-varying Multipath Channels,” in *Proceedings European Wireless Conference*, Apr. 2007.
- [39] F. Hlawatsch and G. Matz, *Wireless Communications over Rapidly Time-Varying Channels*, Elsevier, Ed. Academic Press, 2011.
- [40] C. Hsiao, C.-Y. Chen, and T.-D. Chiueh, “Design of a dual-mode baseband receiver for 802.11n and 802.16e MIMO OFDM/OFDMA,” in *International Symposium on VLSI Design, Automation and Test, 2009. VLSI-DAT '09.*, April 2009, pp. 331 –334, doi:10.1109/VDAT.2009.5158162.
- [41] J.-Y. Hsu, C.-Y. Kao, P.-H. Kuo, and P. Ting, “Configurable baseband designs and implementations of WiMAX/LTE dual systems based on multi-core DSP,” in *IEEE International SOC Conference (SOCC), 2011*, September 2011, pp. 265 –271, doi:10.1109/SOCC.2011.6085146.
- [42] S. Hu, G. Wu, Y. L. Guan, C. L. Law, Y. Yan, and S. Li, “Development and performance evaluation of mobile WiMAX testbed,” in *IEEE Mobile WiMAX Symposium, 2007.*, March 2007, pp. 104 –107, doi:10.1109/WIMAX.2007.348688.
- [43] IEEE, “IEEE Standard for Local and metropolitan area networks Part 16: Air Interface for Broadband Wireless Access Systems,” *IEEE Std 802.16-2009 (Revision of IEEE Std 802.16-2004)*, pp. 1 –2080, 29 2009, doi:10.1109/IEEESTD.2009.5062485.

- [44] —, “IEEE Standard for Local and metropolitan area networks Part 16: Air Interface for Broadband Wireless Access Systems Amendment 3: Advanced Air Interface,” *IEEE Std 802.16m-2011(Amendment to IEEE Std 802.16-2009)*, 2011, doi:10.1109/IEEESTD.2011.5765736.
- [45] —, “IEEE Standard for Local and metropolitan area networks Part 16: Air Interface for Broadband Wireless Access Systems,” *IEEE Std. 802.16-2004*, 2004.
- [46] P. Imperatore, E. Salvadori, and I. Chlamtac, “Path Loss Measurements at 3.5 GHz: A Trial Test WiMAX Based in Rural Environment,” in *3rd International Conference on Testbeds and Research Infrastructure for the Development of Networks and Communities, 2007. TridentCom 2007*, May 2007, pp. 1–8, doi:10.1109/TRIDENTCOM.2007.4444709.
- [47] W. Jakes, *Microwave mobile communications*, ser. IEEE Press classic reissue. Wiley, 1974.
- [48] W. G. Jeon, K. H. Chang, and Y. S. Cho, “An equalization technique for orthogonal frequency-division multiplexing systems in time-variant multipath channels,” *IEEE Transactions on Communications*, vol. 47, no. 1, pp. 27–32, Jan. 1999, doi:10.1109/26.747810.
- [49] H. Kang, S.-B. Im, H.-J. Choi, and D.-J. Rhee, “Robust OFDMA Frame Synchronization Algorithm on Inter-Cell Interference,” in *Asia-Pacific Conference on Communications, 2006. APCC '06.*, 31 2006-sept. 1 2006, pp. 1–5, doi:10.1109/APCC.2006.255832.
- [50] M. Katz and F. H. Fitzek, *WiMAX evolution: emerging technologies and applications*. John Wiley & Sons, 2009.
- [51] S. M. Kay, *Fundamentals of Statistical Signal Processing*. Prentice Hall, 1993.
- [52] M. Khairy, M. Abdallah, and S.-D. Habib, “Efficient FPGA Implementation of MIMO Decoder for Mobile WiMAX System,” in *IEEE International Conference on Communications, 2009. ICC '09*, June 2009, pp. 1–5, doi:10.1109/ICC.2009.5198971.
- [53] G. Leus, “On the estimation of rapidly time-varying channels,” in *Proc. of EUSIPCO*, Vienna, Austria, Aug. 2004, pp. 2227–2230.
- [54] Y. Li and L. Cimini, “Bounds on the interchannel interference of OFDM in time-varying impairments,” *IEEE Transactions on Communications*, vol. 49, no. 3, pp. 401–404, 2001, doi:10.1109/26.911445.
- [55] S. Lu, R. Kalbasi, and N. Al-Dhahir, “OFDM Interference Mitigation Algorithms for Doubly-Selective Channels,” in *IEEE 64th Vehicular Technology Conference, 2006. VTC-2006 Fall. 2006*, Sept 2006, pp. 1–5, doi:10.1109/VTCF.2006.295.
- [56] M. Matthaiou, D. Laurenson, and C.-X. Wang, “Capacity Study of Vehicle-to-Roadside MIMO Channels with a Line-of-Sight Component,” in *IEEE Wireless Communications and Networking Conference, 2008. WCNC 2008.*, March 2008, pp. 775–779, doi:10.1109/WCNC.2008.142.
- [57] C. Mehlführer, S. Caban, and M. Rupp, “Experimental Evaluation of Adaptive Modulation and Coding in MIMO WiMAX with Limited Feedback,” *EURASIP Journal on Advances in Signal Processing*, vol. 2008, 2008, doi:10.1155/2008/837102.
- [58] M. Meidlinger, M. Simko, Q. Wang, and M. Rupp, “Channel Estimators for LTE-A Downlink Fast

- 
- Fading Channels,” in *IEEE International Conference on Communications 2013. ICC 2013*, Jun. 2013.
- [59] I. Mitola, J., “Software radios-survey, critical evaluation and future directions,” in *Proc. National Telesystems Conference (NTC)*, May 1992, pp. 13/15 –13/23, doi:10.1109/NTC.1992.267870.
- [60] —, “Software radio architecture: a mathematical perspective,” *IEEE Journal on Selected Areas in Communications*, vol. 17, no. 4, pp. 514–538, Apr. 1999, doi:10.1109/49.761033.
- [61] J. Mitola, “The software radio architecture,” *IEEE Communications Magazine*, vol. 33, no. 5, pp. 26–38, May 1995, doi:10.1109/35.393001.
- [62] Z. F. Mohamed M.A. and M. R.H., “Simulation of WiMAX Physical Layer: IEEE 802.16e,” *IJCSNS International Journal of Computer Science and Network Security*, vol. 10, no. 11, November 2010.
- [63] A. Molisch, *Wireless Communications*, ser. Wiley - IEEE. Wiley, 2010.
- [64] M. Morelli, C.-C. Kuo, and M.-O. Pun, “Synchronization Techniques for Orthogonal Frequency Division Multiple Access (OFDMA): A Tutorial Review,” *Proceedings of the IEEE*, vol. 95, no. 7, pp. 1394 –1427, Jul. 2007, doi:10.1109/JPROC.2007.897979.
- [65] A. Mourad and I. Gutierrez, “System level evaluation for WiMAX IEEE 802.16m,” in *IEEE 28th International Performance Computing and Communications Conference (IPCCC), 2009*, December 2009, pp. 418 –424, doi:10.1109/PCCC.2009.5403854.
- [66] “Testbed Design for Wireless Communications System Assessment.”
- [67] H. Nguyen-Le and T. Le-Ngoc, “Joint Synchronization and Channel Estimation for OFDM Transmissions over Doubly Selective Channels,” in *IEEE International Conference on Communications, 2009. ICC '09.*, June 2009, pp. 1–5, doi:10.1109/ICC.2009.5199122.
- [68] T. Ohseki, M. Morita, and T. Inoue, “Burst Construction and Packet Mapping Scheme for OFDMA Downlinks in IEEE 802.16 Systems,” in *IEEE Global Telecommunications Conference, 2007. GLOBECOM '07.*, Nov. 2007, pp. 4307 –4311, doi:10.1109/GLOCOM.2007.819.
- [69] M. Patzold, Y. Li, and F. Laue, “A study of a land mobile satellite channel model with asymmetrical Doppler power spectrum and lognormally distributed line-of-sight component,” *IEEE Transactions on Vehicular Technology*, vol. 47, no. 1, pp. 297 –310, Feb. 1998, doi:10.1109/25.661055.
- [70] P. T. T. Pham and T. Wada, “Effective scheme of channel tracking and estimation for mobile WiMAX DL-PUSC system,” *J. Comp. Sys., Netw., and Comm.*, vol. 2010, pp. 6:1–6:9, Jan. 2010, doi:10.1155/2010/806279.
- [71] H. V. Poor, *An introduction to signal detection and estimation*. Springer Science & Business Media, 2013.
- [72] J. Rodríguez-Piñeiro, P. Suárez-Casal, J. A. García-Naya, L. Castedo, C. Briso-Rodríguez, and J. I. Alonso-Montes, “Experimental validation of ICI-aware OFDM receivers under time-varying conditions,” in *IEEE 8th Sensor Array and Multichannel Signal Processing Workshop (SAM 2014)*, A Coruña, Spain, June 2014.
-

- [73] J. Rodríguez-Piñeiro, M. Lerch, J. A. García-Naya, S. Caban, M. Rupp, and L. Castedo, “Emulating extreme velocities of mobile LTE receivers in the downlink,” *EURASIP Journal on Wireless Communications and Networking. Special issue on “Experimental Evaluation in Wireless Communications”*, vol. 2015, no. 106, pp. 1–14, Apr. 2015, doi:10.1186/s13638-015-0343-0.
- [74] J. Rodríguez-Piñeiro, J. A. García-Naya, A. Carro-Lagoa, and L. Castedo, “A Testbed for Evaluating LTE in High-Speed Trains,” in *Proc. of 16th Euromicro Conference on Digital System Design*, 2013.
- [75] L. Rugini, P. Banelli, and G. Leus, “Low-Complexity Banded Equalizers for OFDM Systems in Doppler Spread Channels,” *EURASIP Journal on Advances in Signal Processing*, vol. 2006, no. 1, p. 067404, 2006, doi:10.1155/ASP/2006/67404.
- [76] T. Schmidl and D. Cox, “Robust frequency and timing synchronization for OFDM,” *IEEE Transactions on Communications*, vol. 45, no. 12, pp. 1613–1621, Dec 1997, doi:10.1109/26.650240.
- [77] P. Schniter, “Low-complexity equalization of OFDM in doubly selective channels,” *IEEE Transactions on Signal Processing*, vol. 52, no. 4, pp. 1002–1011, April 2004, doi:10.1109/TSP.2004.823503.
- [78] H. Schulze and C. Lueders, *Theory and Applications of OFDM and CDMA: Wideband Wireless Communications*, ser. Wiley-Interscience online books. Wiley, 2005. ISBN: 9780470017395. URL: <https://books.google.es/books?id=PzWSwn9gHWEc>
- [79] M. Simko, C. Mehlführer, T. Zemen, and M. Rupp, “Inter-Carrier Interference Estimation in MIMO OFDM Systems with Arbitrary Pilot Structure,” in *IEEE 73rd Vehicular Technology Conference (VTC Spring), 2011*, May. 2011, doi:10.1109/VETECS.2011.5956126.
- [80] C. So-In, R. Jain, and A.-K. Tamimi, “Scheduling in IEEE 802.16e Mobile WiMAX Networks: Key Issues and a Survey,” *IEEE Journal on Selected Areas in Communications*, vol. 27, no. 2, pp. 156–171, Feb. 2009, doi:10.1109/JSAC.2009.090207.
- [81] A. Stamoulis, S. Diggavi, and N. Al-Dhahir, “Intercarrier interference in MIMO OFDM,” *IEEE Transactions on Signal Processing*, vol. 50, no. 10, pp. 2451–2464, Oct. 2002, doi:10.1109/TSP.2002.803347.
- [82] P. Suárez-Casal, A. Carro-Lagoa, J. A. García-Naya, and L. Castedo, “A Multicore SDR Architecture for Reconfigurable WiMAX Downlink,” in *Digital System Design: Architectures, Methods and Tools (DSD), 2010 13th Euromicro Conference on*, Sept. 2010, pp. 801–804, doi:10.1109/DSD.2010.108.
- [83] P. Suárez-Casal, J. A. García-Naya, L. Castedo, and M. Rupp, “KLT-based estimation of rapidly time-varying channels in MIMO-OFDM systems,” in *IEEE 14th Workshop on Signal Processing Advances in Wireless Communications (SPAWC), 2013*, Jun 2013, pp. 654–658, doi:10.1109/SPAWC.2013.6612131.
- [84] —, “Channel Estimation in Spatially Correlated High Mobility MIMO-OFDM Systems,” in *Proceedings of the Tenth International Symposium on Wireless Communication Systems (ISWCS)*

- 
- 2013), Aug 2013, pp. 1–5.
- [85] P. Suárez-Casal, J. Rodríguez-Piñeiro, J. A. García-Naya, and L. Castedo, “Experimental assessment of WiMAX transmissions under highly time-varying channels,” in *the Eleventh International Symposium on Wireless Communication Systems (ISWCS)*, Barcelona, Spain, Aug. 2014.
- [86] —, “Experimental evaluation of the WiMAX downlink physical layer in high-mobility scenarios,” *EURASIP Journal on Wireless Communications and Networking*, vol. 2015, no. 1, p. 109, 2015, doi:10.1186/s13638-015-0339-9.
- [87] Z. Tang, G. Leus, and P. Banelli, “Pilot-Assisted Time-Varying OFDM Channel Estimation Based on Multiple OFDM Symbols,” in *IEEE 7th Workshop on Signal Processing Advances in Wireless Communications. SPAWC '06.*, 2006, doi:10.1109/SPAWC.2006.346364.
- [88] Z. Tang, R. Cannizzaro, G. Leus, and P. Banelli, “Pilot-Assisted Time-Varying Channel Estimation for OFDM Systems,” *IEEE Transactions on Signal Processing*, vol. 55, no. 5, pp. 2226 –2238, May. 2007, doi:10.1109/TSP.2007.893198.
- [89] K. Teo and S. Ohno, “Optimal MMSE finite parameter model for doubly-selective channels,” in *IEEE Global Telecommunications Conference, 2005. GLOBECOM '05.*, vol. 6, Dec. 2005, pp. 3503 –3507, doi:10.1109/GLOCOM.2005.1578424.
- [90] A. Tulino, A. Lozano, and S. Verdu, “Impact of antenna correlation on the capacity of multiantenna channels,” *IEEE Transactions on Information Theory*, vol. 51, no. 7, pp. 2491–2509, July 2005, doi:10.1109/TIT.2005.850094.
- [91] J.-J. Van De Beek, O. Edfors, M. Sandell, S. K. Wilson, and P. O. Borjesson, “On channel estimation in OFDM systems,” in *IEEE 45th Vehicular Technology Conference, 1995.*, vol. 2. IEEE, 1995, pp. 815–819.
- [92] X. Wang and K. R. Liu, “An Adaptive Channel Estimation Algorithm Using Time-Frequency Polynomial Model for OFDM with Fading Multipath Channels,” *EURASIP Journal on Advances in Signal Processing*, vol. 2002, no. 8, pp. 818–830, 2002, doi:10.1155/S1110865702000884.
- [93] Y.-J. Wu, J.-M. Lin, H.-Y. Yu, and H.-P. Ma, “A baseband testbed for uplink mobile MIMO WiMAX communications,” in *IEEE International Symposium on Circuits and Systems, 2009. ISCAS 2009.*, May. 2009, pp. 794 –797, doi:10.1109/ISCAS.2009.5117874.
- [94] T. Yucek, M. Ozdemir, H. Arslan, and F. Retnasothie, “A comparative study of initial downlink channel estimation algorithms for mobile WiMAX,” in *Mobile WiMAX Symposium, 2007. IEEE*, 2007, pp. 32–37, doi:10.1109/WIMAX.2007.348698.
- [95] G. Zaggoulos, M. Tran, and A. Nix, “Mobile wimax system performance - simulated versus experimental results,” in *IEEE 19th International Symposium on Personal, Indoor and Mobile Radio Communications, 2008. PIMRC 2008*, September 2008, pp. 1 –5, doi:10.1109/PIMRC.2008.4699670.
- [96] T. Zemen and C. Mecklenbräuer, “Time-Variant Channel Estimation Using Discrete Prolate Spheroidal Sequences,” *IEEE Transactions on Signal Processing*, vol. 53, no. 9, pp. 3597 – 3607,
-

Sept. 2005, doi:10.1109/TSP.2005.853104.

- [97] X. Zhao, J. Kivinen, P. Vainikainen, and K. Skog, "Characterization of Doppler spectra for mobile communications at 5.3 GHz," *IEEE Transactions on Vehicular Technology*, vol. 52, no. 1, pp. 14 – 23, Jan. 2003, doi:10.1109/TVT.2002.807222.

---

# Appendix A

## Resumen de la tesis

La propagación de ondas electromagnéticas está sujeta a efectos tales como difracción, reflexión o absorción que los sistemas de comunicación inalámbricos deben considerar para transmitir información en estos medios de forma fiable. Uno de los efectos más importantes es el denominado multitrayecto, caracterizado por la llegada al receptor de varias réplicas de la señal emitida por el transmisor. Este fenómeno es más acusado en sistemas de banda ancha, en los que la elevada tasa de muestreo permite distinguir versiones de la misma señal que se han propagado usando distintos caminos entre los dos puntos de comunicación.

Algunas de las técnicas más populares para afrontar este problema son las basadas en modulaciones multiportadora. Todas ellas comparten el principio de transmitir la información utilizando canales estrechos en frecuencia denominados subportadoras. De este modo, cada uno de los símbolos consume más tiempo para completar su transmisión, hecho que se ve compensado por el uso de decenas o miles de estos subcanales en paralelo para no mermar la tasa de transmisión. La principal ventaja de este esquema es que al multiplicar la duración de cada uno de los símbolos transmitidos, la distorsión producida por la llegada de réplicas retrasadas de la señal se minimiza, siempre y cuando el retraso entre estas copias se mantenga varios órdenes de magnitud por debajo de la duración de los símbolos.

Entre las modulaciones multiportadora que se han estudiado en la literatura, OFDM ha sido una de las más estudiadas desde el principio de la década de los noventa. Su principal ventaja respecto a otras modulaciones está en su bajo coste computacional, ya que el proceso de establecer una correspondencia entre cada uno de los símbolos transmitidos con su subportadora se puede implementar de forma eficiente utilizando el algoritmo de la Fast Fourier Transform (FFT). Por otro lado, comparte las mismas ventajas que disfrutaban otros esquemas de múltiples portadoras, siendo la más relevante la sencilla estimación e igualación del canal multitrayecto.

Otro importante efecto en canales inalámbricos es el denominado desplazamiento Doppler, que consiste en que la frecuencia de una señal electromagnética que observa un receptor es dependiente de su velocidad relativa respecto al transmisor de esa señal. Cuando este

desplazamiento se suma al multitrayecto, la llegada de réplicas con distintos desfases en frecuencia toma la forma de rápidas variaciones en las condiciones del canal a lo largo del tiempo. Este fenómeno se conoce como ensanchamiento Doppler, y es una de las principales características de los canales inalámbricos en condiciones de movilidad. OFDM, debido a que utiliza un pulso en forma de función sinc para modular cada una de las subportadoras, es muy sensible a este tipo de fenómenos. Esta variabilidad de la respuesta del canal causa que las subportadoras pierdan su ortogonalidad rápidamente, y que se produzca una interferencia entre ellas.

Numerosos estándares de comunicaciones han utilizado OFDM como pilar fundamental en su capa física, siendo los más destacables Worldwide Interoperability for Microwave Access (WiMAX), Long Term Evolution (LTE) y Digital Video Broadcast–Terrestrial (DVB-T). De todas estas tecnologías se pueden encontrar implementaciones comerciales para el uso de usuarios finales, basadas en chips dedicados a procesar las comunicaciones de cada una de las tecnologías. En cambio, en entornos de desarrollo e investigación, son preferibles soluciones más abiertas y reconfigurables. Se suelen distinguir tres tipos de arquitecturas de cara a la implementación: demostradores, que buscan probar la viabilidad de alguna tecnología; prototipos, pensados para trasladar alguna tecnología al usuario final; y bancos de pruebas, que están a medio camino entre los demostradores y los prototipos. Estos últimos son de especial interés en la comunidad investigadora, dado que permiten probar de forma rápida con transmisiones reales a los algoritmos y técnicas que ya se han evaluado en entornos de simulación.

Los objetivos de este trabajo son dos. En primer lugar, se define una arquitectura para la implementación de capas físicas basadas en OFDM, y se prueba en una plataforma basada en DSPs y FPGAs. Por otro lado, se definen métodos de estimación de canal para OFDM en entornos móviles, y se evalúa su rendimiento tanto en entornos de simulación como en medidas experimentales reales. En las siguientes subsecciones se resumen los aspectos principales de este trabajo.

## **A.1 Arquitectura SDR para la implementación de sistemas basados en OFDM**

El primer resultado de este trabajo es una arquitectura para sistemas OFDM, válida para su implementación en sistemas SDR. Para ello, se ha utilizado como referencia la capa física de WiMAX, aunque este mismo esquema se podría utilizar para otros estándares. El hardware sobre el que se ha probado la arquitectura consta de un DSP y tres FPGAs. Cada una de las tareas que debe completar la capa física se pueden clasificar según sus requerimientos de flexibilidad y de carga computacional. En función de ello, se decide la correspondencia de cada

una de las tareas al DSP, si se necesita una alta reconfiguración, o a las FPGAs cuando los requisitos computacionales son más altos.

WiMAX define tanto la codificación de canal como la subcanalización de los datos en los símbolos OFDM para su transmisión. Respecto a la codificación de canal, el estándar permite el uso de codificadores convolucionales, turbo-códigos y Low Density Parity Check (LDPC). En la arquitectura descrita se ha utilizado el codificador convolucional, que utiliza la técnica conocida como tail-biting. En ella se busca que el estado del registro de codificación coincida al principio y al final de cada bloque. Para ello, este registro se inicializa con los últimos bits del bloque a codificar. Este esquema aumenta el coste computacional de la decodificación, a cambio de no desperdiciar bits en garantizar que el estado del registro de codificación se pone a cero. Para decodificar los bloques finalizados con tail-biting, el receptor debe adivinar cuál fue el estado inicial utilizado en el registro de codificación. La decodificación ML requiere comprobar todos los estados posibles, lo que la convierte en una solución con poca aplicación práctica. En la arquitectura se ha optado por utilizar una aproximación consistente en introducir en el decodificador la última fracción del bloque al principio del mismo, y la primera fracción al final. Tanto el codificador como el decodificador de canal se han colocado en una de las FPGAs.

Respecto a la subcanalización, en el estándar se consideran distintos esquemas, con nombres tales como Partial Usage of Subcarriers (PUSC) o Full Usage of Subcarriers (FUSC). Dado que estas configuraciones requieren mucha flexibilidad respecto a la colocación de las subportadoras piloto y las subportadoras de datos, se ha optado por situar el bloque encargado de este procesado en el DSP. Las ráfagas de datos que produce el codificador de canal deben asignarse definiendo regiones rectangulares en el espacio tiempo-frecuencia de la trama. Los datos de distintos usuarios pueden ir concatenados en la misma ráfaga, siempre y cuando todos ellos compartan el mismo perfil de modulación y tasa de codificación. Para realizar la asignación a la trama se utiliza el algoritmo definido por Ohseki, en el que se busca que en ningún símbolo OFDM se transmita más de una ráfaga de forma simultánea, y ocupando el máximo número de portadoras en frecuencia. La principal ventaja de esta estrategia es que se minimizan los retrasos de decodificación, ya que no hay que esperar a recibir toda la trama para empezar este proceso. Esta tarea es además, en el caso del receptor, la responsable de estimar el canal e igualarlo, utilizando en ambos casos un esquema Least Squares (LS).

Por último, las tareas de multiplexado y demultiplexado de las subportadoras mediante el algoritmo de la FFT, y la detección y sincronización de la trama se efectúan en la FPGA. Esta detección se realiza aprovechando las particularidades del preámbulo utilizado en WiMAX, que consta de tres repeticiones en el dominio del tiempo. También se aprovecha la redundancia proporcionada por el prefijo cíclico, y adicionalmente se hace una correlación cruzada con una versión cuantificada del preámbulo.

Esta arquitectura es general en el sentido de que se puede ajustar para dar soporte a otros tipos de capa física. En el trabajo se muestra un ejemplo de como esta arquitectura se podría

utilizar para una implementación de Advanced WiMAX.

## A.2 Estimación de canal en OFDM en canales doblemente selectivos

El canal inalámbrico en condiciones de baja movilidad, se puede aproximar por un canal invariante en el tiempo. Para su estimación, en OFDM se suelen reservar ciertas subportadoras para transmitir pulsos conocidos a priori en el receptor, en lo que se conoce como entrenamiento asistido con pilotos. Existen alternativas como la estimación ciega, en la que se obvia la transmisión de pilotos y se aprovechan esos recursos para enviar datos, o el entrenamiento superpuesto, en el que las señales que actúan como pilotos se superponen a los datos, permitiendo enviar más información a costa de requerir la separación de pilotos y datos en el receptor.

En condiciones de baja movilidad, la estimación e igualación de canal requieren un muy bajo coste computacional ya que la matriz de canal es diagonal. En cambio, en condiciones de movilidad, la matriz de canal empieza a contener valores distintos de cero fuera de la diagonal principal, con su energía concentrada en torno a una banda central. Estimar la matriz de canal completa requeriría obtener el valor de  $N^2$  coeficientes, siendo  $N$  el número de subportadoras del símbolo OFDM. Si no se diseña de forma específica la estructura de pilotos para este escenario, el sistema de ecuaciones para la estimación sería indeterminado, y si se reserva el suficiente número de recursos, haría inviable la transmisión de datos.

Como alternativa, en la literatura se ha tratado este problema suponiendo que la evolución del canal se puede expresar como la combinación lineal de una serie de vectores, dando lugar a los esquemas de estimación basados en BEMs. Se han definido distintas BEMs, como por ejemplo la Complex Exponential BEM (CE-BEM), Generalized Complex Exponential BEM (GCE-BEM), Polynomial BEM (P-BEM), or Discrete Prolate Spheroidal BEM (DPS-BEM). En el caso de OFDM, se han definido estructuras de pilotos específicas para entornos móviles, en las que cada símbolo piloto se rodea de subportadoras a cero para evitar la interferencia de los datos durante la etapa de estimación de canal. Sin embargo, los estándares de comunicaciones no definen este tipo de pilotos, por lo que otro tipo de algoritmos son preferibles para la implementación en sistemas prácticos.

Un esquema alternativo consiste en utilizar como referencia las estimaciones de la respuesta en frecuencia obtenidas durante un grupo de símbolos OFDM. Tomando las variaciones en tiempo entre estas estimaciones se puede aproximar la ICI que se está produciendo entre las portadoras. En trabajos anteriores este proceso se realizaba mediante una regresión por LS, definiendo BEMs para la duración de un grupo de símbolos OFDM, y muestreándolas en la mitad de cada uno de los símbolos.

En este trabajo se sigue esta aproximación, obteniendo la BEM óptima considerando que los coeficientes de canal en un sistema OFDM representan la media de la respuesta en frecuencia durante la duración de cada uno de esos símbolos. Estas BEMs se definen para dos situaciones, una en la que solo se dispone de las estadísticas de segundo orden en el dominio del tiempo del canal, y otra en la que también se conoce la correlación espacial en entornos MIMO.

Las simulaciones se hicieron utilizando tramas que seguían la estructura de pilotos de WiMAX Advanced, y en canales MIMO considerando situaciones con y sin correlación espacial. En los resultados obtenidos se puede comprobar como los errores de estimación obtenidos con estas BEMs son menores a los obtenidos con esta técnica en anteriores trabajos, especialmente al compararse en entornos con espectros Doppler como el modelo de Jakes asimétrico.

### **A.3 Evaluación experimental de OFDM bajo canales doblemente selectivos**

En este trabajo se siguen dos aproximaciones para la evaluación de señales OFDM bajo condiciones de selectividad en tiempo y frecuencia. La primera, utilizada para evaluar la implementación de la arquitectura SDR, está basada en el uso de un emulador de canal. La segunda, en extender la duración de los símbolos OFDM para obtener efectos similares a los observados en canales de alta movilidad.

El emulador de canal está implementado sobre una FPGA, y permite la reproducción de canales multitrayecto, además de canales Additive White Gaussian Noise (AWGN). En lo que respecta al canal multitrayecto se utiliza un modelo basado en coeficientes, en el que la respuesta al impulso del canal se genera siguiendo una distribución Rice. A cada uno de los coeficientes se le puede asignar un retardo y una potencia media, y su espectro Doppler se genera siguiendo el modelo de Jakes. Para producir coeficientes de canal siguiendo este modelo, se filtran muestras de ruido blanco con un filtro cuya respuesta en frecuencia coincide con la definida en el modelo de Jakes.

Este emulador se utiliza para evaluar la arquitectura SDR, y en los resultados se pueden observar los efectos de la variabilidad del canal en la señal OFDM. Para escenarios de movilidad, se obtienen suelos en la tasa de error de bit, ocasionados por la interferencia entre portadoras, ya que la implementación no considera la interferencia producida por la ICI.

Realizar medidas en entornos de movilidad reales puede resultar muy costoso, o incluso imposible, si se desea estudiar el comportamiento de las señales a velocidades muy altas. En este trabajo, como alternativa, se emplea una técnica basada en alargar la duración de los símbolos OFDM para emular estas condiciones de alta velocidad.

Este esquema se puede resumir en los siguientes pasos:

1. La señal generada por el transmisor se alarga en tiempo según un factor de interpolación  $I$ .
2. La señal se emite o se recibe desde algún equipamiento que se desplaza a velocidad  $v$ .
3. El receptor captura la señal, y deshace el paso de interpolación. Desde el punto de vista del receptor, será equivalente a una señal transmitida sin interpolación a una velocidad  $v' = vI$ .

Este esquema permite recrear de manera bastante fidedigna los efectos que tendría un canal selectivo en tiempo a bajas velocidades. Por ejemplo, considerando que las medidas se realizan con  $v = 20$  km/h con un factor de interpolación  $I = 12$ , la velocidad emulada será de  $v' = 360$  km/h. Sin embargo tiene desventajas, ya que al alargar la señal en el dominio del tiempo, esta se vuelve muy estrecha en frecuencia, ocupando una fracción del espectro original. De esta manera, parte de la selectividad en frecuencia, que viene causada por el multitrayecto, tiende a desaparecer paulatinamente a medida que aumenta el factor  $I$ .

En esta tesis se han considerado medidas en dos escenarios, situando el transmisor en la Facultad de Informática de A Coruña, y en el edificio CITIC del Campus de Elviña. En ambos casos el receptor se situó en el interior de un coche, que seguía unas rutas predefinidas sobre las que se hacían varias pasadas. El equipamiento con el que se realizaron las transmisiones está basado en un banco de pruebas implementado con tres placas USRP B210, que permiten realizar transmisiones MIMO con dos antenas con hasta 56 MHz de ancho de banda. Una de las placas se utiliza para el transmisor, conectada a dos amplificadores de alta potencia Mini-Circuits TVA-11-422, dos antenas polarizadas verticalmente Interline SECTOR IS-G14-F2425-A120-V, o dos antenas con polarización cruzada Ubiquity AM-2G15-120. Una de las antenas polarizadas fue la usada para las medidas SISO, mientras que las de polarización cruzada se utilizaron para las medidas MIMO.

Las dos placas restantes se utilizaron como receptor en el interior del coche, cada una conectada a una antena distinta: una en el interior y otra en el exterior del coche. De este modo se pueden capturar las mismas tramas a la vez en ambos entornos, y evaluar la atenuación producida en el interior.

Respecto a las señales generadas, se utilizó un software implementado en Matlab que incluye los aspectos fundamentales de una capa física WiMAX, desde la codificación de canal con códigos convolucionales, hasta la asignación de ráfagas y subcanalización de la trama. En todas las campañas de medidas se utilizó una estructura de trama consistente en seis ráfagas con las siguientes combinaciones de modulación y codificación de canal: 4-QAM 1/2, 4-QAM 3/4, 16-QAM 1/2, 16-QAM 3/4, 64-QAM 1/2 y 64-QAM 3/4. Según el escenario, las tramas se emitieron con distintos factores de interpolación  $I$  siguiendo estrategias diferentes. En el primer escenario, cada uno de los recorridos del coche se hizo capturando tramas utilizando

el mismo factor  $I$ . La principal ventaja de este sistema es que permite capturar un número de tramas mucho mayor en los casos de factores  $I$  pequeños. En el segundo caso, se definió una “supertrama” consistente en tres tramas con factores  $I = 12$ ,  $I = 20$  e  $I = 32$ , que se envían alternativamente. Este esquema se utilizó para evitar en lo posible grandes disparidades en el estado del canal entre las pasadas con el coche.

Como resultado de esta campaña se pudieron probar los algoritmos de estimación de ICI en entornos reales, validando los resultados que ya se habían obtenido en simulación en este y otros trabajos anteriores. Además, se hicieron comparaciones utilizando varios estimadores de la respuesta en frecuencia del canal, y por último, también se obtuvieron algunas aproximaciones de la tasa de transmisión siguiendo distintos criterios. En la práctica, se ha observado en general cierta ganancia utilizando los métodos de cancelación de ICI, aunque la selección del perfil adecuado para hacer las transmisiones resulta importante de cara a esta medida de mérito.

## **A.4 Conclusiones**

En esta tesis se han estudiado las propiedades de la señal OFDM bajo canales selectivos en tiempo y frecuencia, y se han probado bajo distintas condiciones. Por un lado, se ha utilizado una arquitectura implementada sobre FGPA y DSPs funcionando en tiempo real, y basada en el estándar de WiMAX. En este caso la metodología de la evaluación se basó en utilizar un emulador de canal, con el que se pudieron experimentar los efectos de la selectividad en tiempo con un receptor que no considera la ICI.

Por otro lado, se han estudiado métodos de estimación de canal que utilizan como entrada la respuesta en frecuencia de una serie de símbolos OFDM consecutivos y que a partir de sus variaciones en tiempo obtienen la ICI. Para ello, se han diseñado BEMs que son óptimas para este tipo de estimadores, probando en entorno de simulación su superioridad respecto a otras BEMs desarrolladas con anterioridad, sobre todo en entornos en los que el espectro Doppler se aleja del espectro plano, como por ejemplo con el modelo de Jakes asimétrico.

Por último, se han verificado la validez de estos resultados en simulación con medidas reales, y utilizando distintos estimadores de respuesta en frecuencia. Además, se han obtenido estimaciones en tasa de transmisión, en las que también se verificó la ganancia de utilizar cancelación de ICI.